Abstract

First-Principles Investigation on Boron Nanostructures

Hui Tang
2011

First-principles calculations based on density functional theory are employed to study and predict the properties of boron and Mg boride nanostructures. For boron nanostructures, two-dimensional boron sheets are found to be metallic and made of mixtures of triangles and hexagons which benefit from the balance of two-center bonding and three-center bonding. This unusual bonding in boron sheets results in a self-doping picture where adding atoms to the hexagon centers does not change the number of bonding states but merely increases the electron count. Boron sheets can be either flat or buckled depending on the ratio between hexagons and triangles. Formed by stacking two identical boron sheets, double-layered boron sheets can form interlayer bonds, and the most stable one is semiconducting. Built from single-layered boron sheets, single-walled boron nanotubes have smaller curvature energies than carbon nanotubes and undergo a metal-to-semiconductor transition once the diameter is smaller than $\sim$20 Å. Optimal double-walled boron nanotubes with inter-walled bonds formed are metallic and always more stable than single-walled ones. For Mg boride nanostructures, certain Mg boride sheets prefer to curve themselves into nanotubes, which is explained via Mg-Mg interactions governed by the charge state of Mg. In addition, optimal Mg boride sheet structures are explored with a genetic algorithm. Phase diagrams for Mg boride sheet structures are constructed and stable phases under boron-rich environments are identified. Curvature effects on the phase diagram of Mg boride nanotubes are also discussed. As a natural extension to boron sheets, layered boron crystals based on boron sheets are then presented and are shown to be stable under high pressure. Finally, this thesis ends with an investigation of hydrogen-storage properties of pristine and metal doped boron nanostructures.

First-Principles Investigation on Boron Nanostructures

A Dissertation
Presented to the Faculty of the Graduate School
of
Yale University
in Candidacy for the Degree of
Doctor of Philosophy

Hui Tang

Dissertation Director: Sohrab Ismail-Beigi

May 2011

Acknowledgements

First and foremost, I owe my deepest gratitude to my advisor Prof. Ismail-Beigi. For the past six years, he has not only been an extremely supportive and considerate advisor, but also been a super nice and funny friend to me. There's no way I can make it without the every week discussions we had when he patiently listened to my thoughts, and never failed to bring up brilliant ideas. As a matter of fact, I enjoyed every minute working and talking with him, starting from the first phone interview he made to me when I was still a college student in China more than six years ago.

Next, I thank Prof. Stone and Prof. Henrich for carefully reading my thesis and serving on my committee for the past six years. Thank you for consistently advising and supporting me and my research!

I would also like to take this opportunity to thank all my friends at Yale. You guys made my life at Yale so colorful and wonderful. Studying abroad could be hard and painful, but I have had the best time of my life with you guys around. I do believe that whenever and wherever I end up going for the next phase of my life, I will always cherish our friendship and keep it in the bottom of my heart.

My thanks also go to my officemates and colleagues, Kevin Garrity, Hanghui Chen, Xiao Pan, Alexie Kolpak and Jie Jiang. For years, I have spent more time together with you than my family. I have learned so much from all of you, on research and personalities. I wish you all the best with everything in life.

Finally, I would like to thank my family, although I know I can never thank them enough. I want to thank my parents for their most selfish and deep love and support to me, which give me the power to fight for the best in life and the mind to appreciate all the good happening to me. Also, I thank my wife Xiaopu Sun for always being my best friend and always being there for me whenever I needed.

Contents

List of Figures

List of Tables

Chapter 1

Introduction

In the past few decades, first-principles calculations based on density functional theory (DFT) have been applied to model various systems, providing accurate results comparable to the most precise experiments [1]. With neither predefined assumptions nor fitted parameters, DFT is capable of not only describing existing materials realistically, but also reliably predicting unknown properties of novel electronic systems. Armed with modern computational facilities, first-principles DFT calculations can be applied to systems with up to thousands of atoms. First-principles calculations allow us to obtain valuable information when experiments are not possible or too demanding to perform. In addition, due to the rapidity and flexibility in modeling systems with different setups, first-principle calculations can be great substitutes for experiments in sampling and screening candidates to obtain the right materials. Finally, first-principles calculations provide detailed information on the studied system which let us further explore the mechanism for interesting properties and propel our understanding of novel physics.

Boron and boron related nanostructures are ideal systems to investigate with first-principles calculations. As the neighbor of carbon in the periodic table, the "fifth element" boron is on the crossing point of metals and insulators, due to which the chemical bonding of boron tends to be extremely complicated. The observed crystalline phases of boron are all based on B_{12} icosahedra which are interconnected and/or connected to other segments [2, 3, 4, 5]. As an example, Figure 1.1 shows the structure of α rhombohedral boron. The bonding in boron crystals is mixture of two-center bonding and three-center bonding

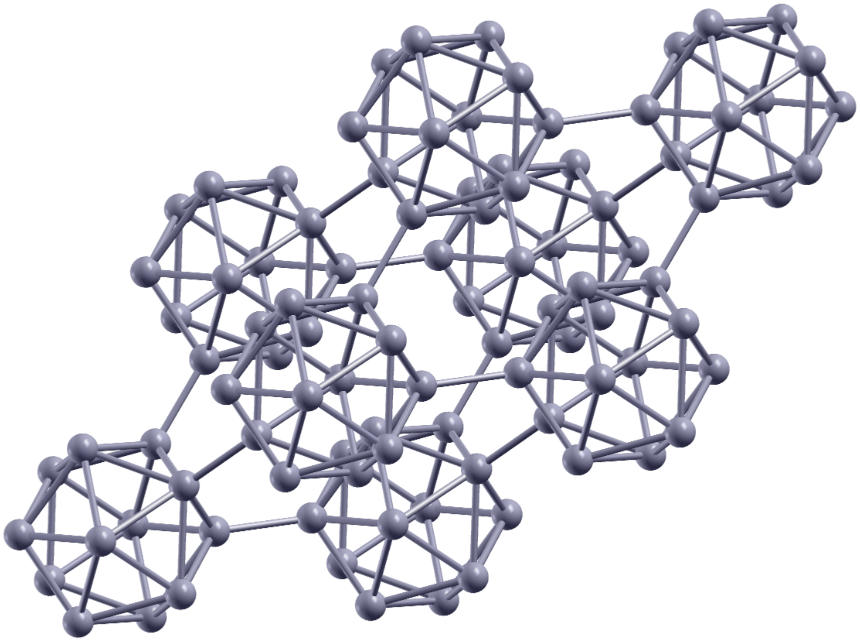

Figure 1.1: Illustration of α rhombohedral boron which is made of interconnected B_{12} icosahedra. Gray balls are boron atoms.

[2, 5] which is also common in boron nanostructures [6]. The strength of mixed boron bonding changes with local environment and is difficult to capture with fitted empirical potentials or tight-binding methods. Furthermore, nanostructures of boron have very different geometries from boron crystals, and knowledge of the crystals does not help with our understanding of the nanostructures. Hence, modeling boron nanostructures from first-principles calculations is the only reliable choice and has been shown to be accurate and efficient in describing the properties of boron and boron related nanostructures [6, 7, 8].

Previous work

Boron is a fascinating element with versatile chemistry even compared to carbon and exhibits various stable boron-based architectures [11]. In particular, boron nanostructures are of great interest to scientists because of their unique structures and possible novel properties. For instance, large-diameter boron nanotubes are predicted to be good one-dimensional conductors independent of chiral indices [12, 13]; pure boron nanotubes and

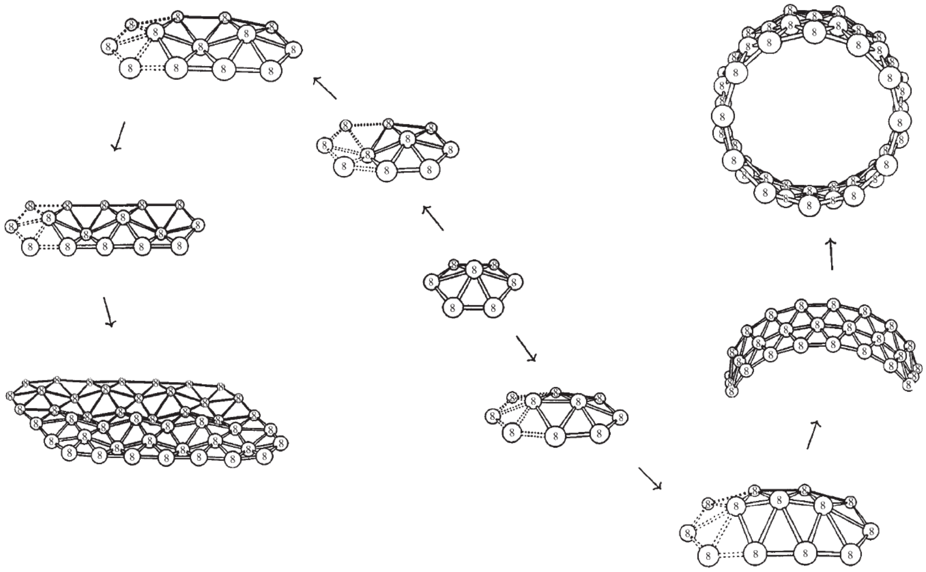

Figure 1.2: Illustration of the Aufbau principle for boron clusters [9, 10]. All large boron clusters, boron sheets and boron nanotubes were proposed to be built from one B_7 unit.

Mg doped boron nanotubes may be superconducting at quite high temperature [14]; boron-based clusters can be used as building blocks to fabricate novel macromolecules [11].

The first research on boron clusters can be traced back to the 1990s; it was inspired by the astonishing properties of carbon clusters, especially fullerenes [15]. Early research work was mainly theoretical and was focused on small boron clusters with less than 20 atoms [16, 17, 18, 19, 9]. These small boron clusters were found to be buckled quasi-planar structures with triangular motifs as the basic constructing unit. Based on this discovery, an Aufbau principle was proposed suggesting that triangular motifs are the building block for surfaces of stable boron nanostructures, including large two-dimensional sheets and tubular structures [9]. These theoretical work was then further backed up by many experiments on small boron clusters [20, 21, 22, 23, 24], and the structures of small boron clusters were solved unambiguously. These quasi-planar boron clusters were further shown to be aromatic in the same manner as carbon molecules [21, 25]. When it came to larger boron clusters, the story became rather complex. Theoretical calculations proposed competitive structures with different geometries including quasi-planar, double-layered quasi-planar, tubular and spherical, all of which are built based on triangular motifs following the Aufbau principle [26, 27, 28, 29]. Only one experiment reported fabrication of boron clusters with

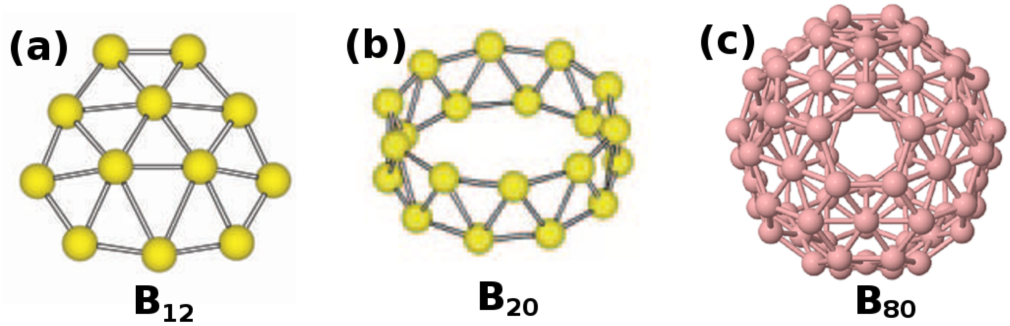

Figure 1.3: Illustrations of boron clusters with various geometries: (a) quasi-planar [21], (b) tubular [24] and (c) fullerene [30].

more than 20 atoms which identified a tubular structure for B_{20} clusters [24]. B_{20} was then seen as the transition point from planar structures to tubular ones.

Inspired by the discovery of tubular boron clusters and the Aufbau principle, several models were proposed predicting the existence of long one-dimensional (1D) boron nanotubes similar to the known carbon nanotubes [31, 32, 33, 34, 10]. In 2004, the first boron nanotubes were reported to be fabricated in experiments with mesoporous catalysts by Pfefferle's group at Yale [35] and spurred further enthusiasm for these materials. After that, first-principles calculations were performed extensively to investigate boron nanotubes [36, 37, 38, 39, 40]. All these works were based on a triangular sheet which has a buckled geometry with lines of boron atoms going alternatively up and down and strong two-center-like bonds forming along the boron lines. All single-walled boron nanotubes made of the buckled triangular sheet are predicted to be metallic with large densities-of-states around the Fermi level, raising the possibility of superconducting boron nanotubes. In addition, due to surface buckling the stability of boron nanotubes is strongly dependent on chirality as well as diameter. In particular, boron nanotubes with buckling lines lying along the nanotubes have almost zero curvature energies [38]. Double-walled boron nanotubes based on triangular sheets are also investigated [41]. Strong bonds exist between inner and outer nanotubes and stabilize double-walled boron nanotubes.

Since 2007, research on boron nanostructures was propelled by many theoretical discoveries. The first one predicted the existence of boron fullerenes which are spherical and hollow inside with surfaces composed of mixtures of pentagons, hexagons and triangles showing exceptional stability [30]. These boron fullerenes have structures closely related to those of carbon fullerenes. For instance, the B_{80} fullerene can be constructed from the C_{60} structure by filling all 20 hexagon faces with extra atoms. Following this work, many other boron fullerenes were predicted with construction rules proposed [42, 43, 44]. Furthermore, by unzipping the B_{80} fullerene, a boron sheet that is more stable than the buckled triangular sheet was discovered [12]. Separately, we predicted a class of stable 2D boron sheets with the most stable α sheet coinciding with the previous prediction [6, 12]. These boron sheets are made of mixtures of hexagonal and triangular motifs and are always metallic. The connection between the 2D sheets and fullerenes is clear – the most stable α sheet [6] is the precursor for boron fullerenes similar to graphene and carbon fullerenes. With these new boron sheets, researchers studied single-walled boron nanotubes built from the α sheet [12, 13]. The stability of these boron nanotubes depends not on chirality but solely on diameter, similar to carbon nanotubes. Furthermore, although α sheet is metallic, boron nanotubes made of α sheet become semiconducting once the diameter is smaller than 20 Å. This metal-to-semiconductor transition is caused by curvature induced surface buckling.

Besides boron nanostructures, some early work predicted that stable metal boride nanotubes can exist in the form of isolated nanotubes and are further stabilized by forming nanotube bundles [45, 46, 47]. These metal boride (MgB_2, AlB_2 and BeB_2) nanotubes were shown to be very good one-dimensional conducting systems and might possibly be superconducting. In fact, the possibility of superconductivity in nanostructures has always been a fascinating subject in physics and materials science. For example, small-radius carbon nanotubes have been shown to be superconducting at low temperatures [48, 49]. Beyond carbon-based materials, MgB_2 as a bulk crystal has attracted interest due to the discovery of superconductivity near 40 K [50]. As nanomaterials, researchers have proposed that MgB_2 nanotubes, which could be fabricated by doping boron nanotubes with Mg [51], may have higher superconducting temperatures than MgB_2 bulk due to electron confinement [45, 52]. As a result, MgB_2 nanotubes were extensively studied in theory [45, 51, 52, 53, 54]. In all theoretical work, Mg boride nanostructures are based on a 2D precursor sheet extracted directly from bulk MgB_2. This is problematic because the sheet is not necessarily the most stable sheet structure for MgB_2 and MgB_2 may not be the right stoichiometry for nanostructures. In 2009, an experiment on Mg boride nanostructures showed a promising result on superconductivity [14]. By doping boron nanotubes with small amount of Mg, researchers fabricated Mg boride nanostructures showing a diamagnetic transition at as high as 80 K, which implies a superconducting temperature much higher than the MgB_2 bulk. However, the geometry and stoichiometry of the fabricated Mg boride nanostructures are still unknown from experiments.

Overview of this thesis

The work in my thesis is mainly dedicated to applying first-principles calculations based on DFT to study boron and Mg boride nanostructures, including two-dimensional sheets and one-dimensional nanotubes. Using first-principles calculations, we predict optimal structures, explain chemical bonding and explore electronic properties of these boron nanostructures with help from experiments. In addition, I present layered boron crystals based on sheet structures which are stable under high pressure and discuss the possibility to apply boron nanostructures to hydrogen storage.

In Chapter 2, I briefly describe theory and methods used in my research. First, I present density functional theory and pseudopotentials which are the two bases for first-principles calculations. Second, the scheme to generate maximally localized Wannier functions (MLWFs) is shown and possible applications of MLWFs are discussed. In addition, I describe the genetic algorithm which is a minimization technique to find global minima via stochastic processes. (Further details of the genetic algorithm and its generalization to 2D sheets and 1D nanotubes are presented in Appendix A.) Finally, the nudged elastic band (NEB) method is presented, which efficiently finds the minimal energy path for a reaction and determines the energy barrier for the reaction.

Chapter 3 presents my research work on structures and electronic properties of boron sheets and nanotubes. In the first part, I discuss my results on single-layered and double-layered boron sheets. Because boron has three valence electrons but four atomic orbitals, 2D atomically-thin boron sheets are made of mixtures of triangles and hexagons, with triangular regions as electron donors and hexagonal regions as acceptors [6]. The stability of boron sheets benefits from the balance of electron donors and acceptors. Due to the existence of triangular regions, the chemical bonding in boron sheets is mixed two-center and three-center type. With the help of MLWFs we are able to show the bonding scheme explicitly and identify a novel self-doping behavior in boron sheets [7]. Self-doping means that adding a boron atom to the center of a hexagon does not change the number of bonding states, but merely increases the electron number by three, which is similar to a classic doping phenomenon. Self-doping provides a convenient way to understand the stability of boron sheets and helps develop a design rule to build stable boron nanostructures from carbon nanostructures. Self-doping also constitutes an efficient scheme to search for the optimal metal boride sheets at given stoichiometries. Furthermore, boron sheets prefer to have flat or buckled ground state geometries determined by the hexagon-to-triangle ratio. Boron sheets with large triangular regions prefer to become buckled [8]. This asymmetric buckling can be well explained via an unconventional electron gas picture. Finally, double-layered boron sheets are constructed by stacking two identical single-layered boron sheets. Strong interlayer bonds are formed only for double-layered boron sheets built on single-layered boron sheets with buckled ground states. The most stable double-layered boron sheet is more stable than the single-layered one and is semiconducting with a DFT band gap of about 0.8 eV.

In the second part of Chapter 3, I present my results on single-walled and double-walled nanotubes. Single-walled boron nanotubes made of the α sheet have smaller curvature energies compared to carbon nanotubes, and the curvature energy of boron nanotubes depends only on diameter, similar to carbon. Although the α sheet is metallic, small-diameter single-walled boron nanotubes can become semiconducting due to surface buckling induced by curvature. The energy gain from surface buckling is very small, but the semiconducting behavior of small boron nanotubes is quite stable according to the calculations of soliton perturbations [8]. Finally, double-walled boron nanotubes built with three different schemes are presented. The most stable double-walled boron nanotubes have mismatched inner and outer nanotubes, are metallic and are always more stable than single-walled boron nanotubes [8].

Chapter 4 investigates Mg boride nanostructures including sheet structures and nanotubes. First, negative curvature energy in Mg doped boron sheets is presented. When doped on different boron sheets, the Mg-Mg interactions are governed by the charge state on Mg as determined by the alignment of Fermi levels between Mg and boron sheets. Due to the interaction between Mg atoms, many Mg doped boron sheets prefer to curve into nanotubes and have negative curvature energies, which is unique and not seen in other systems. In addition, the structures of Mg boride sheets with various stoichiometries are studied with genetic algorithms. The phase diagrams are then constructed and the most stable phases under boron-rich environments are identified. Finally, curvature effects are considered and some preliminary results on how curvature changes the phase diagrams are described.

In Chapter 5, a new class of layered boron crystals are presented and compared to other stable boron phases. Layered boron crystals are built up by stacking boron sheets with additional bonds formed between layers. These new boron structures are less stable than α rhombohedral boron at ambient condition by 0.1-0.2 eV/atom but can become competitive in stability under high pressure and high temperature. Finally, layered boron crystals are metallic with large densities-of-states around the Fermi levels, different from other stable boron phases.

In Chapter 6, the possibility of using boron based nanostructures as hydrogen storage materials is explored. Physisorption and chemisorption of hydrogen on pristine and metal doped boron nanostructures are studied, among which physisorption of hydrogen on Ca doped boron nanostructures gives reasonable absorption energies. However, the energy barriers for hydrogen to be chemisorbed on Ca doped boron sheets are small and even close to zero, and hence chemisorption can become a competing mechanism with physisorption which jeopardizes the performance of Ca doped boron nanostructures as hydrogen storage materials. Finally, a preliminary phase diagram for 2D Ca boride sheets is shown which suggests that the Ca doped α sheet is unstable and thus not a promising hydrogen storage material.

Chapter 2

Methods

2.1 Density functional theory

In an interacting system of electrons and nuclei, all properties are in principle determined by the many-body Hamiltonian of the system, which consists of kinetic energies of electrons and nuclei, Coulomb potentials between electrons and electrons, nuclei and nuclei, and electrons and nuclei. Due to the much smaller mass of an electron than a nucleus, the motion of electrons can be separated from that of the nuclei with the Born-Oppenheimer approximation (or adiabatic approximation), which assumes that electrons respond instantaneously to the motion of nuclei and neglects possible coupling between electrons and motion of nuclei (or phonons). With this adiabatic approximation, the original problem is simplified into many interacting electrons moving in an external potential field generated by all nuclei. However, this many-electron problem is still difficult to deal with, and one of the most efficient and successful approximate solutions to it is based on density functional theory (DFT) [55, 56, 57]. DFT works with the electron density instead of the many-body wavefunctions.

DFT is based on the fact that ground-state properties of an electronic system can be uniquely determined by its electron density [55]. An energy functional of the electron density $\rho(\mathbf{r})$ can be defined as

$$E[\rho(\mathbf{r})] = \int d\mathbf{r} v(\mathbf{r})\rho(\mathbf{r}) + F[\rho(\mathbf{r})], \tag{2.1}$$

where $v(\mathbf{r})$ is the external field acting on the electrons, $F[\rho(\mathbf{r})]$ is the expectation value of the kinetic and electron-electron energies and is a universal functional of $\rho(\mathbf{r})$. This energy functional $E[\rho(\mathbf{r})]$ is minimized by the ground state electron density $n(\mathbf{r})$, and $E[n(\mathbf{r})]$ is the ground state energy. Hence, the ground state properties can be in principle solved via the variational principle with the constraint of a fixed number of electrons.

This system of interacting electrons can be further mapped into non-interacting electrons moving in an effective potential [56]. If $\psi_i(\mathbf{r})$'s are the single-particle wavefunctions for the non-interacting electrons and satisfy the following constraint

$$\rho(\mathbf{r}) = \sum_{i=1}^{N} |\psi_i(\mathbf{r})|^2, \tag{2.2}$$

where the summation is over the N occupied states, the kinetic energy of non-interacting electrons with density $\rho(\mathbf{r})$ is given by

$$T_s = -\frac{\hbar^2}{2m} \sum_i \langle \psi_i | \nabla^2 | \psi_i \rangle, \tag{2.3}$$

where m is the mass of an electron. We decompose $F[\rho(\mathbf{r})]$ into three terms

$$F[\rho(\mathbf{r})] = T_s + E_h + E_{xc} = T_s + \frac{1}{2} \int d\mathbf{r} d\mathbf{r}' \frac{\rho(\mathbf{r})\rho(\mathbf{r}')}{|\mathbf{r} - \mathbf{r}'|} + E_{xc}, \tag{2.4}$$

where E_h is the Hartree energy and E_{xc} is the exchange-correlation energy defined by whatever is leftover in $F[\rho(\mathbf{r})]$. By minimizing the energy functional $E[\rho(\mathbf{r})]$ over $\psi_i(\mathbf{r})$ with the constraint $\rho(\mathbf{r}) = \sum_i |\psi_i(\mathbf{r})|^2$, we can obtain the following Kohn-Sham equations

$$\left[-\frac{\hbar^2}{2m} \nabla^2 + v_{eff}(\mathbf{r}) \right] \psi_i(\mathbf{r}) = \epsilon_i \psi_i(\mathbf{r}), \tag{2.5}$$

where the effective potential is

$$v_{eff}(\mathbf{r}) = v(\mathbf{r}) + \int d\mathbf{r} \frac{\rho(\mathbf{r}')}{|\mathbf{r} - \mathbf{r}'|} + \frac{\delta E_{xc}}{\delta \rho(\mathbf{r})}. \tag{2.6}$$

The Kohn-Sham equations should be solved self-consistently due to the dependence of $v_{eff}(\mathbf{r})$ on $\psi_i(\mathbf{r})$.

Within the Kohn-Sham scheme, all the complexity falls into E_{xc} which is an unknown functional of $\rho(\mathbf{r})$ for an inhomogeneous electron gas. To make the entire scheme work, we need some approximate E_{xc} in a computable format. The first commonly used approximation is the local density approximation (LDA) [56, 58]

$$E_{xc} \approx E_{xc}^{LDA} = \int d\mathbf{r}\rho(\mathbf{r})\varepsilon_{xc}(\rho(\mathbf{r})), \tag{2.7}$$

where $\varepsilon_{xc}(\rho)$ is the exchange-correlation energy per electron in a uniform electron gas with density ρ. $\varepsilon_{xc}(\rho)$ has been computed with quantum Monte Carlo simulations and parametrized in several formats [58]. In principle, we expect that the LDA works best for systems with slowly varying electron density and fails for very inhomogeneous cases like atoms and surfaces. However, the LDA has been shown to be very successful in describing various electronic systems including even very inhomogeneous ones. One reason for the success is that LDA captures the right sum rules for the exchange-correlation hole [1].

After the LDA, further improvement to the approximation of exchange-correlation energy leads to various generalized gradient approximations (GGAs) [59, 60]. Although different in their detailed formats, the GGAs essentially include the magnitude of the gradient of electron density

$$E_{xc} \approx E_{xc}^{GGA} = \int d\mathbf{r}\rho(\mathbf{r})\varepsilon_{xc}(\rho(\mathbf{r}), |\nabla\rho(\mathbf{r})|), \tag{2.8}$$

and thus are better at dealing with inhomogeneous systems. GGAs have shown systematic improvement over the LDA on binding energies and have extended the application of DFT to quantum chemistry, which requires higher computational accuracy [1].

2.2 Pseudopotentials

The pseudopotential method provides an efficient modeling of the electron-ion interaction to assist first-principle calculations based on DFT [61, 62, 63]. Two basic approximations are included in constructing pseudopotentials. The first one is the separation of frozen core electrons from chemically active valence electrons. In an atom, we separate electrons into core and valence electrons. For instance, carbon has two core electrons in the 1s state and four valence electrons filling the $2s$ and $2p$ states. Core electrons are tightly bound to the nuclei with low eigen-energies and stay in the core region forming closed shells. Core electrons are usually inert in condensed matter systems and are largely irrelevant in determining most properties of materials. In contrast, valence electrons which are loosely bound to the nuclei participate in forming chemical bonds with other atoms and determine the main properties of materials. Given the inertness of core electrons, we can combine core electrons and the nuclei to form an positive frozen core and consider only valence electrons interacting through an effective potential with the frozen core.

With this frozen-core approximation, we only worry about valence electrons. However, the effective potential between valence electrons and the frozen core is still Coulomb-like and is very strong close to the core region. Because of the strong potential, wavefunctions of valence electrons usually have rapid oscillations near the core region, which creates difficulties for calculations. We can circumvent the problem by noticing the fact that important properties of materials (e.g., chemical bonds) are determined by wavefunctions in the interstitial region between atoms instead of wavefunctions near the core region. As long as wavefunctions in the interstitial region are described accurately, properties of materials would be modeled correctly. Hence, we can make another approximation by replacing the real valence electron wavefunctions with pseudo-wavefunctions which are smooth and nodeless inside the core region but agree with the true wavefunctions outside the core. The resulting effective potentials are called pseudopotentials. Pseudopotentials are not unique because we can vary the size of the core region and also optimize the pseudo-wavefunctions inside the core region to create pseudopotentials that fit specific needs.

Pseudopotentials have been a very convenient tool and have greatly facilitated DFT calculations. On the one hand, pseudopotentials remove core electrons and allow us to work with valence electrons only, which improves the speed of calculations compared to all-electron calculations and thus is especially crucial for heavy elements with large numbers of core electrons. On the other hand, pseudopotentials artificially create smooth nodeless wavefunctions inside the core region to replace the original wavefunctions with nodes and fast oscillations. If the oscillations were not removed by pseudopotentials, a huge number of Fourier components would be needed to to expand the wavefunctions, which results in extremely large planewave bases. Hence, pseudopotentials have allowed us to use a planewave basis in our calculations which otherwise would be formidable to use in any serious calculations due to the need to resolve irrelevant but rapid oscillations of wavefunctions in the core region.

Furthermore, pseudopotentials naturally explain the chemical similarity between elements in the same group. We take C and Si as examples. C has 4 valence electrons in $2s$ and $2p$, and Si also has 4 valence electrons filling $3s$ and $3p$. After pseudizing the two elements to obtain pseudopotentials, C and Si become extremely similar: both have pseudopotentials converging quickly to $-4/r$ for large r and 4 electrons filling $1s$ and $2p$ states. C and Si only differ in pseudopotentials near the core region. Hence, for elements in the same group, their pseudo-atoms have the same number of electrons and pseudopotentials with the same asymptotic behavior, which result in similar chemical properties.

2.3 Maximally localized Wannier functions

In a periodic system, electronic states are usually described with Bloch states $\psi_{n\mathbf{k}}(\mathbf{r})$ labeled by band index n and crystal momentum $\mathbf{k}$ which are eigenstates of the crystalline Hamiltonian and propagate throughout the system. Alternatively the electronic states can be represented in terms of localized Wannier functions $W_n(\mathbf{r}-\mathbf{R})$ with band-like index n and lattice vector $\mathbf{R}$ which are presumably localized functions at $\mathbf{R}$. Wannier functions are obtained via a Fourier transformation of Bloch states from $\mathbf{k}$ representation to $\mathbf{R}$ representation spanning the same sub-space as their corresponding Bloch states.

Although used as a powerful theoretical tool, the application of Wannier functions in numerical problems has been hindered by the arbitrariness in their definition [64]. For an isolated band, the freedom in choosing the phases of the Bloch states can result in Wannier functions that are different in shape, not necessarily localized and in some cases are as extended as the Bloch states. In addition, for a group of composite bands there is the extra freedom to mix Bloch states of different bands through a unitary transformation. To resolve this problem, the standard method is to remove the arbitrariness of Wannier functions via minimizing their total spreads and generate maximally localized Wannier functions (MLWFs) [65, 66, 67]. These MLWFs have many desired properties and have been applied to various problems. In this section, we briefly describe the procedure to generate MLWFs following similar notation to previous works.

Isolated bands

For an isolated band described by Bloch state $\psi_{n\mathbf{k}}(\mathbf{r})$, Wannier function $W_n(\mathbf{r}-\mathbf{R})$ or $|\mathbf{R}n\rangle$ is defined as

$$|\mathbf{R}n\rangle = \frac{V}{(2\pi)^3}\int d\mathbf{k}e^{-i\mathbf{k}\cdot\mathbf{R}}|\psi_{n\mathbf{k}}\rangle, \tag{2.9}$$

where V is volume of the real-space primitive cell. Since there can be an arbitrary phase $e^{i\phi_n(\mathbf{k})}$ with $\psi_{n\mathbf{k}}(\mathbf{r})$, the definition of the Wannier function is not unique.

For an isolated group of N interconnected composite bands (e.g., valence bands of an insulator), Bloch states can be mixed via a unitary transformation in addition to the arbitrary phases. Multiplying by an phase factor can be also seen as a unitary transformation. Then the generalized definition of Wannier functions is

$$|\mathbf{R}n\rangle = \frac{V}{(2\pi)^3}\int d\mathbf{k}e^{-i\mathbf{k}\cdot\mathbf{R}}\sum_{m=1}^{N} U_{mn}^{\mathbf{k}}|\psi_{m\mathbf{k}}\rangle, \tag{2.10}$$

where $U^{\mathbf{k}}$ is an $N\times N$ unitary matrix. Different $U^{\mathbf{k}}$ can lead to distinct Wannier functions with different spatial shapes.

To remove the arbitrariness, maximally localized Wannier functions are generated through minimizing the sum of quadratic spreads of Wannier functions, which is defined as

$$\Omega = \sum_n \langle(\mathbf{r}-\bar{\mathbf{r}}_n)^2\rangle_n = \sum_n [\langle r^2\rangle_n - |\bar{\mathbf{r}}_n|^2], \tag{2.11}$$

where $\bar{\mathbf{r}}_n = \langle\mathbf{r}\rangle_n = \langle\mathbf{0}n|\mathbf{r}|\mathbf{0}n\rangle$ and $\langle r^2\rangle_n = \langle\mathbf{0}n|r^2|\mathbf{0}n\rangle$. This spread functional can be further separated into two parts

$$\Omega = \Omega_I + \tilde{\Omega}, \tag{2.12}$$

where

$$\Omega_I = \sum_n\left[\langle r^2\rangle_n - \sum_{\mathbf{R}m}|\langle\mathbf{R}m|\mathbf{r}|\mathbf{0}n\rangle|^2\right], \tag{2.13}$$

and

$$\tilde{\Omega} = \sum_{n} \sum_{\mathbf{R}m \neq \mathbf{0}n} |\langle \mathbf{R}m|\mathbf{r}|\mathbf{0}n\rangle|^2. \tag{2.14}$$

These two terms are both non-negative and Ω_I is independent of changes in $U^{\mathbf{k}}$, or gauge invariant [65]. Hence minimizing Ω with respect to $U^{\mathbf{k}}$ is equivalent to minimizing $\tilde{\Omega}$.

MLWFs obtained through minimizing the spread functional have turned out to be always real in character, although they could be complex by definition [64]. In practice, this can be used as a good criterion to check if the minimization is well converged. In addition, MLWFs are proven to be exponentially localized and can be used as localized complete basis in linear-scaling approach and transport problems [68]. Furthermore, MLWFs provide insightful information on chemical bonding which is hard to extract from the Bloch representation [64]. Finally, the centers of MLWFs can be interpreted as the coordinates of electrons, which provides valuable connection to modern polarization theory [64, 69].

Entangled bands

In some system (e.g., metals and conduction bands of insulators), the energy bands we are interested in are entangled with other irrelevant energy bands. A “disentanglement” procedure is needed to pick out the “right” energy bands before trying to obtain MLWFs for these entangled bands using the method for isolated bands described in the previous section. For instance, the s band of copper is mixed with the five d bands, so we need to separate the s band from the d bands before generating MLWFs with s characteristics. The standard procedure for disentanglement is as follows.

Assume we want to generate MLWFs from N energy bands that are entangled with other bands. To perform the disentanglement procedure and obtain N smooth bands, we choose an energy window (“outer window”) which includes $N^{\mathbf{k}}_{win}$ eigenvalues at $\mathbf{k}$ and make sure $N^{\mathbf{k}}_{win} \geq N$ for any kpoints. A set of N orthonormal Bloch states is obtained at each kpoint through the following transformation of all original eigenstates that fall in the energy window:

$$|\psi^{opt}_{n\mathbf{k}}\rangle = \sum_{m \in N^{\mathbf{k}}_{win}} V^{\mathbf{k}}_{mn} |\psi_{m\mathbf{k}}\rangle, \tag{2.15}$$

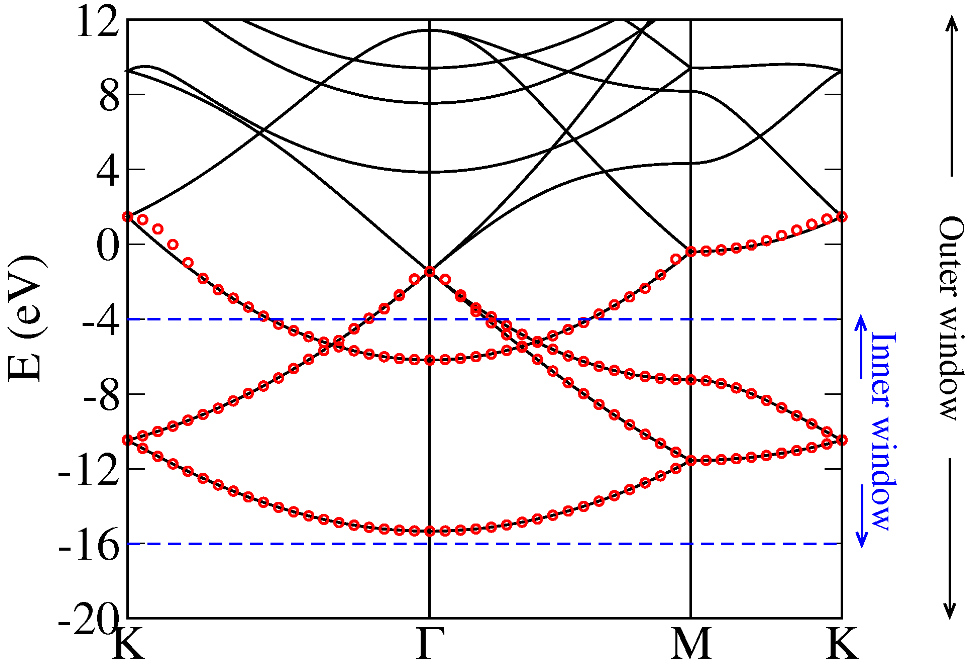

Figure 2.1: Illustration of outer and inner energy windows when generating 4 MLWFs for the flat triangular sheet from entangled bands. Black solid lines are bands calculated from a planewave basis and red circles are bands calculated using MLWFs.

where $V^{\mathbf{k}}_{mn}$ is a $N^{\mathbf{k}}_{win} \times N$ matrix and satisfies $\{V^{\mathbf{k}}\}^{\dagger} V^{\mathbf{k}} = \mathbb{I}$. Generating MLWFs for entangled bands is then a two-step procedure. First we need to choose $V^{\mathbf{k}}$ to get a reasonable $|\psi^{opt}_{n\mathbf{k}}\rangle$. Once we have $|\psi^{opt}_{n\mathbf{k}}\rangle$, we can follow the procedure described in the previous section to obtain MLWFs from $|\psi^{opt}_{n\mathbf{k}}\rangle$. Specifically, Ω_I and $\tilde{\Omega}$ are calculated with $|\psi^{opt}_{n\mathbf{k}}\rangle$ plugged in. From the previous section, we know that Ω_I is gauge invariant and is independent of $U^{\mathbf{k}}$. For entangled bands, Ω_I is then determined by $V^{\mathbf{k}}$, and $\tilde{\Omega}$ depends on both $U^{\mathbf{k}}$ and $\tilde{\Omega}$. To achieve minimal total spreads for Wannier functions, it is rational to minimize Ω_I with respect to matrices $V^{\mathbf{k}}$, which serves as the disentanglement procedure. Hence, a two-step minimization procedure is needed to generate MLWFs for entangled bands – first minimize Ω_I with respect to $V^{\mathbf{k}}$ to obtain disentangled bands, then minimize $\tilde{\Omega}$ with respect to $U^{\mathbf{k}}$ to obtain MLWFs [66].

With the disentanglement procedure, the MLWFs obtained will not necessarily reproduce the original energy bands since they may span different subspaces. However, in most cases, at least certain portions of the energy bands should be reproduced exactly (e.g., energy bands around the Fermi level in electron transport problems). To reproduce certain energy bands, in addition to the outer energy window, we can apply an inner energy window during the disentanglement procedure and make sure that all Bloch states inside the inner window are used without mixing them with other states outside the inner windows [66]. In Figure 2.1, we illustrate inner and outer energy windows with a flat triangular boron sheet. We calculate energy bands from MLWFs [67, 70] and compare them to plane-wave calculations. We can see that energy bands within the inner windows are reproduced exactly with MLWFs.

Applications

In our research, we have used MLWFs to analyze the chemical bonding in boron sheets. In two-dimensional boron sheets, the chemical bonding is mixed two-center and three-center type which is difficult to analyze using traditional concepts and tools. MLWFs are able to show explicitly the "positions" of electrons (or electron pairs) and provide insightful information on the chemical bonding in boron sheets. With MLWFs we can identify bonding patterns and observe directly the mixing of two-center and multi-center bonding [7].

On the other hand, charge transfer has been an ill-defined quantity in first-principles calculations because it is difficult to assign electrons to different atoms due to the fact that atomic orbitals are no longer the eigenstates of the system Hamiltonian. The Löwdin method has been widely used by researchers, where one projects wavefunctions onto orthogonalized atomic orbitals [71, 72]. However, because orthogonalized atomic orbitals are usually not localized and tend to extend to regions far from the corresponding atoms, the Löwdin method usually results in too small a charge transfer between atoms. Since MLWFs are a localized orthonormal complete basis, we assign electrons to MLWFs by projecting wavefunctions to MLWFs and calculate the projected density of states on Wannier function $|\mathbf{0}m\rangle$

$$N_m(E) = \sum_{n\mathbf{k}} \delta(E - \epsilon_{n\mathbf{k}}) \big| \langle \psi_{n\mathbf{k}} | \mathbf{0}m \rangle \big|^2 \tag{2.16}$$

By integrating the projected density-of-states up to the Fermi level, we can calculate the number of electrons associated to a Wannier function. In our Mg boride system, we can easily assign Wannier functions to Mg and boron subsystem by inspection. We take the number of electrons on Mg associated Wannier functions as the number of electrons on the Mg atom and calculate the charge transfer from Mg to boron. Because MLWFs are a localized basis, the calculated charge transfer is larger than the value from Löwdin method and is much more reasonable, as shown in our work [7].

2.4 Genetic algorithm

Structure prediction using numerical computation is a long-standing and difficult problem in materials science. For a given number and species of atoms, we would like to know what is the most stable structure made of these atoms. To accomplish this, we need to minimize the free energy of the system with respect to all atomic coordinates and unit cell parameters. In the multi-dimensional phase space made of all structural parameters, the free energy surface consists of "valleys" and "hills" which are connected by saddle points. Each valley acts as a local basin of attraction, and any local minimization methods such as conjugate gradients can only find a local minimum lying in a basin which is not necessarily the global minimum.

To find the global minimal point instead of local, various stochastic methods have been proposed including simulated annealing [73], basin hopping [74, 75], random searching [76] and genetic algorithms [77, 78, 79], which allow us to find the global minimum with certain probabilities. Among these methods, genetic algorithms are rather promising due to their fast convergence and capability to deal with systems of up to 40 atoms at present [77, 78, 79]. Genetic algorithms were first proposed as a numerical method to find global minima for general questions. They simulate the process of evolution which involves reproduction through crossover of genes from parents and mutation through random changes of genes. In addition, they allow competition between individuals in each generation, which guarantees "survival of the fittest". When adapted to predicting the optimal structure with first-principles calculations, the basic procedure of the genetic algorithm is as follows. First, starting with a set of randomly generated structures, we relax each structure to the corresponding local minimum using standard techniques in first-principles calculations.

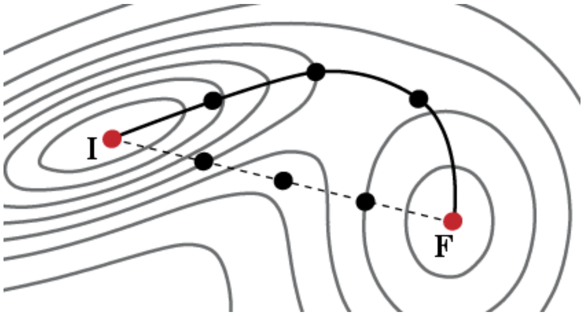

Figure 2.2: Illustration of the nudged elastic band method [80]. The initial (I) and the final (F) states are two local minima of the energy surface. To determine the MEP between I and F, an initial guess of the reaction path (dashed line) is constructed by connecting the initial and the final states. A number of images of the system (black solid circles) are positioned along the path. The initial path is then optimized to yield the MEP (solid line) on the energy surface.

Second, we choose a certain number of lowest-energy structures after relaxation (discarding the remaining ones) and use these as parents to randomly generate offspring through crossover and mutation. Then these new structures are passed on to compete in the next generation by relaxing them to local minima and comparing their total energies. Finally, the above process is iterated until convergence criteria are satisfied or a maximum number of iterations (generations) is reached. The genetic algorithm can be easily adapted to studying two-dimensional sheet structures and one-dimensional nanotubes. Further details of genetic algorithms are in Appendix A.

2.5 Nudged elastic band method

In condensed matter physics, it is important to find the minimum energy path (MEP) for a system going from one configuration to another. The highest energy point in the path then determines the energy barrier for the transition. This point is a saddle point which is maximal along one direction but is minimal along all others. Usually multiple maxima can exist in the MEP and hence the overall shape of MEP must be well estimated to obtain the energy barrier. Various methods have been proposed to find the MEP among which the nudged elastic band (NEB) method is the most robust and efficient one to date [81, 82, 83, 84].

The idea behind NEB is quite simple. A number of images (or replicas) of the system are generated between the initial and the final configurations to create a guess of the reaction path (see Figure 2.2). Each image is a replication of the system with different atomic coordinates. Usually these initial images are generated via linearly interpolating the atomic coordinates from the initial configuration to the final one. To generate a continuous reaction path, these images are connected with elastic springs. While holding the initial and the final configurations fixed, the intermediate images are optimized to generate the MEP.

Two different types of forces exist on each image: forces from the elastic springs and real forces from the atomic interactions within the image. The elastic forces are defined to be tangential to the path, while real forces can be along any direction. To avoid images collapsing to local minima (the initial or the final state), the projection of the real forces tangential to the path is zeroed out. Suppose we have $N+1$ images $\mathbf{R}_i$ $(i = 0, ..., N)$ with $\mathbf{R}_0$ and $\mathbf{R}_N$ being the initial state and the final states, respectively. These images are connected with elastic springs with elastic constant K and zero initial length. The force on image i is given by

$$\mathbf{F}_i = \mathbf{F}_i^s - \nabla E(\mathbf{R}_i)|_\perp, \tag{2.17}$$

where $\mathbf{F}_i^s$ is the spring force given by

$$\mathbf{F}_i^s = K(|\mathbf{R}_{i+1} - \mathbf{R}_i| - |\mathbf{R}_i - \mathbf{R}_{i-1}|)\hat{\tau}_i, \tag{2.18}$$

with $\hat{\tau}_i$ being the unit tangent vector for image i, and $-\nabla E(\mathbf{R}_i)|_\perp$ is the real force perpendicular to $\hat{\tau}_i$

$$-\nabla E(\mathbf{R}_i)|_\perp = -\nabla E(\mathbf{R}_i) - (-\nabla E(\mathbf{R}_i) \cdot \hat{\tau}_i)\,\hat{\tau}_i \tag{2.19}$$

With forces given by Equation (2.17), a standard minimization technique can be used to optimize the intermediate N-1 images and obtain the MEP.

Chapter 3

Boron nanostructures

As the neighbor of carbon in the periodic table, we had expected that nanostructures of boron might resemble carbon. However, because boron has only three valence electrons instead of four and is electron deficient, it is impossible for boron to make regular covalent bonding like carbon. Instead boron prefers three-center or even multi-center bonding due to electron deficiency. Hence boron nanostructures tend to have complex geometries which are unique for boron and are not observed in any other materials. In this chapter, we present geometries of boron nanostructures and describe their bonding and electronic properties.

3.1 Single-layered boron sheets

3.1.1 Structures

We start with discussing the structures of two-dimensional boron sheets we discovered. We define the binding energy as

$$E_b = E_{at} - E_{sheet}, \tag{3.1}$$

where E_{at} is the energy of an isolated spin-polarized boron atom and E_{sheet} is the energy per atom of a sheet. With our definition, E_b is always positive and larger E_b corresponds to a more stable structure. Table 3.1 shows binding energy and geometrical data of our most stable boron sheet (α sheet in Figure 3.1) along with three other boron sheets: the flat triangular sheet, the buckled triangular sheet and the hexagonal sheet [36, 38, 39]. The

Table 3.1: Binding energies E_b (in eV/atom) and geometric parameters (in Å) of four boron sheets: the flat and buckled triangular sheets, the hexagonal sheet, and one of our sheets (α in Figure 3.1). d^{flat} is the bond length of the flat triangular sheet. d^{σ} and d^{diag} are the bond lengths of the buckled triangular sheet, d^{σ} is between atoms with the same z, while d^{diag} is between atoms with different z. Δz is the buckling height. d^{hex} is the bond length for the hexagonal sheet. d^{new} gives the bond length range of sheet α.

	Flat triangular		Buckled triangular			
	E_b	d^{flat}	E_b	d^{σ}	d^{diag}	Δz
LDA	6.58	1.68	6.74	1.59	1.80	0.81
previous LDA[38]	6.76	1.69	6.94	1.60	1.82	0.82
previous LDA[36]	6.53	-	6.79	-	-	-
GGA	5.79	1.70	6.00	1.60	1.86	0.88
previous GGA[39]	5.48	1.71	5.70	1.61	1.89	-

	Hexagonal		Sheet α	
	E_b	d^{hex}	E_b	d^{new}
LDA	5.82	1.65	6.86	1.64-1.67
GGA	5.25	1.67	6.11	1.66-1.69
previous GGA[39]	4.96	1.68	-	-

hexagonal sheet is unstable with respect to in-plane shearing distortion, so we obtain the tabulated values by maintaining hexagonal symmetry while optimizing the bond length. Our calculations on triangular and hexagonal sheets agree very well with previous work [36, 38, 39]. The buckled triangular sheet is more stable than the flat one by 0.16 eV/atom due to the former structure forming stronger σ bonds along the buckled direction [38]. We also can reproduce previous results on boron nanotubes made from triangular sheets [36, 38].

Figure 3.1 shows two examples of our boron sheets which are more stable than the buckled triangular sheet by 0.12 (α sheet) and 0.08 (β sheet) eV/atom, respectively. These boron sheets are metallic and are composed of mixtures of hexagons and triangles. Sheet α is the most stable structure in our library. With a flat triangular sheet as a template, these boron sheets can be constructed by removing atoms from the template. Each removed atom produces a hexagonal hole generating a mixture of hexagons and triangles. We define a "hexagon hole density" as

$$\eta = \frac{\text{No. of hexagon holes}}{\text{No. of atoms in the original triangular sheet}}. \tag{3.2}$$

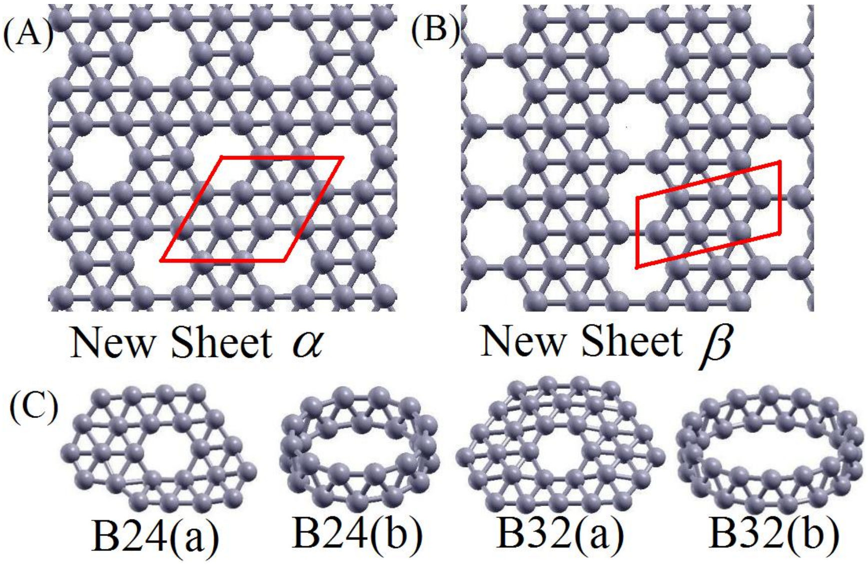

Figure 3.1: (A, B) Two examples of our boron sheets (top view). Red solid lines show the unit cells. (C) Four boron clusters: $B_{24}(a)$ and $B_{32}(a)$ are clusters with hexagonal holes; $B_{24}(b)$ and $B_{32}(b)$ are the double-ring clusters from refs. [27, 29]. Gray balls are boron atoms, and gray "bonds" are drawn between nearest neighbors.

In brief, η is the fraction of atoms removed from a triangular sheet that yields a desired sheet. The triangular sheet has η=0, the hexagonal sheet has η=1/3, and sheets α and β have η of 1/9 and 1/7, respectively. From now on, we name boron sheets using a capital letter followed by the η value. T(0) is flat triangular, H(1/3) is hexagonal (*i.e.* graphitic), A(1/9) is the most stable α sheet, and B(1/7) is β sheet.

A priori, the energies of these sheets can depend on both η and the pattern of hexagons. This results in a huge phase space of hexagonal patterns for a given η. It turns out that η is the major factor determining the stability of boron sheets and E_b has relatively small variations with the pattern of hexagons, especially for stable boron sheets. We have discovered that the most stable structures occur when the hexagons are distributed as evenly as possible at fixed η. Figure 3.2 shows the LDA binding energies E_b versus η for this class of structures. E_b reaches a maximum of 6.86 eV/atom at η=1/9, which corresponds to the α sheet. In addition, we have investigated the other extreme where hexagons form lines whose binding energies are also shown in Figure 3.2. For the linearly aligned hexagons, the most stable structure occurs at η = 1/7 (sheet β), which is 0.03 eV/atom less stable than the α sheet. Although sheets with hexagon lines are more stable

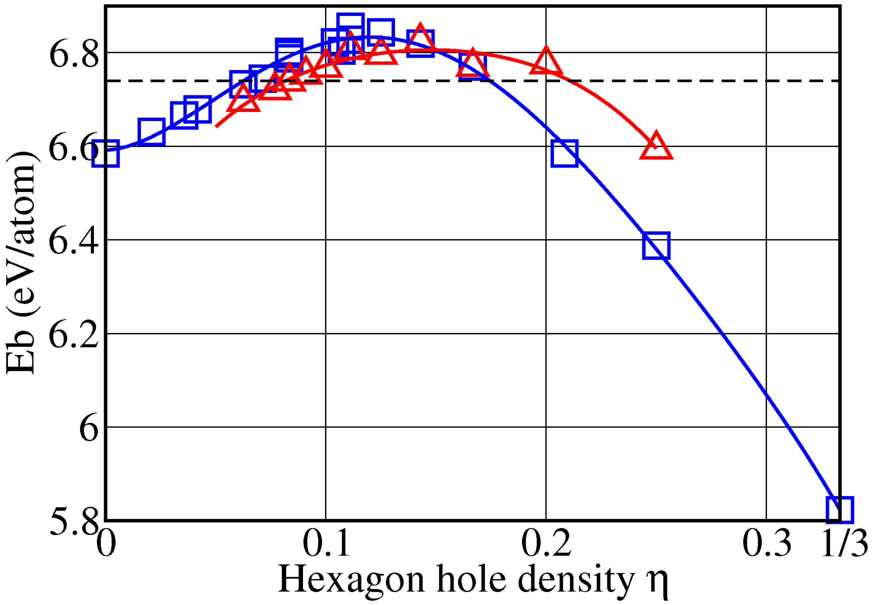

Figure 3.2: LDA binding energy E_b versus hexagon hole density η for single-layered boron sheets in two extreme cases. The blue '□' are the calculated binding energies for the case where hexagons are evenly distributed. The red '△' are the calculated binding energies for the case where hexagons form lines. The solid curves are from polynomial fitting. The dashed line shows E_b for the buckled triangular sheet. The two limiting cases $\eta = 0$ and $\eta = 1/3$ correspond to the flat triangular and hexagonal sheets, respectively. Maximum E_b occurs for sheet α ($\eta = 1/9$).

for $\eta \geq 1/5$, boron sheets with evenly distributed hexagons are more favorable for η close to 1/9. In this work, since we concentrate primarily on the most stable boron nanostructures, we will be primarily interested in studying the properties of boron sheets with evenly distributed hexagons.

These findings on boron sheets have important ramifications for boron clusters. The α sheet can be considered as the precursor of B_{80} fullerene [30] just like graphene is the precursor of carbon fullerenes. We also have studied some clusters composed of mixtures of triangles and hexagons. Figure 3.1 shows the double-ring structures for B_{24} and B_{32} [27, 29] along with clusters constructed by us. The new B_{24} cluster with a hexagon hole is less favorable by 0.08 eV/atom, while the B_{32} is more favorable by 0.03 eV/atom than the corresponding double-ring. The stability of our sheets, of B_{80}, and our clusters with hexagonal holes suggests that, for boron systems with more than 20-30 atoms, the Aufbau principle [9] breaks down and a more general structural rule is required.

3.1.2 Bonding scheme

To explain the stability of these sheets, we now consider the nature of their electronic bonding. Generally, in-plane bonds formed from overlapping sp^2 hybrids are stronger than out-of-plane π-bonds derived from p_z orbitals, so a structure that optimally fills in-plane bonding states should be most preferable. Guided by this principle, Figure 3.3 shows projected densities-of-states (PDOS) for five boron sheets with separate in-plane (the sum of s, p_x and p_y) and out-of-plane (p_z) projections.

We begin with the hexagonal sheet, a textbook sp^2 bonded system. All sp^2 hybrids are oriented along nearest neighbor vectors so that overlapping hybrids produce canonical two-center bonds. A large splitting ensues between in-plane bonding and anti-bonding states. The p_z orbitals form their own manifold of bonding and anti-bonding states. The p_z PDOS vanishes at the transition point between the two. In the case of graphene, the four valence electrons per atom completely fill the sp^2 and the p_z bonding states, leading to a highly stable structure. However, a boron atom has only three valence electrons. As shown in Figure 3.3, some of the strong in-plane sp^2 bonding states are unoccupied, explaining the instability of this sheet. For our discussion below, this sheet is highly prone to accepting electrons to increase its stability should they be available from another source.

Next, we consider the flat triangular sheet. Each atom has six nearest neighbors but only three valence electrons. No two-center bonding scheme leads to a proper description. Previous work has noted qualitatively that a three-center bonding scheme exists here [38]. We now present a detailed model of the three-center bonding with crucial implications for the stability of our new sheets. Figure 3.4 shows a choice of orientations for the sp^2 hybrids where three hybrids overlap within an equilateral triangle formed by three neighboring atoms. For an isolated triangle, we have a simple 3×3 tight-binding problem with D_3 symmetry. Its eigenstates are dictated by group theory: one low-energy symmetric bonding orbital b and two degenerate high-energy anti-bonding orbitals a^*. (This is "closed" three-center bonding; details on this and other types of bonds are found in standard references [85].) These orbitals then broaden into bands due to inter-triangle couplings. Separately, the p_z orbitals also broaden into a single band (not shown). In Figure 3.3, the in-plane PDOS becomes zero at the energy separating in-plane bonding and anti-bonding states.

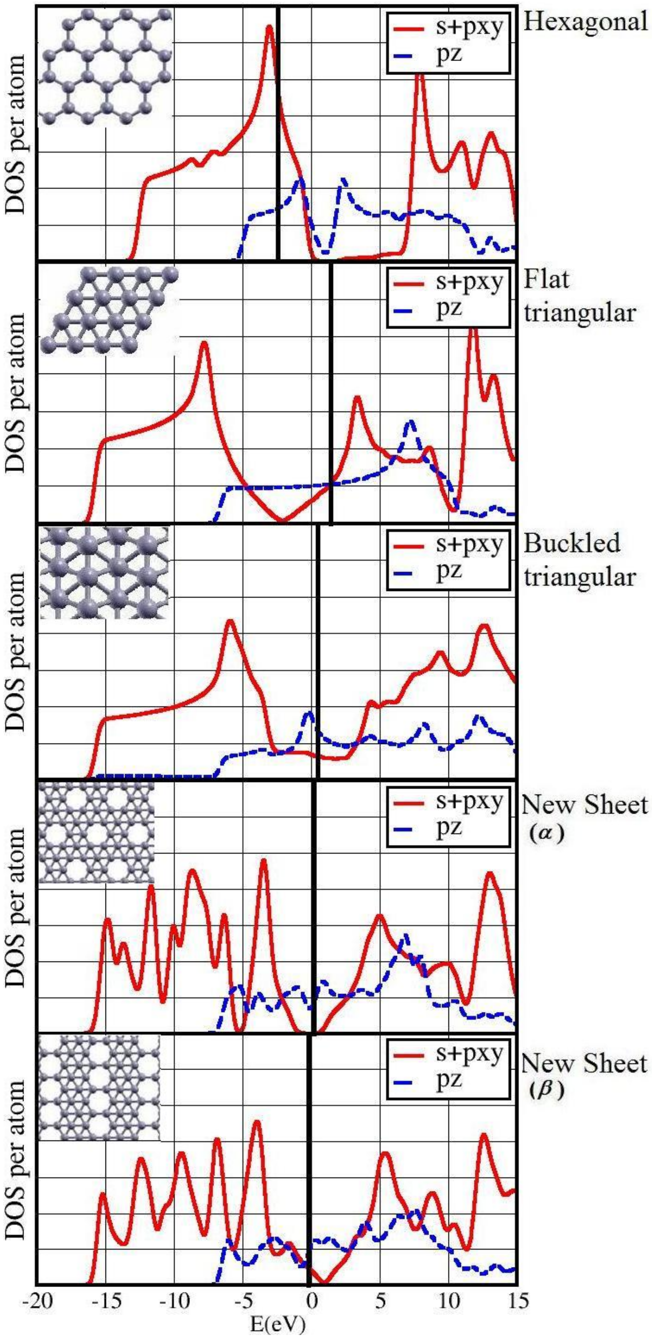

Figure 3.3: Projected densities-of-states (PDOS) for four boron sheets. Projections are onto in-plane (sum of s, p_x and p_y, solid red) and out-of-plane orbitals (p_z, dashed blue). Thick vertical solid lines show the Fermi energy E_F. (We use 0.3 eV of Gaussian broadening. The vertical scale is arbitrary.)

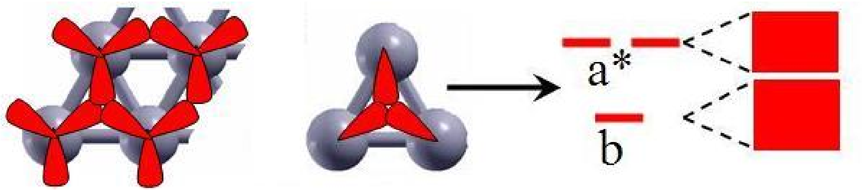

Figure 3.4: Three-center bonding scheme in flat triangular sheets. Left: orientation of sp^2 hybrids. Center and right: overlapping hybrids within a triangle (D_3 symmetry) yield one bonding (b) and two anti-bonding (a^*) orbitals. These then broaden into bands due to inter-triangle interactions.

Ideally this sheet would be most stable if: (i) two electrons per atom would completely fill the b-derived in-plane bonding bands, (ii) the anti-bonding a^*-derived bands were empty, and (iii) the remaining electron per atom would half fill the low-energy (bonding) portion of the p_z-derived band. This would mean that the E_F would be at the zero point of the in-plane PDOS in Figure 3.3. Clearly, this picture is a valid zeroth-order description. However, E_F lies slightly above the ideal position and makes some electrons occupy in-plane anti-bonding states. In other words, this sheet prefers to donate these high-energy electrons, which has critical implications below. (Although we seem to break symmetry by making half of the triangles filled and half empty, filling the entire b-derived in-plane bonding band makes all hybrids equally occupied. This restores full in-plane symmetry: *i.e.*, the two possible initial orientations of hybrids give the same final state.)

The flat triangular sheet, however, buckles under small perturbations along z [36]. The buckling mixes in-plane and out-of-plane states and can be thought of as a symmetry reducing distortion that enhances binding. As shown in Figure 3.3, some states move below E_F as indicated by the small peak immediately below E_F.

Finally, we turn to the new structures. The above discussion has shown that the hexagonal sheet should be able to lower its energy by accepting electrons, while the flat triangular structure has a surplus of electrons in anti-bonding states. From a doping perspective, the three-center flat triangular regions should act as donors while the two-center hexagonal regions act as acceptors. Thus if the system is able to turn into a mixture of these two phases in the right proportion, it should benefit from the added stability of both subsystems. Specifically, the hexagon-triangle mixture with the highest stability should place E_F precisely at the zero-point of in-plane PDOS, filling all available in-plane bonding states and none of the anti-bonding ones. The remaining electrons should fill the low-energy p_z-derived states, leading to a metallic system. These expectations are born out clearly in Figure 3.3 as well as by the energetic stability of the structures (Figure 3.2). In fact, the most stable sheet α satisfies this condition precisely, while the less stable sheet β has a slight shift of E_F from the ideal position.

3.1.3 Self-doping

From our analysis of the bonding in boron sheets, we know that boron atoms in the triangular regions act like electron donors. In this section, we will show explicitly how the doping works and discuss its consequences and applications.

Previously, we discovered that the α sheet, or the A(1/9) sheet, is most stable due to the optimal filling of σ bonds: electrons fill all in-plane bonding σ states while leaving all in-plane anti-bonding σ^* states empty, and any remaining electrons partially fill out-of-plane π states [6]. The fact that σ bonds are stronger than π bonds explains why the best structures are determined by optimal filling of the in-plane manifold. Following this philosophy, we count the number of in-plane and out-of-plane states for many boron sheets to identify trends.

We begin with a large M-atom T(0) sheet and gradually remove atoms: each removal leaves behind a hexagonal hole. For each structure obtained, we calculate the densities-of-states (DOS) projected onto in-plane and out-of-plane states; mathematically, this means projection onto even and odd parity states with respect to reflection in the sheet plane. We identify the separation energy E_{sep} of in-plane bonding σ and anti-bonding σ^* states as the energy where the in-plane DOS has a zero (we have checked the validity of this criterion in a few cases by manually plotting wave functions and checking their character in detail). By integrating the in-plane DOS $D_\sigma(\epsilon)$ and out-of-plane DOS $D_\pi(\epsilon)$, we calculate (i) N_σ – the number of in-plane σ bonding states with energy below E_{sep}

$$N_\sigma = \int_{-\infty}^{E_{sep}} d\epsilon \, D_\sigma(\epsilon), \tag{3.3}$$

and (ii) N_π – the number of out-of-plane π states with energy below E_{sep}

$$N_\pi = \int_{-\infty}^{E_{sep}} d\epsilon \, D_\pi(\epsilon) \,. \tag{3.4}$$

The number of electrons is given by integrating the total DOS up to the Fermi energy E_F:

$$N_e = 2 \int_{-\infty}^{E_F} d\epsilon \, [D_\sigma(\epsilon) + D_\pi(\epsilon)] = 3M(1-\eta) \,. \tag{3.5}$$

where the factor of two accounts for spin and the form $3M(1-\eta)$ comes from the fact that each boron atom has 3 valence electrons and removing atoms from the original T(0) sheet reduces the number of atoms by a proportion of η (which is justified by the definition of η).

A configuration should be optimal if electrons fill all the in-plane bonding states and leave all the in-plane anti-bonding states empty, with partial occupancy of the π manifold. This simply means $E_F = E_{sep}$ or equivalently

$$2(N_\sigma + N_\pi) = N_e = 3M(1-\eta) \,, \tag{3.6}$$

Note that Equation (3.6) is a constraint on the sheet structure (*i.e.* the η value) and will hold only for particular sheets that are highly stable.

Based on first principles calculations, we have discovered that N_σ and N_π are smooth functions of η. Figure 3.5 shows the behavior of N_σ and N_π versus η for a large collection of boron sheets. As we can see, N_σ/M is precisely unity for all η, and N_π/M always hovers around 1/3. When plugging $N_\sigma = M$ and $N_\pi = M/3$ into Equation (3.6), we find the simpler relation

$$2(M + M/3) = 3M(1-\eta) \,. \tag{3.7}$$

The solution to this equation is $\eta = 1/9$ which is precisely the η value for the most stable A(1/9) or α sheet.

The results shown in Figure 3.5 are surprising: the number of in-plane bonds remains constant even as we add or remove boron atoms from the boron sheet. Since the inter-atomic distances are essentially fixed when η changes [6], adding or removing atoms directly

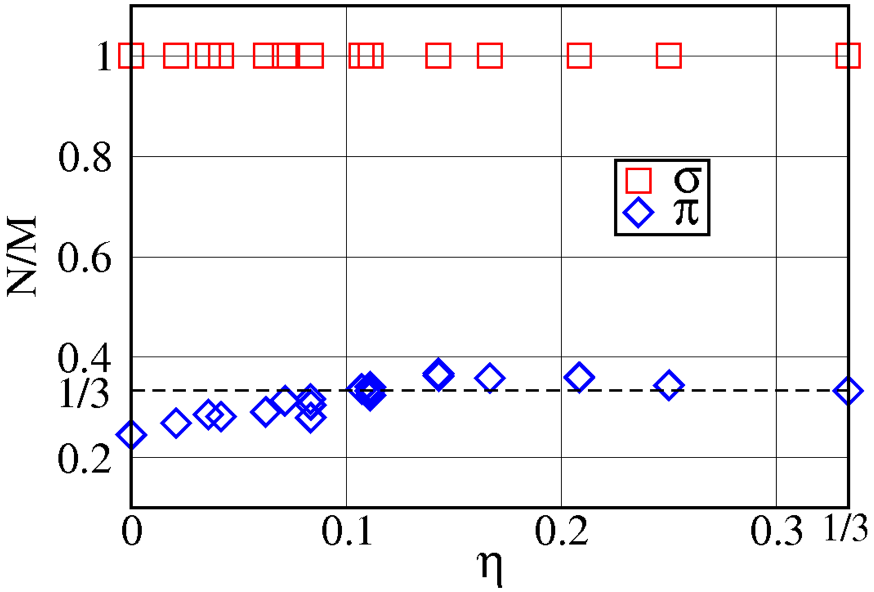

Figure 3.5: N_σ/M & N_π/M versus η. All data are extracted from *ab initio* plane-wave calculations, red □ for σ and blue ♢ for π states. The horizontal black dashed line shows $N/M = 1/3$.

changes the areal density of boron atoms. Naively, we would have expected a higher areal density of atoms to result in a higher density of bonding states. We discuss the reason for this behavior next.

Chemical bonding from Wannier functions

By investigating the chemical bonding in 2D boron sheets using maximally localized Wannier functions (MLWFs) [65, 66, 67], we can explain the surprising results on constant number of bonds. We consider the evolution of MLWFs when boron sheets change from hexagonal to triangular. For example, Figure 3.6(a) shows how a six-atom unit-cell of H(1/3) evolves under addition of boron atoms into mixed-phase D(2/9), A(1/9), and finally T(0). As per Figure 3.5 and detailed analysis of the band structures, all four sheets are found to have 9 σ bonding bands. For each sheet, we calculate MLWFs for the lowest 12 bands and obtain 9 in-plane (σ) and 3 out-of-plane (π) MLWFs. We reproduce the 9 σ bonding bands in each case by imposing an inner window [66].

For in-plane states, each sheet has one or two unique types of σ MLWFs due to symmetry (the others are obtained by symmetry operations). We show representative σ MLWFs

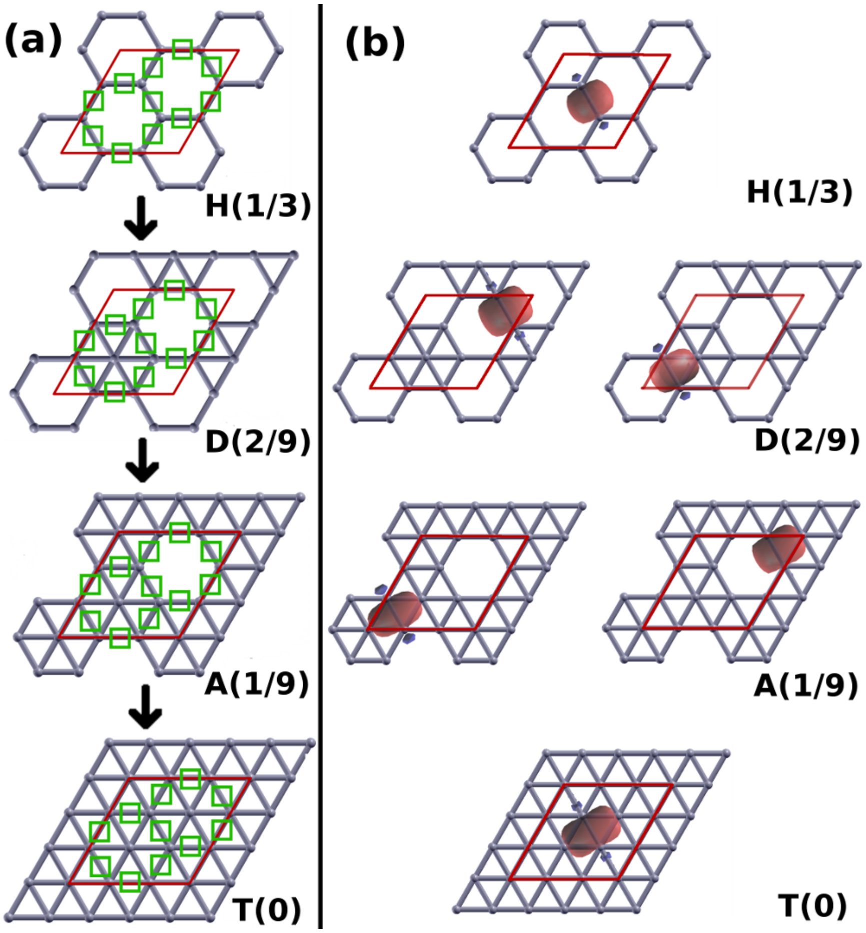

Figure 3.6: (a) Evolution of boron sheets from H(1/3) to D(2/9), A(1/9), and finally T(0): Green '□' mark the centers of σ MLWFs. (b) Isosurface contour plots of representative σ MLWFs for H(1/3), D(2/9), A(1/9) and T(0), respectively: Red for positive, blue for negative values; other σ MLWFs are obtained by symmetry. Red solid lines show unit cells.

for each sheet in Figure 3.6(b). Sheet H(1/3) has 9 identical MLWFs localized in the middle of two adjacent atoms, *i.e.* two-center bonding. At the other extreme, sheet T(0) is three-center bonded [6], and we find that it can be described using two different sets of MLWFs: (i) triangular-shaped σ MLWFs centered in the centers of triangles indicating explicitly three-center bonding as shown in Figure 3.7(a), or (ii) σ MLWFs shown in Figure 3.6(b) and Figure 3.7(b) which are centered between adjacent atoms and symmetrically spread to triangles on both sides. These two sets of MLWFs span the same subspace, generate identical band structures, and thus describe the same physics of three-center bonding.

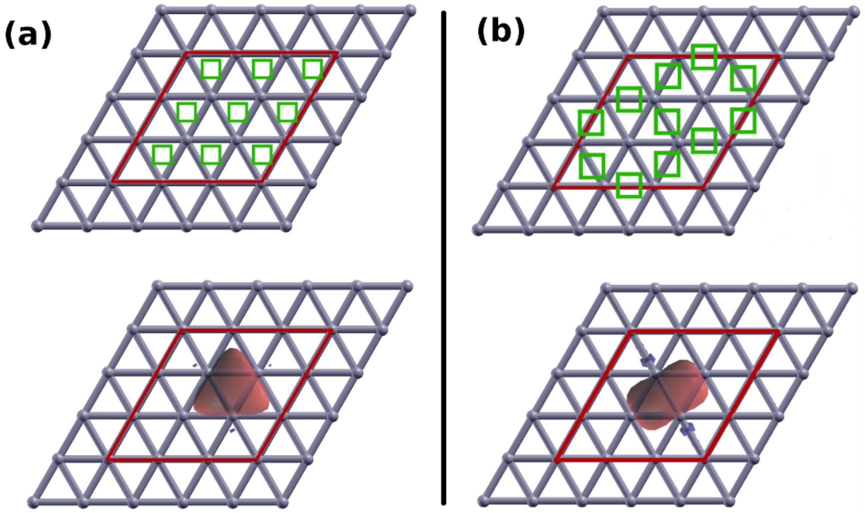

Figure 3.7: Centers (marked by green '□') & Isosurface contour plot (red for positive, and blue for negative values) of two sets of σ MLWFs for T(0) boron sheet: (a) Triangular-shaped, (b) rectangular-shaped. These σ MLWFs are even with respect to reflection in the plane of the boron sheets. Red solid lines show the unit cells.

We use group (ii) because it shows the most consistent evolution with η below. The two intermediate sheets D(2/9) and A(1/9) each have two types of σ MLWFs. For D(2/9), the first type is similar to that of H(1/3) as it is centered between a B-B pair in a hexagonal environment, while the other is asymmetric and spreads towards the neighboring triangular region, *i.e.* mixing of two- and three-center character. For A(1/9), the first type is in a triangular environment and resembles that of T(0), while the other is asymmetric in the same manner as D(2/9).

After looking at the figures, the main observation is that despite large changes of sheet structure and atomic areal density, the same number of σ MLWFs are basically centered at the same sites as in H(1/3) while showing minor shifts in some cases. Thus, during the evolution of the sheet from hexagonal to triangular, the basic in-plane bonding pattern and number of bonds of the hexagonal system is retained with some minor perturbations in shape and position. (We have checked that these results are general and not restricted to the sheets discussed here.)

Turning to out-of-plane states, due to symmetry the three π MLWFs of a given sheet are identical and can be transformed into each other by simple translation and rotation. We show the representative π MLWFs for each sheet in Figure 3.8(a). For H(1/3), two sets

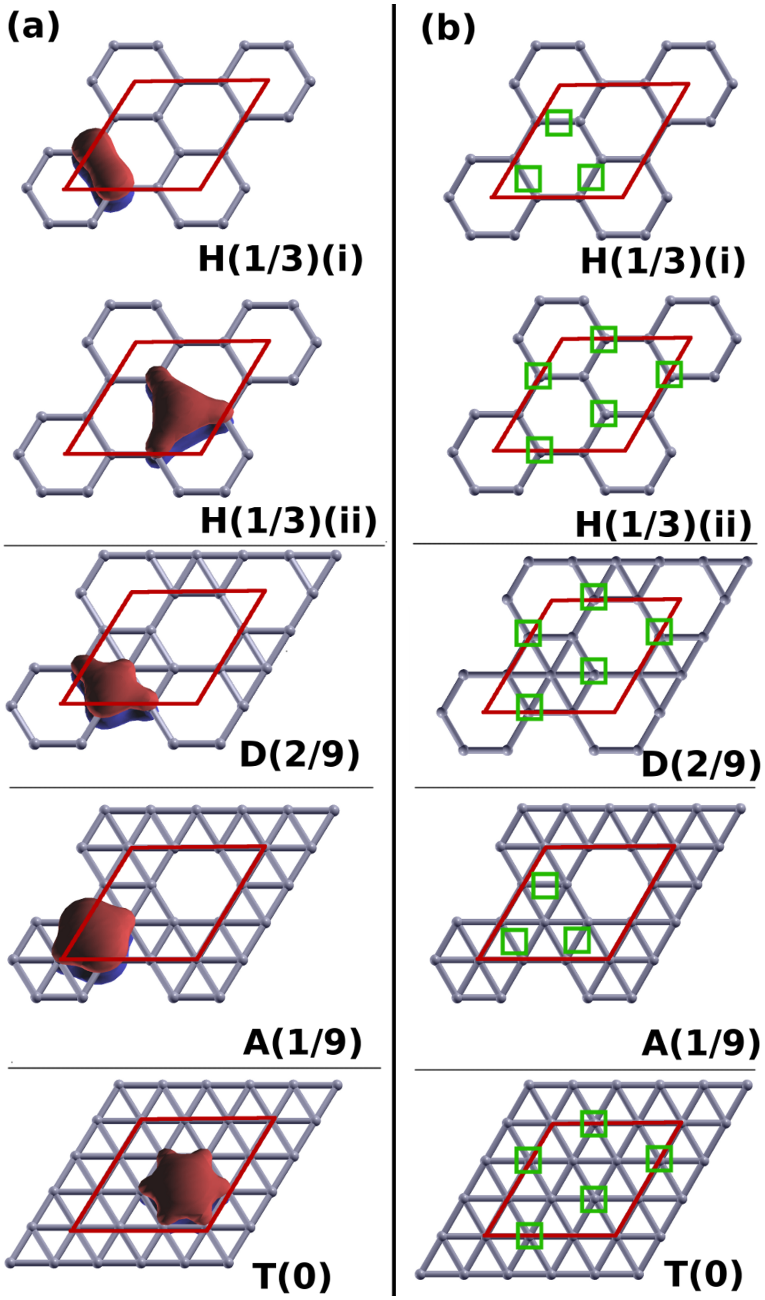

Figure 3.8: (a) Isosurface contour plots of representative π MLWFs for H(1/3), D(2/9), A(1/9) and T(0), respectively: Red for positive, blue for negative values; other π MLWFs are obtained by symmetry. These π MLWFs are odd with respect to reflection in the plane of the boron sheets. (b) Centers of π MLWFs shown by green '□'. Red solid lines show the unit cells.

of π MLWFs can be obtained depending on the choice of initial guess. These two sets of π MLWFs reproduce the same band structure, span the same subspace and thus describe the same physics. We label them H(1/3)(i) and H(1/3)(ii) in Figure 3.8. The π MLWF in H(1/3)(i) is peanut-like and centered in the middle of the B-B line connecting two boron atoms. On the other hand, H(1/3)(ii) is centered on a boron atom and spreads to its three nearest neighbors. For the other extreme, the sheet T(0), π MLWF is centered on a boron atom and spreads to its six nearest neighbors. The π MLWFs of the two mixed-phase sheets (D(2/9) and A(1/9)) differ from each other. For D(2/9), the MLWF is centered on a boron atom and spreads to four nearest neighbors, while for A(1/9), the MLWF is centered in the middle of a B-B pair and spreads to these two boron atoms and two other boron atoms in the two neighboring triangular regions. When looking at the centers of these π MLWFs, as shown in Figure 3.8(b), we discover that π MLWFs evolve with the structures of boron sheets in almost the same way as σ MLWFs. As we can see, sheets D(2/9) and T(0) have π MLWFs centered on the same sites as H(1/3)(ii), which are on every other atom of the H(1/3)'s lattice. On the other hand, sheet A(1/9) has π MLWFs centered on the same sites as H(1/3)(i), which are on every other B-B bonds of the H(1/3)'s lattice. Although we do not have all sheets sharing the same π MLWF centers like we have for σ MLWFs, we do have the bonding patterns of three sheets, D(2/9), A(1/9) and T(0), originating from the same parent system H(1/3). In details, the π manifolds of D(2/9) and T(0) originate from H(1/3)(ii), and that of A(1/9) originates from H(1/3)(i).

Self-doping and a general design rule

The above analysis leads to the following picture for boron sheets: adding a boron atom to fill a hexagonal hole in a 2D boron sheet does not change the number of bonding states but simply causes the three valence electrons of the added atom to be released into the lattice. In other words, adding a boron is equivalent to doping the original boron system with three more valence electrons. We call this unusual situation self-doping. Since 2D boron sheets are precursors of atomically thin boron nanotubes and fullerenes, self-doping is generally useful and applicable. For example, self-doping provides a general design rule for stable boron nanostructures. If we start with a stable graphene-derived carbon nanostructure with Z atoms containing many hexagon motifs, we could contemplate replacing all carbon with boron. However, to make a stable structure, we would need to add boron atoms since boron has only three valence electrons compared to carbon's four, and we need an extra electron per atom (Z extra electrons in total) to fill the bonding states. The solution is simple: if we fill the hexagon center sites with additional $Z/3$ boron atoms, they will each donate three electrons (exactly Z electrons in total) without changing the bonding states, making the structure iso-electronic to the original carbon system, and thus stabilize the final boron structure. This design rule explains the fact that the A(1/9) sheet and the stable B_{80} fullerene [30] can be derived from graphene and the C_{60} fullerene by filling hexagonal holes with extra atoms. Moreover, it explains why stable B_{80+8k} $(k \geq 0, k \neq 1)$ fullerenes can be built from the corresponding C_{60+6k} $(k \geq 0, k \neq 1)$ fullerenes [42]. Finally, our design rule also sheds light on the recently discovered new families of stable boron fullerenes [43, 44].

Self-doping applied in metal borides

Beyond pure boron nanostructures, self-doping provides a powerful tool for gaining a zeroth-order view of metal boride systems. In metal boride structures, we expect that the boron-boron bonding is much stronger than the metal-boron or metal-metal bonding. Furthermore, we expect the metal atoms to donate electrons to the boron subsystem. Therefore, a stable metal boride 2D sheet should have optimally filled boron bonds as a starting point.

Consider a MeB_x system where Me is a metal atom. Assuming that each metal atom donates y electrons to the boron subsystem and does not otherwise perturb the electronic structure, each boron atom now has on average $(3 + y/x)$ electrons and the total number of electrons for the boron subsystem is now

$$N_e = (3 + y/x)M(1 - \eta)\,. \tag{3.8}$$

As discussed in previous sections, optimal filling of the boron subsystem means $E_F = E_{sep}$ or equivalently $2(N_\sigma + N_\pi) = N_e$. Since we assume the electronic structure of the boron subsystem remains fixed after doping, we still assume that $N_\sigma = M$ and $N_\pi = M/3$. Therefore, to achieve the MeB_x system with optimal stability, the following constraint

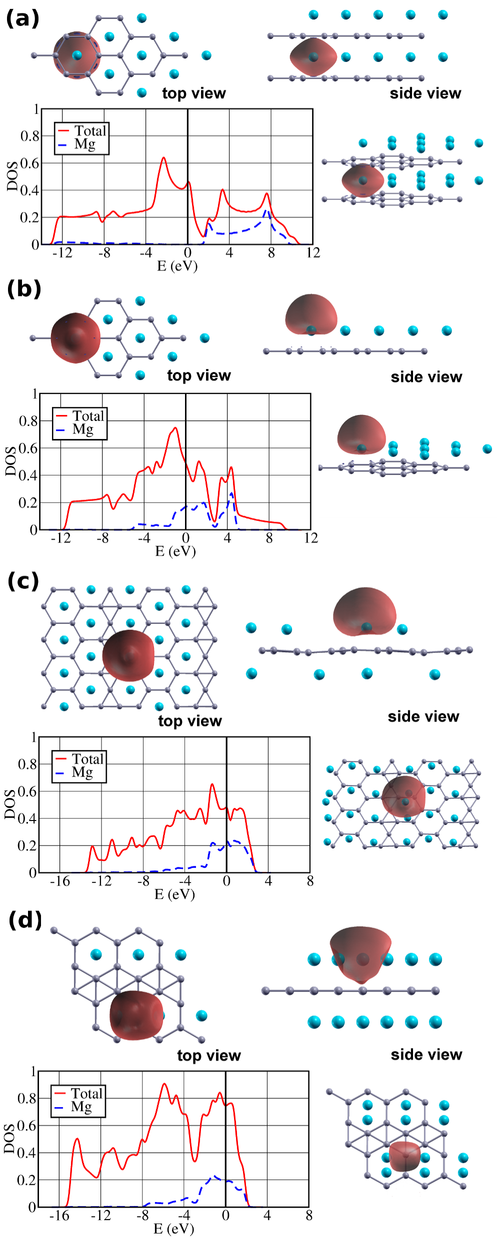

Figure 3.9: Isosurface contour plots of MLWFs associated with Mg (red for positive and blue for negative values), total DOS (red solid lines) and PDOS on Mg (blue dashed lines) for (a) MgB_2 bulk, (b) MgB_2 sheet derived from bulk, (c) MgB_2 sheet from a G(3/10) sheet, and (d) MgB_2 sheet based on an E(1/5) sheet. The charge transfers from Mg to B are (a) 1.82 e/Mg, (b) 1.37 e/Mg, (c) 1.05 e/Mg and (d) 0.62 e/Mg. For the MgB_2 sheet in (c), two types of MLWFs associated with Mg exist: we only show one of them while the other is similar to the one in (d). Small gray balls are boron, and large blue green balls are Mg. Fermi levels are at zero.

should be satisfied:

$$2(M + M/3) = (3 + y/x)M(1 - \eta_{optimal}). \tag{3.9}$$

The solution is

$$\eta_{optimal} = \frac{1 + 3y/x}{9 + 3y/x}. \tag{3.10}$$

Therefore, if we can estimate the charge transfer y, we estimate the optimal η for any x and thus greatly narrow down the search space for the most stable 2D metal boride structures.

Unfortunately, charge transfer is not easy to calculate precisely because there is no unique way to assign electrons to atoms. One popular way is to calculate Löwdin charges by projecting electronic states to orthogonalized atomic orbitals [71, 72]. However, Löwdin orbitals form an incomplete basis with long-ranged tails, and this method may lead to unreasonable charge transfer results. For instance, in bulk MgB_2, one rational way to explain its stability is that each Mg atom donates all its two valence electrons to the boron honeycomb lattice, making the boron lattice iso-electronic to graphene and stabilizing the structure. Following this explanation, which is consistent with our method based on the self-doping picture, we expect the charge transfer from Mg to boron to be essentially complete and close to 2 electrons per Mg. However, our Löwdin analysis gives only 0.76 e/Mg charge transfer. Therefore, in order to apply self-doping in metal boride systems, a new scheme that gives more reasonable charge transfer is necessary.

Here we propose to compute charge transfer by projecting wavefunctions onto MLWFs: these are an exponentially decaying, maximally localized, orthogonal and complete basis [65, 66, 67]. For Mg-B systems, we found it easy to assign MLWFs to Mg or B atoms by simple visual inspection. For bulk MgB_2, we calculate MLWFs for the 6 lowest bands, obtaining 5 MLWFs for B which are similar to those of H(1/3), and 1 MLWF around Mg (see Figure 3.9(a)). Projecting the DOS onto these MLWFs and integrating up to the Fermi energy gives a very reasonable charge transfer of 1.82 e/Mg, or approximately Mg^{2+}. Therefore, we believe that the MLWF-based charge transfer gives sensible values for our self-doping method and we use it to calculate charge transfer below.

Again, we would like to emphasize that, formally, charge transfer is an ill-determined

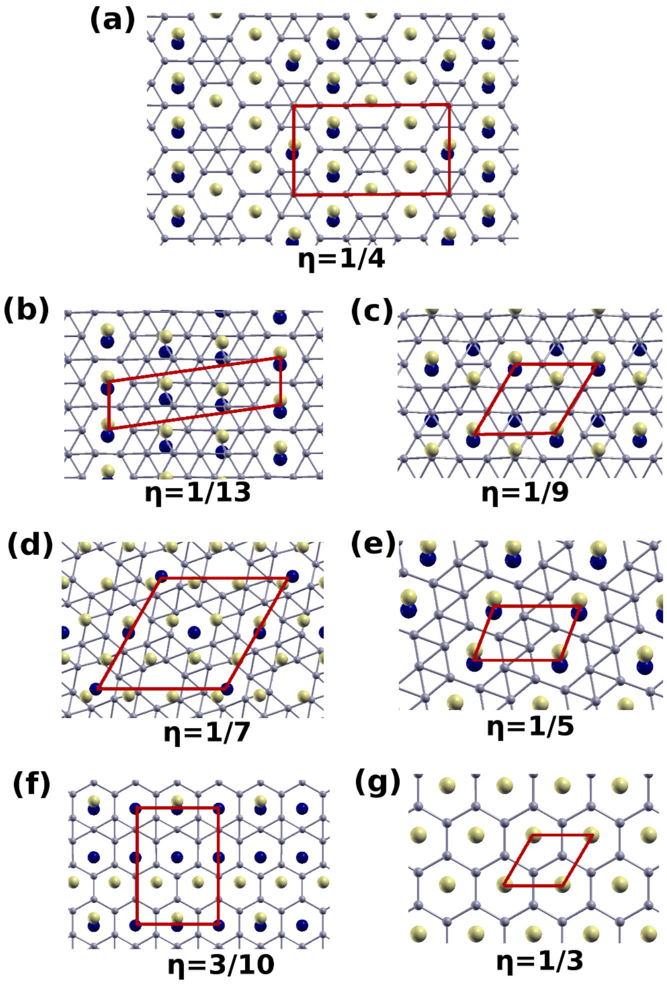

Figure 3.10: The most stable MgB_2 sheets for (a) $\eta = 1/4$, (b) $\eta = 1/13$, (c) $\eta = 1/9$, (d) $\eta = 1/7$, (e) $\eta = 1/5$, (f) $\eta = 3/10$ and (g) $\eta = 1/3$. The structure in (a) is the best MgB_2 sheet in our library. We display topviews that are rotated slightly around the horizontal (x) axis. Small gray balls are B, large light yellow balls are Mg lying above the boron plane, and large dark blue balls are Mg lying below the boron plane. Red solid lines show the primitive cells.

quantity depending on details of how it is defined and calculated. However, our main use of charge transfer will be to make zeroth-order *estimates* of $\eta_{optimal}$ in Eq. (3.10) in order to describe the basic properties of stable metal borides. For such an application, we believe that as long as the charge transfer can be reasonably defined — such as in our case involving a metal atom that is chemically expected to donate electrons to the boron subsystem — the overall approach will be useful.

We illustrate this approach based on self-doping for 2D atomically thin MgB_2 sheets. (Enlarging the project to other MgB_x stoichiometries is a future project.) Figure 3.9 shows three MgB_2 sheets: Figure 3.9(b) is the bulk-derived sheet structure with Mg on H(1/3), Figure 3.9(c) is based on a G(3/10) boron sheet, and Figure 3.9(d) is built from an E(1/5) boron sheet. These MgB_2 sheets are illustrated in Figures 3.10(e)-(g). The MLWF charge transfers are 1.37, 1.05 and 0.62 e/Mg, respectively, which are quite different from and clearly smaller than 1.82 e/Mg (the bulk MgB_2 value). This already suggests that the MgB_2 sheet structure derived from bulk will not be the most stable.

Furthermore, we notice that the charge transfers of three MgB_2 sheets are different from each other. Hence, the charge transfer y and the optimal η are interdependent quantities: rigorously, Equation (3.10) should be solved self-consistently in y and x. However, since the method is approximate and we wish to present a zeroth order view, we note that, very crudely, y hovers around unity. Using a guess of y=1 in Equation (3.10) yields $\eta_{optimal}$=5/21, which suggests that Mg placed on $\eta \approx 1/4$ boron sheets should create the most stable MgB_2 sheets.

To test this method, we construct many MgB_2 sheets by putting Mg on different boron sheets with a range of η. Figure 3.11 shows the energies of the best MgB_2 sheets we found for each η, and Figure 3.10 shows their atomic geometries. The optimal MgB_2 sheet we have found, shown in Figure 3.10(a), occurs at $\eta = 1/4$ and is obtained by doping Mg on an F(1/4) boron sheet. This particular MgB_2 sheet is 0.72 eV/MgB_2 more stable than the bulk-derived one (η=1/3), which is a significant energy difference. We believe that this sheet is a better precursor for MgB_2 nanotubes.

During the above search process, we found the following rules-of-thumb to hold when generating stable MgB_2 sheets. While we are not able to present a proof, we believe they should be generally applicable to other stoichiometries. In order to make the lowest energy structure, one should: (a) to whatever extent possible, put Mg on the hexagon sites (above or below the boron sheet), (b) fill both sites above and below the hexagon if needed, (c) put any remaining Mg in the triangular regions. Only a very small number of our most stable MgB_2 sheets do not obey these rules, e.g., the sheet in Figure 3.10(d).

To exemplify these rules, for the fixed boron sublattice of sheet F(1/4) we constructed

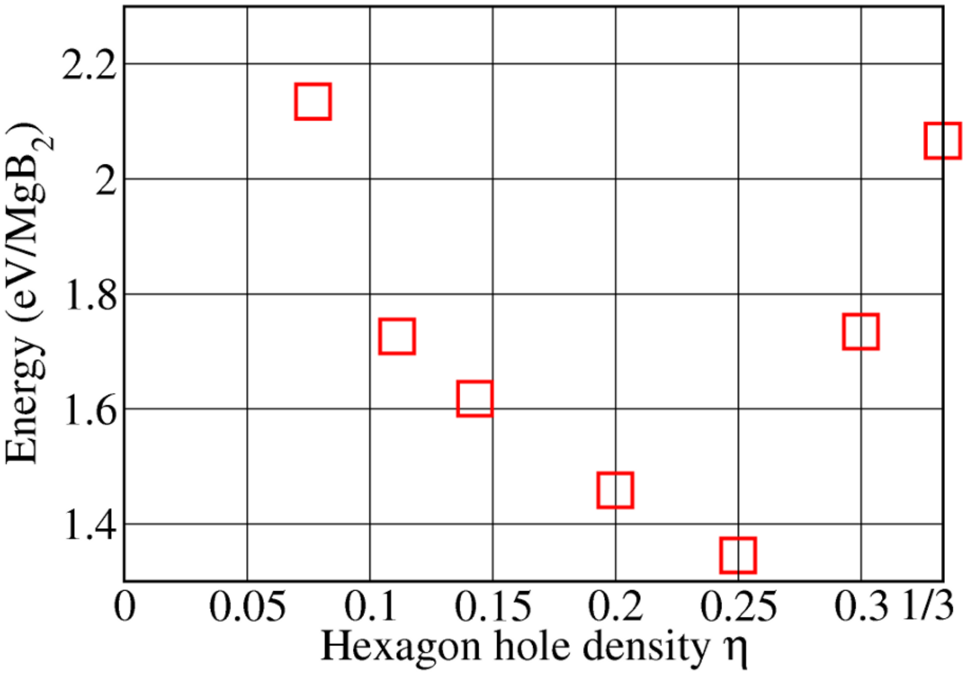

Figure 3.11: Red squares show the energies (measured relative to bulk MgB_2) per formula unit of the most stable MgB_2 sheets at each η versus η. The optimal MgB_2 sheet structure occurs at $\eta = 1/4$ (whose image is shown in Figure 3.10(a)). The point at $\eta = 1/3$ corresponds to the bulk-derived sheet structure.

a few variants of the optimal MgB_2 sheet (Figure 3.10(a)) where only the distribution of Mg atoms among hexagon sites was varied. These MgB_2 sheets, which are shown in Figure 3.12, are all less stable than the optimal one but only by at most 20 meV/MgB_2. Thus while a search over possible Mg arrangements is needed to find the true ground state, this part of the search does not contribute greatly to the total energy as long as all Mg atoms occupy hexagon sites. In summary, the combination of the optimal η from Eq. (3.10) and the above rules for the best Mg placement greatly narrow down the search space for optimal metal boride nanostructures.

3.1.4 Surface buckling

Unlike graphene, not all 2D atomically thin boron sheets are completely flat. Instead, for many boron sheets, the atoms prefer to move out of the nominal sheet plane and form corrugated surfaces. This phenomenon is generally named 'buckling' in the literature. Buckling is quite common in boron nanostructures. All quasi-planar boron clusters studied

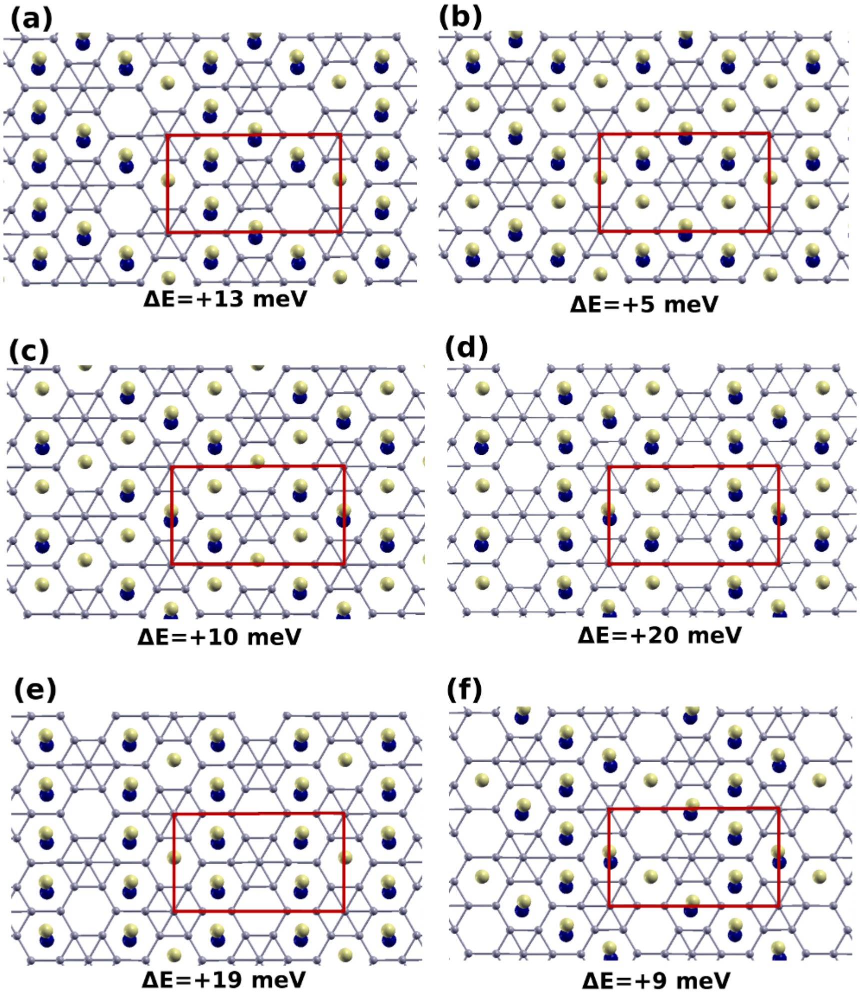

Figure 3.12: MgB_2 sheet structures derived from the same F(1/4) boron sheet sublattice but with different Mg distributions from the optimal MgB_2 sheet shown in Figure 3.10(a). These sheets are all less stable than the optimal structure. The energy differences, in meV per formula unit, are shown below each structure. We display topviews that are rotated slightly around the horizontal (x) axis. Small gray balls are B, large light yellow balls are Mg lying above the boron plane, and large dark blue balls are Mg lying below the boron plane. Red solid lines show the primitive cells.

in both theory and experiments have buckled surfaces [16, 17, 18, 19, 9, 20, 21, 22, 23, 24]. For 2D boron sheets made of triangles and hexagons, the ground-state configurations may be either buckled or flat depending on the hexagon-to-triangle ratio (see below). In addition, small-diameter nanotubes have buckled surfaces [12, 13] although their precursor, sheet A(1/9), prefers to stay flat. Finally, buckling is closely related to the formation of

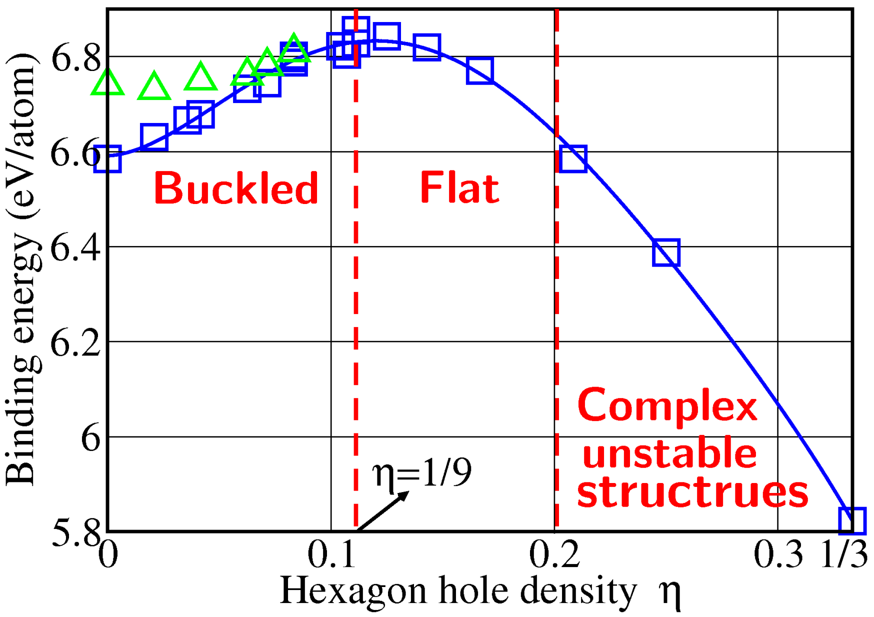

Figure 3.13: Binding energy E_b (from LDA) versus hexagon hole density η for single-layered boron sheets with evenly distributed hexagons. The blue '□' are the binding energies of flat sheets, and the solid blue curve is a polynomial fit. The green '△' are the binding energies for buckled sheets (that are stabilized by buckling). Maximal E_b occurs for sheet α ($\eta = 1/9$) or A(1/9), which is the most stable structure. The vertical dashed red line at $\eta = 1/9$ indicates the separation point of naturally flat and buckled single-layered boron sheets.

interlayer bonds in double-layered boron sheets as we discuss in Sec. 3.2. For these reasons, investigating the buckling of boron sheets is helpful for understanding the basic properties of boron nanostructures.

We have performed a large number of calculations on 2D single-layered boron sheets where we start with flat configurations, create perturbations in the form of buckling of the surfaces, and allow for full relaxations. We summarize the key results here. First, for sheets with $\eta > 1/5$, which in their flat form are already highly unstable compared to the optimal sheets with $\eta \approx 1/9$ (see Figure 3.13), we find large vertical buckling amplitudes along the out-of-plane (z) direction and complex resulting final structures. However, even after relaxation, these structures are still quite unstable energetically, so we ignore them in what follows. Second, for sheets with $\eta < 1/5$, some sheets buckle vertically along the out-of-plane z direction while some do not and remain flat. More precisely, among boron sheets with evenly distributed hexagons and for $0 < \eta < 1/5$, we find that whether the ground state is buckled or flat depends only on the hexagon hole density η. The buckling behavior is asymmetric with respect to η: sheets with $\eta < 1/9$ prefer to buckle while those with $\eta \geq 1/9$ remain flat. The energetic changes due to buckling are shown in Figure 3.13. The increase in stability due to buckling is at most 0.16 eV/atom for the triangular T(0) sheet and decreases to zero as $\eta = 1/9$ is approached. The separation point occurs at $\eta = 1/9$, which coincides with the optimal sheet structure A(1/9). Therefore, when we account for the buckling effect, the left side ($\eta < 1/9$) of the binding energy curve becomes somewhat flatter as shown in Figure 3.13.

It has been known that the triangular sheet T(0) [see Figure 3.14(a)] can buckle in many different ways and get trapped in various local minima, but the two-atom-cell buckling pattern leads to the most stable structure of the buckled triangular sheet [36, 38, 37, 39, 40, 6]. However, for other sheets with $0 < \eta < 1/9$, we find that they generally prefer to become buckled in some specific manner. These buckling patterns are determined by the eigenvectors of the unstable phonon modes with imaginary frequencies of the corresponding flat sheets. For instance, the $\eta = 1/12$ sheet Z(1/12) shown in Figure 3.14(b) has two different buckling patterns determined by its two imaginary phonon modes. One of these patterns is shown in Figure 3.14(b) as indicated by coloring. The stabilization of the buckled Z(1/12) sheet is actually quite small and is only 0.01 eV/atom.

On the other hand, the optimal A(1/9) and other sheets with $1/9 < \eta < 1/5$ [e.g., sheets B(1/7) and C(1/6) in Figure 3.14] have only stable real phonon frequencies and thus stay flat. In order to see whether these sheets prefer to buckle when compressed, which is typical when they are bent or curved to form part of a nanotube, we studied these flat sheets under isotropic compression in the x-y plane and checked to see if any phonon mode became unstable. Not surprisingly, we found that under sufficient compression, every sheet will develop one or more imaginary phonon frequencies and will buckle. For example, sheet B(1/7) has an imaginary phonon frequency when compressed by 5%. The buckling patterns of compressed sheets A(1/9), B(1/7) and E(1/6) are shown in Figure 3.14 by coloring.

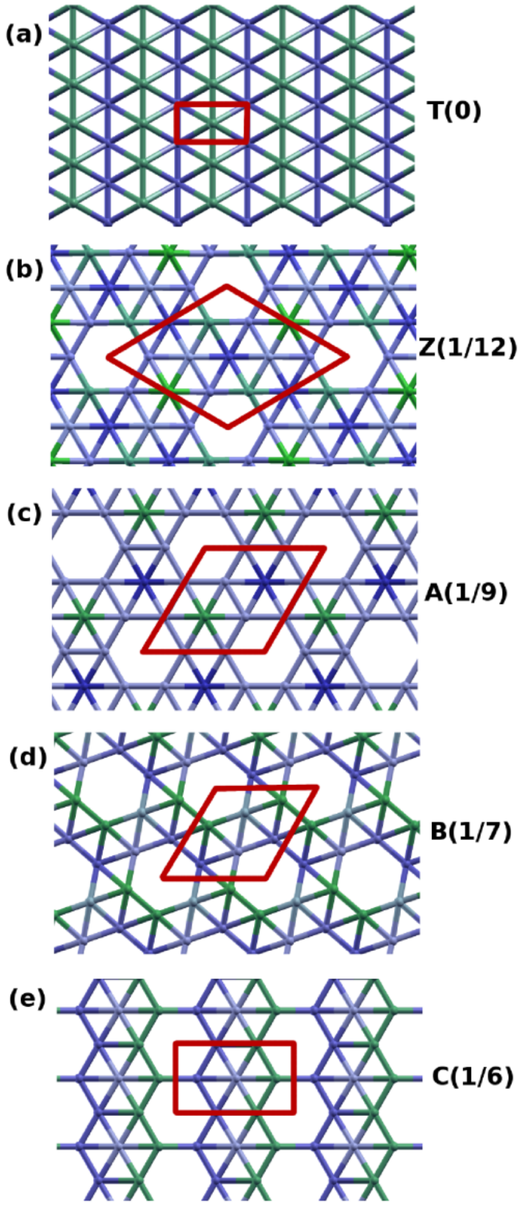

Figure 3.14: Structures of five boron sheets: (a) T(0), (b) Z(1/12), (c) A(1/9), (d) B(1/7) and (e) C(1/6). The red solid lines show the unit cells. The preferred buckling patterns are indicated by coloring: z coordinates increase as color changes from green to gray to purple so that green means negative z coordinates, gray shows z coordinates close to 0, and blue means positive z. Since the sheets A(1/9), B(1/7) and C(1/6) do not buckle at equilibrium, the buckling patterns shown here are obtained by applying an isotropic compressive strain of 5% in the x-y plane.

Origin of buckling: σ-π mixing?

What is the origin of this common tendency for 2D boron structures to buckle? An obvious first guess is that perhaps the buckling is driven by mixing of in-plane σ and out-of-plane π states. For a flat 2D structure, all electronic states have either even or odd parity with respect to the reflection in the plane which correspond to in-plane (σ) and out-of-plane (π) states, respectively. Once a 2D structure becomes buckled, the original reflection symmetry is lost, and in a perturbative picture the resulting electronic states are mixtures of the original in-plane and out-of-plane states. If important mixing happens around the Fermi level, bonding combinations of σ and π states could be pushed below the Fermi level, leading to increased stability. (This picture is analogous in many ways to the stabilization resulting from a Peierls distortion.) In other words, in this scenario the band energy would decrease sufficiently to overcome the increase in elastic energy and thus make buckling preferable.

Following this idea, the fact that sheet A(1/9) is flat can be rationalized via a simple argument: no mixing between in-plane and out-of-plane states exists around the Fermi energy because the Fermi level lies in an energy gap for the in-plane states [6]. Thus there is no energy gain to compensate the increase of elastic energy. However, this explanation is already problematic because it does not provide a reason for the clear asymmetry in buckling behavior around $\eta = 1/9$. All sheets with η above and below 1/9 have in-plane and out-of-plane states coexisting at the Fermi energies, so that we would have expected that sheets on both sides of $\eta = 1/9$ would buckle, in disagreement with the *ab initio* results.

A more careful examination shows that in fact the entire picture is quantitatively incorrect. (A better explanation is provided in the next section.) To quantitatively examine whether the behavior of the band energy can explain the buckling, we divide the total energy E_{tot} into two parts, the band energy E_{band} and the remainder as a "repulsive" term E_{rep}:

$$E_{tot} = E_{band} + E_{rep}, \tag{3.11}$$

where

$$E_{band} = \int_{-\infty}^{E_F} D(E)\, E\, dE, \tag{3.12}$$

where $D(E)$ is the electronic density-of-states and E_F is the Fermi energy, and we compute this energy directly from the first principles results. The repulsive energy, $E_{rep} = E_{tot} - E_{band}$, is defined and computed exactly as this difference from *ab initio* calculations. (To make E_{rep} always positive, we have defined the repulsive energy of an isolated boron atom to be zero, then E_{rep} and E_{tot} for all boron sheets are scaled accordingly.) As expected from simple tight-binding theory, E_{rep} is generically positive and in a tight-binding picture would be given by a sum over repulsive pair interactions [86]:

$$E_{rep} \approx \sum_{R_i, R_j} V(|R_i - R_j|), \tag{3.13}$$

where $V(|R_i - R_j|)$ is a short-range repulsive interaction between two nuclei at R_i and R_j. (However, we emphasize that we do not use this approximate form but instead compute E_{tot}, E_{band}, and E_{rep} directly from the first principles results.)

When computing the band energy, it is clear that any shifts in E_F will modify the computed value. It is well known that standard periodic supercell calculations have an arbitrary, and difficult to compute, energy shift stemming from the long-range Coulomb interaction. Therefore, to get reliable E_{band} energies, we must measure E_F with respect to the vacuum level. This is accomplished by performing a series of calculations with differing supercell sizes L along the z direction; the behavior of E_F versus L for large L is essentially linear in L^{-1}. In this way, we can extrapolate to $L = \infty$ and find absolute E_F and thus E_{band} energies.

In the σ-π mixing picture described above, the band energy E_{band} should decrease upon buckling as hybridization around E_F pushes states below E_F. In Table 3.2, we show the calculated band energies and repulsive energies of five sheets spanning a range of η values when they are flat and slightly buckled (according to their preferred buckling patterns), respectively. We can see that all sheets except sheet C(1/6) have their band energies increase and repulsive energies decrease due to buckling, while sheet C(1/6), which naturally does not prefer to buckle, has the opposite behavior. These results are clearly

Table 3.2: Band energies (E_{band}), repulsive energies (E_{rep}) and total energies (E_{tot}) of five boron sheets T(0), Z(1/12), A(1/9), B(1/7), and C(1/6), respectively, for flat and buckled cases (from LDA). For the flat sheets, the energies are in eV/atom. For the buckled sheets, the percentage change from the flat energy is reported to highlight the direction of the energy change ('+' for increase and '-' for decrease'). The buckling height is fixed at 0.16 Å in all cases.

	Flat			Buckled		
Sheet	E_{band}	E_{rep}	E_{tot}	δE_{band}	δE_{rep}	δE_{tot}
T(0)	-37.82	8.50	-29.32	+0.89	-4.31	-0.10
Z(1/12)	-37.21	7.68	-29.54	+1.19	-5.81	-0.01
A(1/9)	-36.21	6.61	-29.59	+0.59	-3.18	+0.01
B(1/7)	-35.07	5.52	-29.55	+0.92	-5.00	+0.02
C(1/6)	-33.89	4.38	-29.51	-0.02	+0.68	+0.01

opposite to the expectations from the σ-π mixing picture. In other words, splitting the total energy into band and repulsive energies has not helped us understand the origin of the buckling.

Kinetic energy: The driving force for buckling

As the chemical bonding picture based on σ-π hybridization fails to explain the buckling, we turn to a different physical picture. We instead view these 2D metallic boron sheets as a realization of (a possibly non-standard) 2D electron gas. Namely, we should consider breaking up the total energy into terms that are most natural for an electron gas analysis: the kinetic energy, the (classical) electrostatic energy of interaction among all charges, and the exchange-correlation energy due to the quantum behavior of the electrons. Interestingly, even though 2D boron sheets show significant covalent bonding character, this picture turns out to work well: the kinetic term is dominant, as expected for a medium-to-high density electron gas, and its variations largely dictate the buckling. Therefore, we write the total energy E_{tot} as

$$E_{tot} = E_{kin} + E_{xc} + E_{es}, \tag{3.14}$$

where E_{kin} is the total electronic Kohn-Sham kinetic energy, E_{xc} is the exchange-correlation energy (here evaluated within the LDA or GGA), and E_{es} is the sum of all remaining energies. E_{es} physically represents the sum of all classical electrostatic interactions among

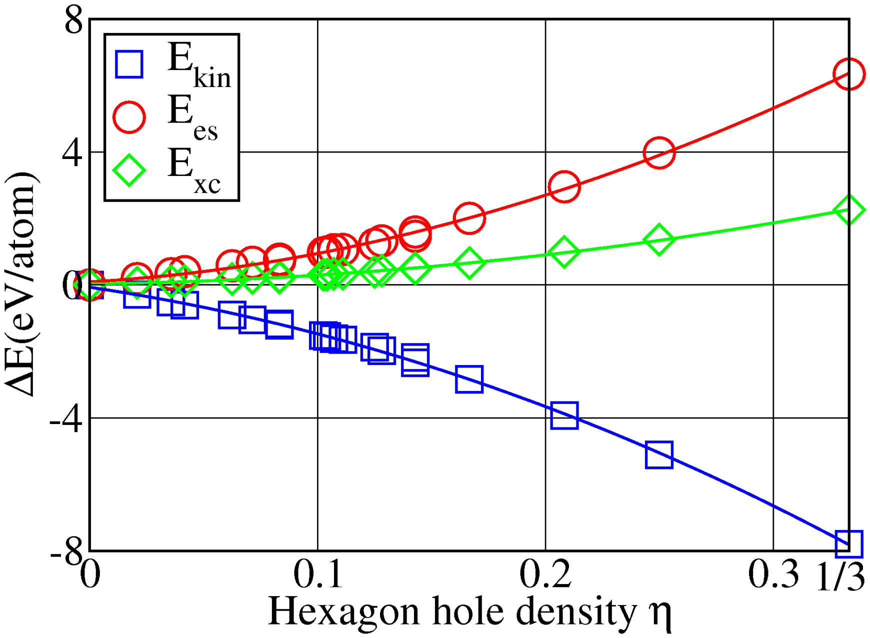

Figure 3.15: Kinetic (E_{kin}), electrostatic (E_{es}) and exchange-correlation (E_{xc}) energies versus η for flat 2D boron sheets. Energies are in the units of eV/atom. All three energies are plotted with respect to their respective values at $\eta = 0$ (the zero of energy). The squares, circles and diamonds are the calculated results, while the solid curves are guides to the eye.

charges: electron-electron, electron-ion, and ion-ion. (The nonlocal electron-ion interaction from the pseudopotential is thus included in E_{es} as this term is designed to reproduce the interactions of the valence electrons with the nucleus in an all-electron framework.)

Separately, it is helpful to have a measure of the average electron density in the system in order to correlate with usual notions of electron gas behavior. Unfortunately, there is no obvious unique *a priori* way to define an average electron density for an arbitrary material system with a spatially varying electron density. Therefore, we resort to a very simple definition which uses the density itself as the weighing function:

$$\bar{n} = \frac{\int (n(r))^2 dr}{\int n(r) dr}. \tag{3.15}$$

This simple measure averages the density in the spatial regions where the electrons spend the most time. Therefore, it is slightly biased to large values by the relatively large values of the electron density close to each boron atom and does not only measure the electron

Table 3.3: Kinetic energy (E_{kin}), electrostatic energy (E_{es}), exchange-correlation energy (E_{xc}), total energy (E_{tot}), and the average electron density $\bar{n}$ of five boron sheets T(0), Z(1/12), A(1/9), B(1/7), and C(1/6), respectively, for flat, artificially buckled and fully relaxed cases (from LDA). For flat sheets, energies are in eV/atom and $\bar{n}$ is in units of 10^{-2}e/Bohr^3. For buckled and fully relaxed sheets, we show percentage changes of the energies and $\bar{n}$ compared to the flat values ('+' for increase, '-' for decrease). The buckling height is fixed at 0.16 Å in all artificially buckled sheets.

Flat					
Sheet	E_{kin}	E_{es}	E_{xc}	E_{tot}	$\bar{n}$
T(0)	57.34	-104.22	-30.12	-77.00	8.85
Z(1/12)	56.17	-103.49	-29.90	-77.22	8.74
A(1/9)	55.79	-103.25	-29.81	-77.27	8.71
B(1/7)	55.16	-102.76	-29.63	-77.23	8.59
C(1/6)	54.50	-102.22	-29.47	-77.19	8.47

Buckled					
Sheet	δE_{kin}	δE_{es}	δE_{xc}	δE_{tot}	$\delta\bar{n}$
T(0)	-1.62	+0.65	+0.74	-0.10	-2.49
Z(1/12)	-0.80	+0.33	+0.35	-0.01	-1.14
A(1/9)	-0.27	+0.11	+0.12	+0.01	-0.46
B(1/7)	-1.34	+0.57	+0.69	+0.02	-2.33
C(1/6)	-0.78	+0.31	+0.43	+0.01	-1.42

Fully relaxed					
Sheet	δE_{kin}	δE_{es}	δE_{xc}	δE_{tot}	$\delta\bar{n}$
T(0)	-4.10	+1.74	+1.31	-0.20	-3.73
Z(1/12)	-0.44	+0.19	+0.13	-0.01	-0.42
A(1/9)	-	-	-	-	-
B(1/7)	-	-	-	-	-
C(1/6)	-	-	-	-	-

density of the delocalized mobile electrons. However, for our purposes, it is a reasonable definition in which it shows monotonic behavior versus η (see below).

We first investigate how E_{kin}, E_{xc} and E_{es} behave for flat sheets. Figure 3.15 shows E_{kin}, E_{xc}, E_{es} versus η for a large set of flat 2D boron sheets. We can see that E_{kin}, E_{xc} and E_{es} all change smoothly and monotonically with η, or equivalently with 1-η. Because the nearest-neighbor distances in the different boron sheets are almost identical [6], for these flat sheets 1-η also changes monotonically with the average electron density $\bar{n}$ as shown in Table 3.3. Hence, E_{kin}, E_{xc} and E_{es} all change monotonically with $\bar{n}$ as one would expect for an electron gas.

We now turn to the buckling effect for these sheets. Table 3.3 shows how E_{kin}, E_{xc} and

E_{es} change when each sheet buckles. For the five sheets investigated, E_{kin} always decreases and E_{xc} and E_{es} always increase due to buckling. For those sheets that prefer to buckle, sheets T(0) and Z(1/12) in Table 3.3, the decrease in E_{kin} dominates over the other two energy increases. Therefore, the buckling is driven by kinetic energy lowering, and that kinetic energy lowering wins over the increase of $E_{es} + E_{xc}$ for $\eta < 1/9$. In addition, we see that $\bar{n}$ is decreased by buckling, and lowering of density is consistent with lowering of kinetic energy (a smaller Fermi momentum or Fermi energy) and higher E_{es} and E_{xc} (larger average charge separation). Intuitively, if we view the sheet as a continuous film, then surface buckling can be expected to increase the surface area which then rationalizes the decrease in electron density: the same number of electrons are spread over a sheet with increased surface area due to the corrugation. However, since there is no rigorous definition of surface area at the discrete atomic scale, this picture serves primarily as an aide to understanding and visualization.

What we have found is that buckling reduces the electron density, which in turn lowers the kinetic energy and thus drives the buckling. The kinetic energy is larger and more dominant for higher electron densities (smaller η) so that those sheets will have a stronger tendency to buckle. Most importantly, this picture naturally explains the asymmetry in the buckling behavior about $\eta = 1/9$. Since buckling reduces $\bar{n}$, and $\bar{n}$ and $1 - \eta$ are in monotonic relation, decreasing $\bar{n}$ effectively increases η. Because the binding energy versus η (see Figure 3.2) has a maximum at $\eta = 1/9$, sheets with $\eta < 1/9$ can increase their stability by buckling, while those with $\eta > 1/9$ would decrease their stability if they buckled.

The above results clearly show that it is the lowering of the kinetic energy that drives the initial stages of buckling in boron sheets. We may wonder if this finding is more general. After all, for the small buckling amplitudes used above, it can be argued that the geometry and chemical bonding modes barely change, but in the final fully buckled structure this may not be the case. For example, the fully buckled triangular sheet has strong two-center-type bonding and the bond length along that direction are significantly reduced [36, 37], pointing to basic changes in bonding topology and possibly a decrease in surface area in the intuitive picture above. However, our results show that even in fully relaxed buckled sheets, the kinetic energy is still the energetic driving force: Table 3.3 shows that for the triangular T(0) and the Z(1/12) sheets, the kinetic energy and average electron density are always lowered compared to their flat counterparts — and this holds for other sheets we have investigated. Furthermore, as we will show in Sec. 3.3.2, the same kinetic energy reduction holds for buckled single-walled boron nanotubes as well. Therefore, we believe that kinetic energy reduction is most probably the key driving force that drives the buckling of boron sheets and nanotubes.

3.2 Double-layered boron sheets

For boron nanostructures, strong interlayer bonds can be formed between two planar or quasi-planar parts stacking perpendicular to the nominal structure plane [29, 41]. Due to these interlayer bonds, multi-layered boron sheets can be more energetically favorable than the most stable single-layered boron sheet A(1/9) (see below). When creating boron nanostructures such as nanotubes by folding, wrapping, or cutting boron sheets, it is possible that multi-layered boron sheets will be the parent structures under certain growth conditions. Therefore, studying multi-layered boron sheets, where the simplest cases are those of double-layered sheets, can be relevant to understanding experimentally grown structures as well as to helping us understand the general properties for boron nanostructures.

Below, we find that the knowledge we have gained concerning the buckling of single-layered boron sheets is invaluable in clarifying and rationalizing the tendencies for buckling and formation of interlayer bonds in double-layered systems. In this work, we limit ourselves to double-layered sheets, which already create a large class of systems to study and analyze. Our primary aim is to obtain a basic understanding of the buckling and bonding behavior of boron sheets when they are in close proximity. An extension of these results to multi-layered structures is beyond the scope of the present work.

In this work, the naming system for boron sheets has been using a letter followed by the η value to designate a single-layered sheet. For double-layered boron sheets discussed mainly in this section, we name a sheet using the word 'double' followed by the name of the corresponding precursor single-layered sheet. For instance, double-B(1/7) refers to a double-layered boron sheet made from stacking two identical B(1/7) sheets [see

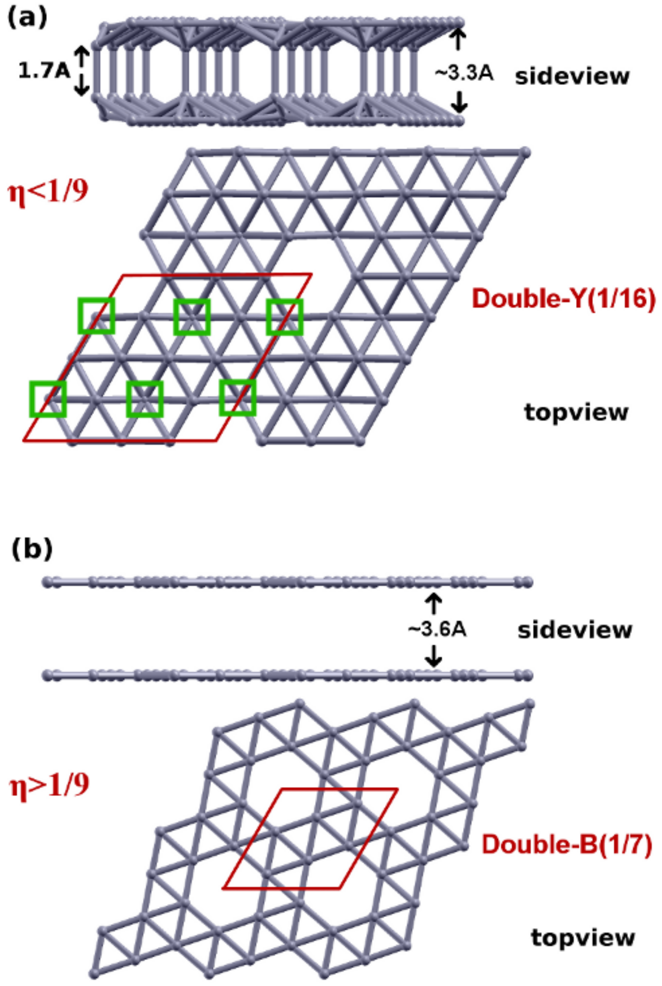

Figure 3.16: Illustration of structures of double-layered boron sheets (top and sideviews) for both (a) the $\eta < 1/9$ double-Y(1/16) sheet and (b) the $\eta > 1/9$ double B(1/7) sheet. The red solid lines in the top views show the 2D primitive unit cells. The green squares in the top view of (a) mark the atoms that form interlayer bonds in a primitive cell.

Figure 3.16(b)].

To study double-layered boron sheets, we proceed in the following manner: we take two (primitive cell) copies of a particular 2D boron sheet and place the two copies some initial distance apart (≈ 3 Å). We then create some random perturbations of all atomic positions and perform a full relaxation. After following this procedure for a large number of such double-layered structures, we discover that a pair of sheets with $\eta < 1/9$ tends to make strong interlayer bonds. On the other hand, two sheets with $\eta >= 1/9$ do not: the

Table 3.4: Energetic and geometric properties of five double-layered boron sheets constructed from pairs of T(0), Y(1/16), Z(1/12), A(1/9) and B(1/7) sheets (from LDA). The first three double-layer sheets form interlayer bonds while the other two do not. E_{bond} (in eV/atom) is the reduction in energy (i.e. binding energy) of the double-layer sheet compared to the two separate constituent single-layer sheets. d_{bond} (in Å) is the interlayer bond length. N_{bond} is the number of interlayer bonds per atom formed between the two sheets. ΔE_{α} (in eV/atom) is the energy of the double-layer system compared to the optimal single-layered A(1/9) (α) sheet. d_{inter} (in Å) is the distance between two nominal sheet planes defined by boron atoms not making interlayer bonds.

Sheets	η	E_{bond}	d_{bond}	N_{bond}	ΔE_{α}	d_{inter}
T(0)	0	-0.30	1.70	1/8	-0.03	3.37
Y(1/16)	1/16	-0.24	1.70	4/30	-0.12	3.33
Z(1/12)	1/12	-0.19	1.69	3/22	-0.135	3.23
A(1/9)	1/9	-0.02	-	0	-0.02	3.49
B(1/7)	1/7	-0.03	-	0	+0.01	3.60

two single-layered sheets stay quite flat, are weakly bound, and stay apart at a relatively large distance of typically 3.5 to 3.6 Å. (This separation likely correlates with weak van der Waals interactions which are not correctly captured by LDA or GGA calculations; however, our main point is that the interactions are quite weak and no interlayer bonds are formed, which we believe is a robust result even if van der Waals interactions were included correctly.) Two typical examples are shown in Figure 3.16. When interlayer bonds form, the interlayer bond length is about 1.7 Å which is quite typical of the lengths in 2D boron structures.

The above behavior is simply explained from the buckling behavior of single-layered boron sheets: a pair of sheets will form interlayer bonds only when each sheet alone prefers to buckle in the first place (i.e., both sheets have $\eta < 1/9$). The main requirement is to properly align the sheets so that the geometry allows the buckling atoms to make interlayer bonds with each other. As a simple further test of the relation between buckling and formation of interlayer bonds, we know that the optimally stable A(1/9) sheet does not normally buckle but can be forced to buckle when under compression. Therefore, we put 1% of isotropic compression in the xy plane on a pair of A(1/9) sheets in close proximity and find that the sheets buckle, that they form interlayer bonds of about 1.7 Å in length, and that the bonding pattern is the one dictated by the buckling pattern of the single-layered sheet under compression (see Figure 3.14).

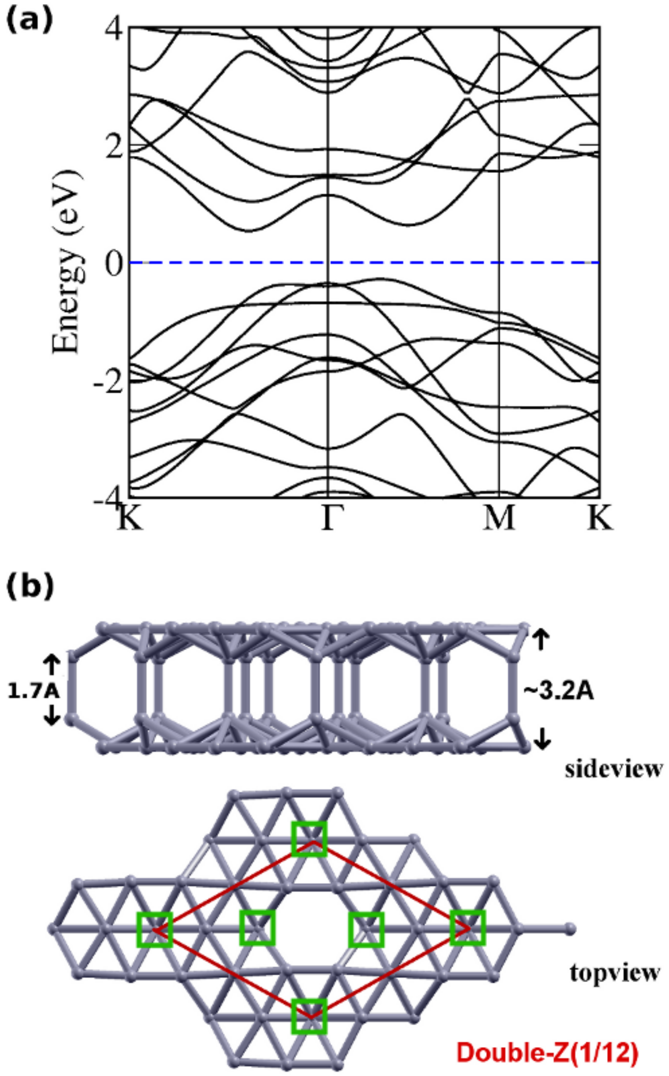

Figure 3.17: (a) Band structure of the double-Z(1/12) sheet: the Fermi level is set to zero, which is illustrated by the blue dashed line. (b) Structure of the double-Z(1/12) sheet (sideview & topview). Red solid lines show the unit cell and green squares mark the atoms making interlayer bonds in one unit cell.

Table 3.4 shows a subset of our *ab initio* results for double-layered boron sheets built from pairs of T(0), Y(1/16), Z(1/12), A(1/9) and B(1/7) sheets. The first three double-layered sheets, made from T(0), Y(1/16) and Z(1/12), form interlayer bonds with the bond lengths close to 1.7 Å and thus strongly stabilize (i.e. bind) the double-layer system. The energy reduction due to the interlayer bonding, E_{bond} in the Table, is significant and gets larger for smaller η since more interlayer bonds form. As a result, we find that the most stable double-layered sheet in our library occurs at $\eta = 1/12$ for the double-Z(1/12) case. This double-layered system is 0.135 eV/atom more stable than the optimal single-layered A(1/9) sheet and is thus the most stable sheet structure we have found to date. Figure 3.17 shows the atomic structure and the electronic band structure of the double-Z(1/12) sheet. In contrast to the single-layered sheets which are all metallic, the double-Z(1/12) sheet is semiconducting with a reasonably large LDA band gap of 0.8 eV. Speaking figuratively, the formation of the interlayer bonds has created bonding and anti-bonding combinations of the states that used to be at the Fermi level, pushed them above and below E_F, and thus created a semiconducting system. Due to this stability, boron nanotubes could in fact originate from this double-Z(1/12) sheet. However, depending on growth conditions during experiment, it might be possible that either single or double layered tubes will be preferred, thus making the nanotubes either metallic or semiconducting. Some of the aspects addressable from first principles are discussed in the following sections.

3.3 Single-walled boron nanotubes

We now turn to single-walled nanotubes made from single-layered 2D boron sheets, and we investigate primarily their curvature energies and surface buckling. We name a boron nanotube (single-walled or double-walled) following the established standard for carbon nanotubes: an (n, m) nanotube has its chiral vector $Ch = n \times \boldsymbol{a}_1 + m \times \boldsymbol{a}_2$, where $\boldsymbol{a}_1$ and $\boldsymbol{a}_2$ are the two primitive lattice vectors of the corresponding sheet structure [87]. We take the extended direction of the nanotube to be along the z direction. The curvature energy of a nanotube, E_{curv}, is defined as

$$E_{curv} = E_{tube} - E_{sheet}, \tag{3.16}$$

where E_{tube} is the energy per atom of that nanotube, and E_{sheet} is the energy per atom of the corresponding sheet structure. Therefore, E_{curv} is the energy cost of rolling up the sheet into a tubular structure.

A priori, the number of possible structures for single-walled nanotubes is enormous. However, we know that the A(1/9) sheet is the most stable 2D single-layered boron sheet, so that for large diameter nanotubes with vanishing curvature, we are assured that the surface structure of the most stable single-walled nanotubes will be that of the A(1/9) structure. Based on this fact, we simply constrain all the single-walled nanotubes we study to be built from the A(1/9) structure regardless of diameter. In principle, one can investigate the question of whether single-walled nanotubes made from sheets other than A(1/9) might be stabilized due to curvature effects for small diameters, but this question is beyond the scope of our present work.

The optimal boron sheet A(1/9) has a energy gap for the in-plane σ states and a finite density-of-states for the out-of-plane π manifold [6, 12]. Thus, the conductivity of the A(1/9) sheet comes only from out-of-plane π states. Therefore, large-diameter single-walled nanotubes built from A(1/9) will always be metallic since the electronic structures are determined by the zone-folding technique [87, 88]. However, it has been found that small-diameter boron nanotubes built from the A(1/9) sheet are semiconducting, with energy gaps around a few tenth of eVs, due to curvature and surface buckling [12, 13]. Below, we investigate in detail these curvature effects on the energetics and electronic structure of the single-walled nanotubes.

3.3.1 Curvature

Figure 3.18 shows how the curvature energy E_{curv} changes with tube diameter D for a wide range of such achiral single-walled nanotubes [i.e., (n,0) and (n,n) nanotubes] created from wrapping the A(1/9) sheet. The data from these two different classes of nanotubes lie almost exactly on the same smooth curve, suggesting that the curvature energy of this type of single-walled nanotubes does not depend strongly on chirality. Namely, E_{curv} is determined by the nanotube diameter D, a result that is consistent with previous work on this problem [12, 13].

As is the case for carbon nanotubes [89, 90], we expect from elastic theory that E_{curv} should have the following simple dependence on D for large D:

$$E_{curv} = \frac{C}{D^2}, \tag{3.17}$$

where C is a constant. By fitting all the data in Figure 3.18, we obtain C=4.28 eVÅ^2/atom,

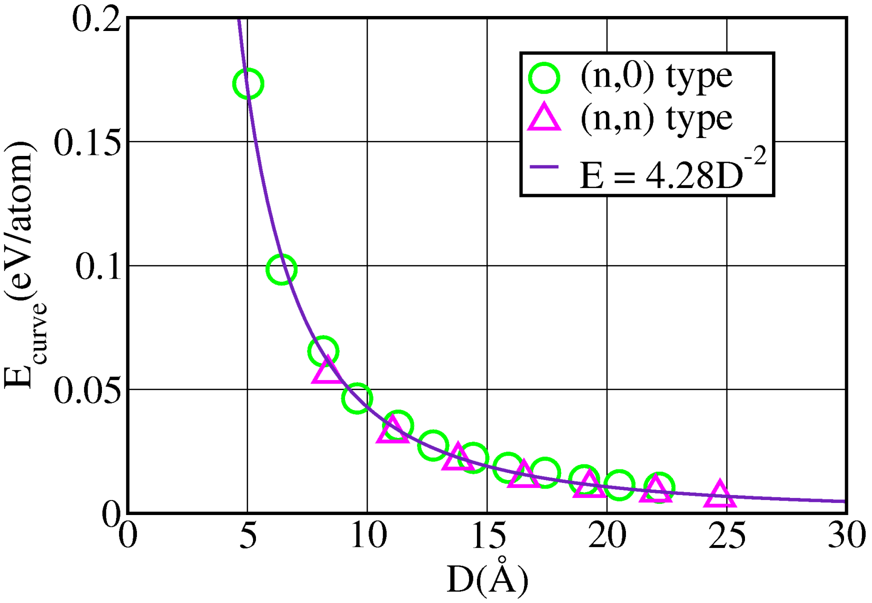

Figure 3.18: Curvature energies E_{curv} in eV/atom of single-walled boron nanotubes made of the A(1/9) sheet versus diameter D in Å(from LDA). Green '◯' are for (n,0) nanotubes with n ranging from 3 to 14. Magenta '△' are for (n,n) nanotubes with n ranging from 3 to 9. The indigo solid line is a single-parameter $1/D^2$ fit to the combined data set.

slightly larger than the value C=3.64 eVÅ^2/atom in previous work [13], which we believe is due to the fact that the LDA we use usually results in stronger bonding than GGA-PBE. For comparison, carbon nanotubes have C=8.56 eVÅ^2/atom [89, 90]. Therefore, for a given diameter, it is easier to curve the A(1/9) sheet than to curve graphene to create single-walled nanotubes.

3.3.2 Surface buckling

Since sheet A(1/9) is metallic with a large density of states at its Fermi energy coming from the out-of-plane π manifold, simple zone-folding leads us to expect that all boron nanotubes made of sheet A(1/9) are metallic. However, boron nanotubes with small radii are actually semiconducting due to the fact that tube surfaces become buckled under the large curvature necessitated by the small diameter. This buckling has been attributed to rehybridization in the σ-π manifold [12, 13].

As we explained in Sec. 3.1.4, sheet A(1/9) prefers to stay flat when it is stress free but will buckle under compression. When it buckles, the two boron atoms in each unit

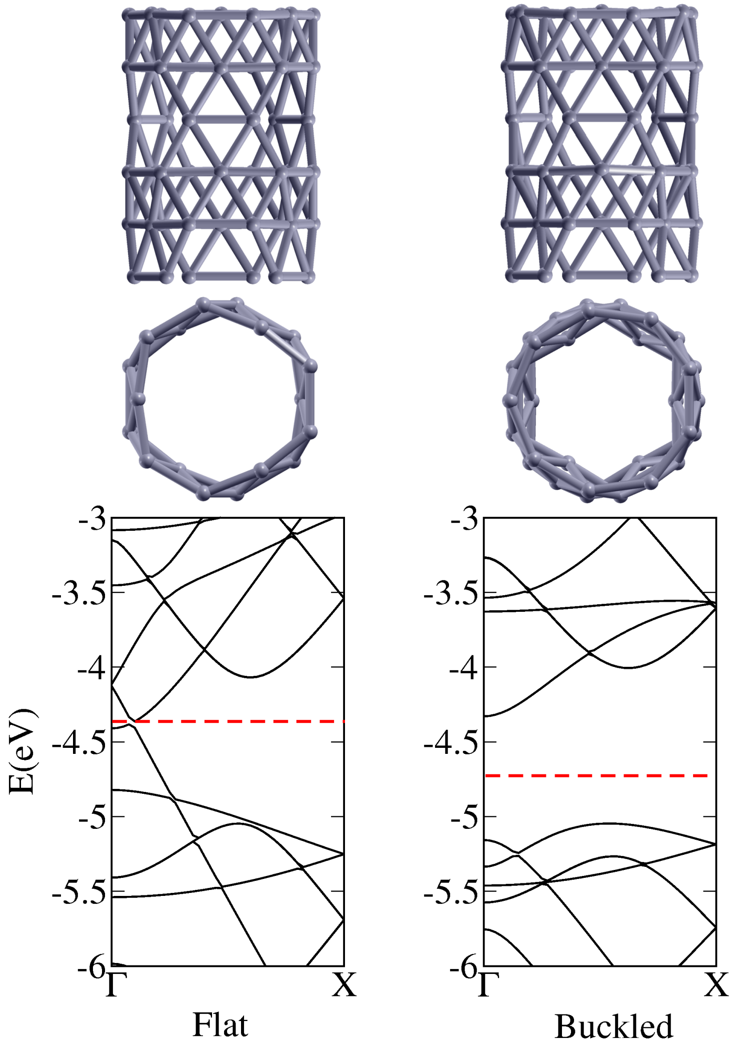

Figure 3.19: Structures (sideview and topview) and bandstructures of the single-walled boron nanotube (3,0) with flat (left) and buckled (right) surfaces (from LDA). Red dashed lines show the Fermi energies.

cell that are in the triangular regions will move out of the sheet plane, with one going up and the other going down (see Figure 3.14). We find that when the A(1/9) sheet is curved to form nanotubes, the same buckling pattern is observed: the two atoms in the triangular regions become inequivalent, with one moving radially inwards and the other moving radially outwards. Due to this surface buckling, small-diameter single-walled boron nanotubes become semiconducting. Figure 3.19 shows the single-walled nanotube (3,0) as an example. This buckling and semiconducting behavior is only relevant for small diameter

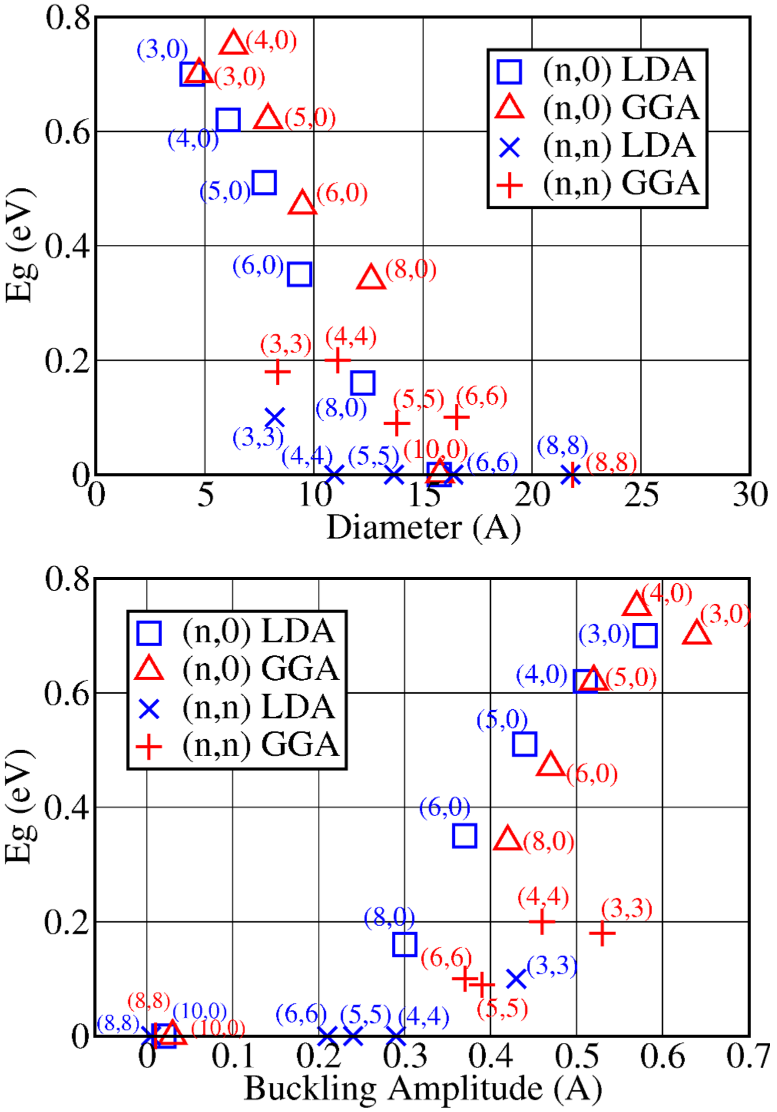

Figure 3.20: Band gap E_g (in eV) versus tube diameter (top, in Å) and buckling amount (bottom, in Å) for (n,0)- and (n,n)-type A(1/9)-derived single-walled boron nanotubes calculated with both LDA and GGA.

nanotubes: as Figure 3.20 shows, the band gap vanishes for diameters larger than ∼ 20 Å [12, 13]. We also see that for a fixed diameter, the band gaps for (n,0) and (n,n) nanotubes can be significantly different.

As our results in Figure 3.20 show, the LDA and GGA result in systematically different band gaps for these single-walled boron nanotubes with results that differ by ∼ 0.1-0.2 eV

Table 3.5: Energetic, structural, and electronic data for $(n,0)$- and (n,n)-type single-walled boron nanotubes derived from sheet A(1/9) based on LDA and GGA calculations. The table shows total energy differences δE (in meV/atom) between flat- and buckled- surfaced cases of a nanotube, (average) nanotube diameter D (in Å), buckling amplitude A_{buckle} (in Å), and the nanotube band gap E_{gap} (in eV).

	LDA				GGA			
Tube	δE	D	A_{buckle}	E_{gap}	δE	D	A_{buckle}	E_{gap}
(3,3)	2.71	8.20	0.43	0.10	6.57	8.3	0.53	0.18
(4,4)	1.30	10.9	0.29	0	4.19	11.1	0.46	0.20
(5,5)	0.68	13.7	0.24	0	2.73	13.8	0.39	0.09
(6,6)	0.35	16.4	0.21	0	1.95	16.5	0.37	0.10
(8,8)	0.32	21.8	0.01	0	1.39	21.9	0.01	0
(3,0)	9.81	4.40	0.58	0.70	14.85	4.73	0.64	0.70
(4,0)	7.16	6.06	0.51	0.62	11.38	6.31	0.57	0.75
(5,0)	5.12	7.70	0.44	0.51	8.86	7.89	0.52	0.62
(6,0)	3.13	9.33	0.37	0.35	6.32	9.47	0.47	0.47
(8,0)	0.50	12.2	0.30	0.16	3.88	12.6	0.42	0.34
(10,0)	0.03	15.7	0.02	0	2.29	15.8	0.03	0

for the same nanotube index. However, since LDA and GGA give very similar band gap predictions for bulk materials, the difference is most likely not due to the treatment of exchange correlation but instead coming from a structural difference. In fact, the GGA generally predicts a larger surface buckling for single-walled nanotubes than LDA (see Table 3.5). Therefore, we plot the same data versus the buckling amplitude instead of diameter in Figure 3.20 — the buckling amplitude is the difference in radial distance of the two types of buckled triangular atoms. We see an approximate collapse of the data on a single curve for both (n,0) and (n,n) nanotubes. Therefore, we believe that to leading order, the band gap for a single-walled nanotube is determined by its buckling amplitude, while the relation of the buckling amplitude to the diameter is more complex but secondary.

To understand the surface buckling in more detail, we have compared the properties of the buckled ground-state of a single-walled nanotube to the same nanotube but with a flat surface. The flat structure is constructed as follows: we know that the atoms that buckle are those corresponding to the atoms of the parent A(1/9) sheet that are in a triangular region. The symmetry breaking leading to the ground state has one of these atoms move inwards and the other move outwards. To generate the flat structure, we simply force these two atoms to remain equivalent by doing a constrained atomic relaxation whereby

Table 3.6: Kinetic energy (E_{kin}), exchange-correlation energy (E_{xc}), electrostatic energy (E_{es}), total energy (E_{tot}) for flat- and buckled-surfaced single-walled boron nanotubes made of sheet A(1/9) based on LDA calculations using SIESTA. For flat cases, energies are in eV/atom. For buckled ones, we show percentage changes of the energies compared to the corresponding flat values ('+' for increase, '-' for decrease).

	Flat-surfaced				Buckled-surfaced			
Tube	E_{kin}	E_{xc}	E_{es}	E_{tot}	δE_{kin}	δE_{xc}	δE_{es}	δE_{tot}
(3,3)	54.90	-29.74	-102.16	-77.00	-0.14	0.05	0.06	-0.007
(4,4)	54.99	-29.76	-102.25	-77.02	-0.09	0.03	0.04	-0.004
(5,5)	55.06	-29.78	-102.31	-77.03	-0.09	0.03	0.04	-0.002
(6,6)	55.05	-29.78	-102.31	-77.04	-0.07	0.02	0.03	-0.001
(8,8)	55.18	-29.82	-102.41	-77.05	-0.28	0.16	0.11	0
(3,0)	54.73	-29.68	-101.92	-76.87	-0.28	0.10	0.11	-0.013
(4,0)	54.86	-29.72	-102.09	-76.95	-0.22	0.06	0.09	-0.009
(5,0)	54.92	-29.74	-102.17	-76.98	-0.19	0.05	0.08	-0.007
(6,0)	54.99	-29.76	-102.24	-77.01	-0.18	0.06	0.08	-0.004
(8,0)	55.03	-29.77	-102.29	-77.03	-0.14	0.05	0.06	-0.001
(10,0)	55.06	-29.78	-102.32	-77.04	-0.01	0.00	0.01	0

we constrain these two atoms to have the same radius measured from the nanotube axis. As expected, for flat surfaces, the single-walled boron nanotubes are all metallic regardless of diameter (e.g., see (3,0) nanotube in Figure 3.19). Table 3.6 shows the changes of different components of the total energy of buckled single-walled boron nanotubes compared to flat ones. For all nanotubes, buckling is always accompanied by a decrease in kinetic energy E_{kin} and increases in E_{xc} and E_{es}, the same as for 2D boron sheets. This strongly suggests that surface buckling in single-walled boron nanotubes is also driven by lowering of kinetic energy.

The total energy differences between flat and buckled nanotubes are found in Tables 3.6 and 3.5. The energy differences per atom are extremely small and decrease to zero rapidly with increasing nanotube diameter: they are at most 15 meV/atom for the smallest diameters. We note that the GGA systematically favors buckled surfaces compared to the LDA and predicts larger energy gains from buckling. Given the extremely small magnitude of these energy differences, it is not clear whether the LDA or GGA is accurate enough to capture them correctly. In fact, a recent work [91] has investigated the geometry of a finite (5,0) single-walled boron nanotube segment using the presumably more accurate MP2 method [92] and concluded that no buckling exists on the surface of this finite nanotube because the buckled configuration has a higher energy. This is in contrast to our results here and previous LDA and GGA-based findings [12, 13]. Hence, we believe that more caution is required regarding the LDA/GGA predictions for such small energy differences and that further studies are required to determine the correct ground-state geometries and electronic properties of single-walled boron nanotubes made from the A(1/9) sheet. However, if surface buckling does in fact take place, the generic monotonic trend of decreasing buckling and decreasing gap with increasing diameter is most likely a robust result. In the next section, we discuss fluctuations in surface buckling assuming that the LDA/GGA predictions for the buckling are valid.

3.3.3 Fluctuations in buckling

The fact that small diameter nanotubes constructed from the A(1/9) sheet are semiconducting is a symmetry breaking phenomenon: the surface of the nanotube buckles in a way that two originally equivalent atoms (per surface unit cell) become inequivalent whereby one moves radially inwards and the other outwards. The existence of two distinct but symmetry-related minima, i.e. a degenerate ground state, allows for the possibility of topological soliton fluctuations at finite temperatures that connect one minimum to the other. A topological soliton represents a stable, non-uniform distribution of an order parameter (surface buckling here) that occurs in a system with several degenerate ground-state configurations: the soliton connects two regions of the system which lie in distinct minima; topological solitons are stable and cannot easily decay because no continuous transformation can map the system back to a trivial uniform distribution in a single minimum [93]. Because the region of the soliton joining the two minima will have a relatively flat nanotube surface, it will be metallic and thus the nanotubes will have semiconducting regions separated by metallic islands. We examine the likelihood of this possibility below: the main motivation is that the energy difference between flat and buckled configurations is quite small so thermal fluctuations might play an important role.

Figures 3.21 and 3.22 show typical results for the energy and band gap of (3,0) and (5,0) nanotubes as a function of buckling amplitude. Figure 3.23 shows the structure of the buckled (5,0) nanotube and also identifies the atoms undergoing the buckling motion. For intermediate buckling amplitudes, the ground-state buckled configuration and the flat

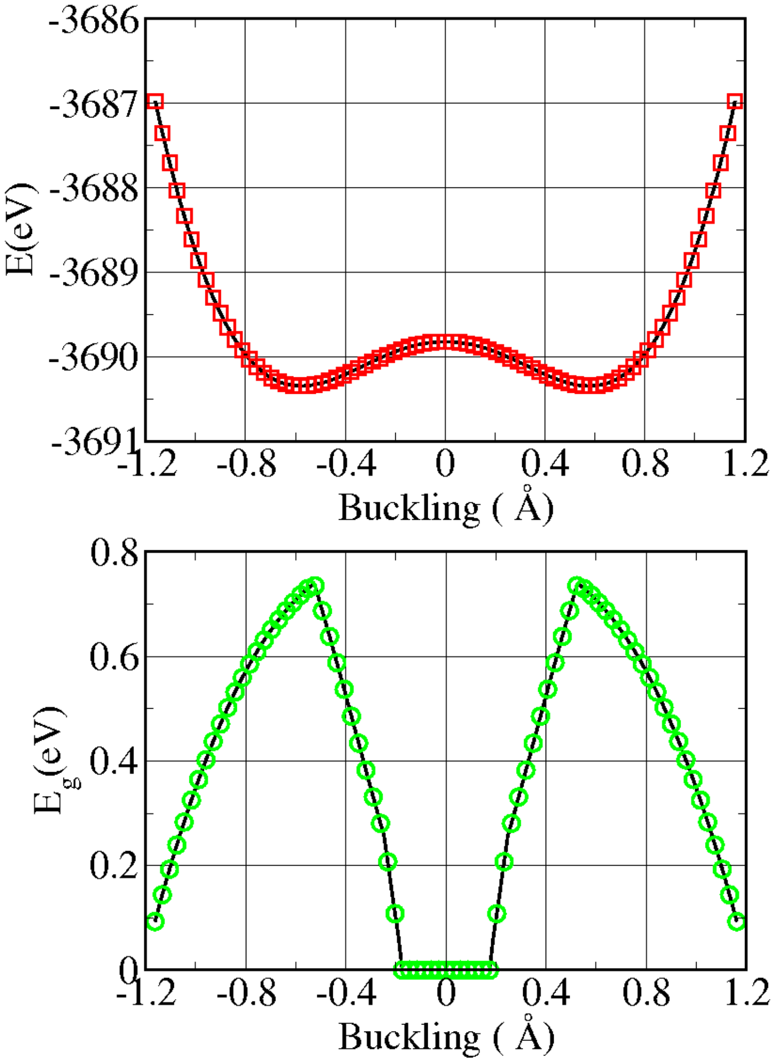

Figure 3.21: Total energy per nanotube primitive cell (top, in eV) and band gap (bottom, in eV) versus buckling amplitude (in Å) for the 48-atom primitive cell of the single-walled boron nanotubes (3,0) (from LDA). Red squares and green circles are the calculated data. Black solid curves are guides to the eye.

configuration are used as endpoints and the intermediate configurations are linearly interpolated between them. The reflection symmetry of the plots in Figure 3.21 and 3.22 is a consequence of the symmetry breaking in the system. The band gap versus bucking is strongly nonlinear and becomes zero for finite small buckling amplitude: therefore, merely having some buckling does not guarantee semiconducting behavior; instead some finite threshold value must be crossed.

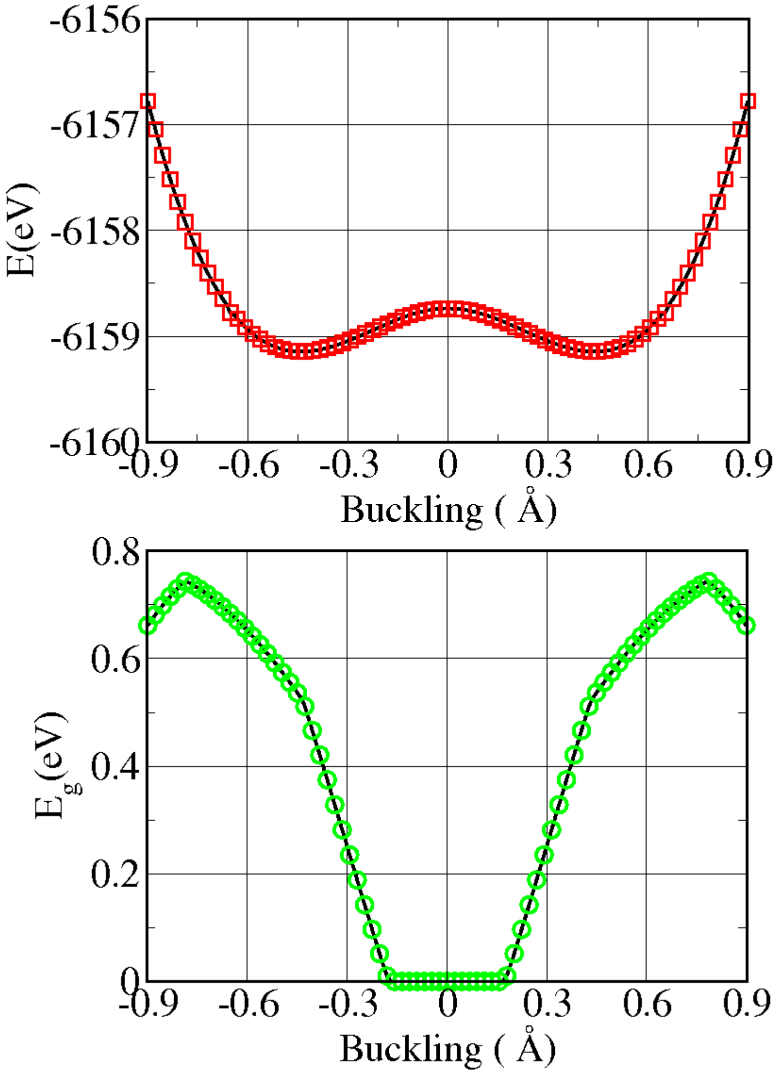

Figure 3.22: Total energy per nanotube primitive cell (top, in eV) and band gap (bottom, in eV) versus buckling amplitude (in Å) for the 80-atom primitive cell of the single-walled boron nanotubes (5,0) (from LDA). Red squares and green circles are the calculated data. Black solid curves are guides to the eye.

For convenience, we will focus on $(n, 0)$ nanotubes. As Figure 3.23 demonstrates for the example of the (5,0) nanotube, all buckling atoms in a $(n, 0)$ nanotube lie on rings about the circumference on the nanotube. Any given ring can be classified by one of three labels: ('i') the ring contains inward buckling atoms, ('o') the ring contains outward buckling atoms, or ('-') the ring does not contain buckling atoms. For the two ground states, the sequence is either the repeated 'io-' pattern or the repeated 'oi-' pattern. An

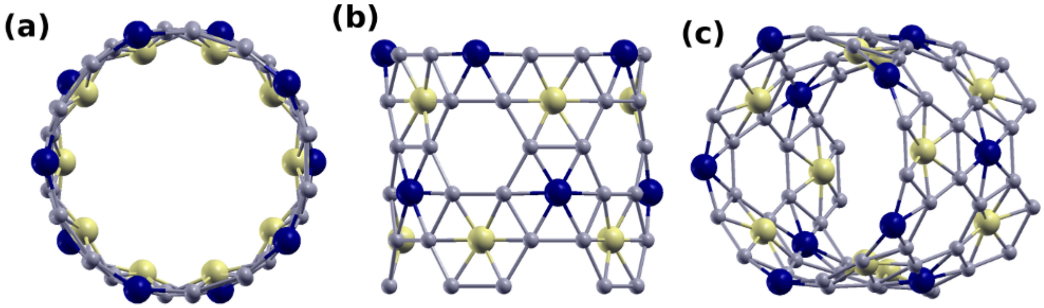

Figure 3.23: Structure of single-walled boron nanotube (5,0): (a) top view, (b) side view and (c) angled view. Big blue (dark) balls are the boron atoms moving outward, big yellow (light) balls show the atoms moving inward and small gray balls show the rest atoms that do not buckle.

abrupt soliton going from one to the other minimum is denoted by '...io-io-oi-oi-...'. Of course, the transition region joining the 'io-' and 'oi-' minima will generally have some width in order to lower the energy, as we detail below.

We extract soliton energies from first principles calculations as follows. For the (3,0) and (5,0) nanotubes, we chose unit cells that were two or three times the respective primitive cell. Starting from the repeated 'io-' ground state, we created abrupt solitons of the 'io-oi' and 'oi-io' variety by fixing the buckling atoms into the appropriate positions and relaxing all other atomic coordinates. Due to periodic boundary conditions, two equivalent solitons are created in the unit, one 'io-oi' and the other 'oi-io'. To allow for wider solitons, we allowed some of the buckling atoms to relax: for example, for a triple-long nanotube, starting from the abrupt 'io-io-io-oi-oi-oi' state, we relaxed to the 'io-io-xx-oi-oi-xx' configuration where all the atoms in the rings denoted by 'x' are allowed to fully relax. An even wider soliton would be 'io-xx-xx-oi-xx-xx'. Table 3.7 contains our first principles LDA results for the energies of the various soliton configurations. Widening the solitons does reduce the energy, but the reduction is most significant when the first pair of buckled rings are allowed to relax. This data suggest that the solitons would be at most four buckling rings wide.

To help us model longer unit cells and other (n,0) nanotubes, we fit our results to a simple model. First, we note that the buckling configuration is specified by the amplitude of a unit of three neighboring rings. For example, 'io-' has optimal positive buckling, 'oi-'

Table 3.7: LDA energy costs for soliton configurations of (3,0) and (5,0) single-walled A(1/9)-derived nanotubes. The "Configuration" column describes the unit cell used and its geometry (see text for the 'i', 'o', '-', and 'x' nomenclature). E_{sol} is the energy per soliton in eV above the ground-state for that configuration. K is the extracted spring constant for the simplified model of Eq. (3.18) in eV/Å^2.

Nanotube	Configuration	E_{sol}	K
(3,0)	io-io-io-io	0	
(3,0)	io-io-oi-oi	1.25	1.89
(3,0)	io-xx-oi-xx	0.86	1.79
(3,0)	io-io-io-io-io-io	0	
(3,0)	io-io-io-oi-oi-oi	1.39	2.04
(5,0)	io-io-io-io	0	
(5,0)	io-io-oi-oi	0.92	2.28
(5,0)	io-xx-oi-xx	0.60	1.98
(5,0)	io-io-io-io-io-io	0	
(5,0)	io-io-io-oi-oi-oi	0.96	2.58
(5,0)	io-io-xx-oi-oi-xx	0.64	2.34
(5,0)	io-xx-xx-oi-xx-xx	0.57	2.39

has optimal negative buckling, and 'xx-' has an intermediate value. Let j index each such three ring unit and A_j be its buckling amplitude. The LDA calculations on a primitive cell of a nanotube provide us with the energy $\mathcal{E}_{coh}(A)$ of coherently buckling the entire length of the nanotube by amplitude A: this is what is shown in Figure 3.21 and 3.22. When there are fluctuations in buckling, in addition to energy changes due to the fact that $\mathcal{E}_{coh}(A)$ depends on A, there will also be energy costs due to the non-uniformity of A_j along the nanotube, which we model by a nearest-neighbor spring model. Thus our model is

$$E_{tot} = \sum_j \mathcal{E}_{coh}(A_j) + \frac{K}{2}\Big(A_{j+1} - A_j\Big)^2, \tag{3.18}$$

where K is the spring constant for A_j variations along the length. Using this model together with the *ab initio* data of Table 3.7 and the actual A_j values from the associated structures, we back out K for each case and list them in Table 3.7. Despite the simplicity of the model, there is a general agreement for the extracted K: $K \approx 1.8$ eV/Å^2 for the (3,0) nanotube and $K \approx 2.3$ eV/Å^2 for the (5,0) nanotube. Based on this, we assume that $K \approx 2$ eV/Å^2 is a reasonable value of K for all (n,0) nanotubes. To extend this model to all (n,0) nanotubes, we observe that the function $\mathcal{E}_{coh}(A)$ for the (3,0) and (5,0) nanotubes

Table 3.8: Soliton energies for the (n,0) nanotubes in eV/soliton based on the model of Eq. (3.18) with $K = 2$ eV/Å^2. The predictions based on LDA and GGA are presented separately.

Nanotube	LDA E_{sol}	GGA E_{sol}
(3,0)	0.73	0.97
(4,0)	0.62	0.85
(5,0)	0.50	0.75
(6,0)	0.36	0.62
(8,0)	0.14	0.50
(10,0)	0.001	0.003

is fit quite accurately by a fourth-order polynomial $\mathcal{E}_{coh}(A) = E_{coh}(0) + gA^2 + hA^4$; we extract the two constants g and h by reproducing the two important data for each (n,0) nanotube in Table 3.5: that the minima occur at $A = \pm A_{buckle}$ and that the buckled configurations at $\pm A_{buckle}$ are δE lower in energy than the flat one at $A = 0$.

Solving for solitons of the energy function of Eq. (3.18) is straightforward. We consider a 100-long chain of rings, constrain the left 30 to be in the 'io-' configuration, the right 30 to be in the 'oi-' configuration, and relax the interior 40 rings to minimize E_{tot}. The resulting solitons turn out to be quite narrow, typically 2-4 buckling rings at most. The resulting energies per soliton from this model for a range of (n,0) nanotubes are shown in Table 3.8. We note that the LDA-based soliton energies are smaller than the GGA-based ones simply because, as Table 3.5 shows, the LDA predicts a smaller energy difference between the flat and buckled configuration and a smaller buckling amplitude.

The results in Table 3.8 show that, even at room temperature, the average spacing between solitons — given by $\exp(E_{sol}/k_BT)$ lattice spacings — is quite large even for the semiconducting (8,0) nanotube within LDA: for the (8,0), the average soliton-soliton spacing is some 200 unit cells. Although solitons are much more closely spaced for the (10,0) or larger tubes, these are already metallic nanotubes (see Table 3.5). Therefore, the soliton fluctuations are sparse enough that, for the nanotubes with semiconducting ground states, most of the nanotube length in practice will be composed of semiconducting regions separated by rare and narrow metallic segments.

The model of Eq. (3.18) also allows us to estimate the effect of thermal fluctuations about each buckled configuration on the band gap of the nanotube: Figures 3.21 and 3.22 show that as the buckling amplitude fluctuates about its minimum value, the band gap values for the nanotube generally decrease since they are close to maximal at the optimal buckling configuration. However, classical Monte Carlo sampling using Eq. (3.18) reveals that the fluctuations for the semiconducting nanotubes — even up up to (8,0) — only create a modest reduction of the average band gap value during the sampling.

Summarizing this section, we find that although thermal or soliton fluctuations are possible, the energetics of the semiconducting single-walled nanotubes prevent them from modifying the nanotube electronic properties significantly from those of the predicted ground-state structures. Namely, even including thermal fluctuations at room temperature, the single-walled nanotubes that are predicted to have a semiconducting ground state should in fact be semiconducting over most of their lengths.

3.4 Double-walled boron nanotubes

Although single-walled boron nanotubes show very interesting properties such as a metal-insulator transition versus tube diameter, given that double-layered boron sheets are more stable than single-layered ones, we should consider the question of whether single- or double-walled nanotubes are the proper ground state for boron nanotubes of small to medium diameter. As per Sec. 3.2, the double-Z(1/12) sheet is 0.135 eV/atom more stable than the most stable single-layered A(1/9) sheet. Thus, large-diameter double-walled nanotubes made of double-Z(1/12) are guaranteed to be more favorable than single-walled ones. However, smaller diameter double-walled nanotubes have large curvatures, which makes it harder to predict the structure and properties ahead of time.

The aim of this section is to study the structures, energetics and electronic properties of double-walled boron nanotubes and to compare them to single-walled ones as a function of diameter. Here, we will consider three classes of double-walled nanotubes: a) the most obvious structures are obtained by creating double-walled nanotubes by rolling up the highly stable double-Z(1/12) sheet as it is; b) double-walled nanotubes made from two coaxial single-walled A(1/9)-derived nanotubes of different diameters; and c) double-walled nanotubes constructed from coaxial single-walled Z(1/12)-derived nanotubes of different

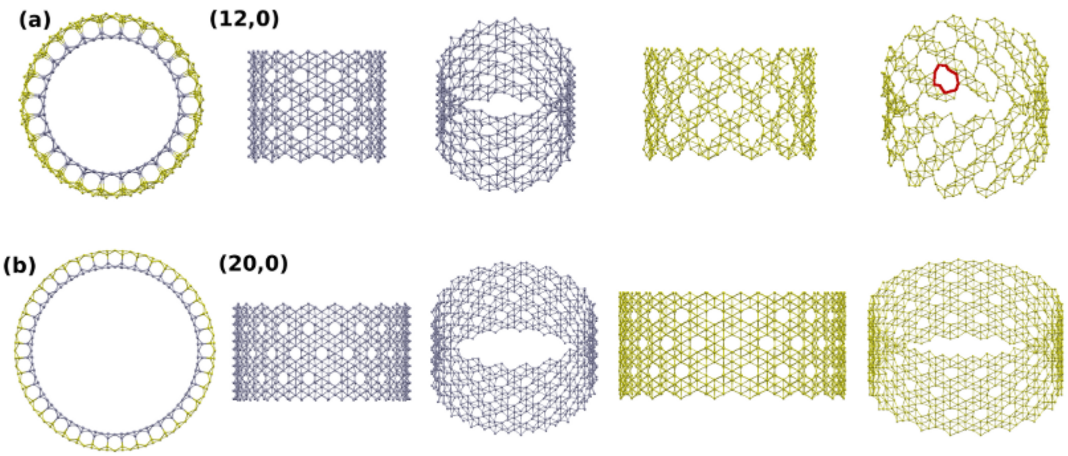

Figure 3.24: Structures of nanotubes (a) (12,0) and (b) (20,0) made of the double-Z(1/12) sheet. The first column shows the structure of each nanotube viewed down its axis. In the next four columns, we show the geometry of the inner and outer walls (surfaces) separately: the second and third columns show a side and angled view of the inner surface, and the fourth and fifth columns show the side and angled view of the outer surface. To help the reader, inner surface atoms are shown in gray (darker) while outer surface atoms are shown in yellow (lighter). In the fifth row, red solid lines mark an example of a structural "hole" that is formed for the (12,0) nanotube on its outer surface due to broken boron-boron bonds.

diameters. Clearly, these three possibilities do not exhaust all the possibilities for double walled nanotubes, but we believe that they form a reasonable set of structures to study for an initial orientation and investigation and have a high chance of including the actual ground-state structure for double-walled boron nanotubes.

3.4.1 Double-walled nanotubes from the double-Z(1/12) sheet

We first consider double-walled boron nanotubes constructed by rolling up the most stable double-layered Z(1/12) sheet. Although this sheet is the most stable in our library, it is expected to be quite stiff under curvature compared to any single-layered sheet because its inner and outer walls have the same number of atoms but are geometrically forced to have different diameters (radii of curvature) which stretches the outer surface, compresses the inner surface, and strains the interlayer bonds. Figure 3.24 shows two examples of such nanotubes.

First principles results support this expectation. Figure 3.25 shows the curvature energy versus outer nanotube diameter for such double-walled nanotubes. The curvature energies

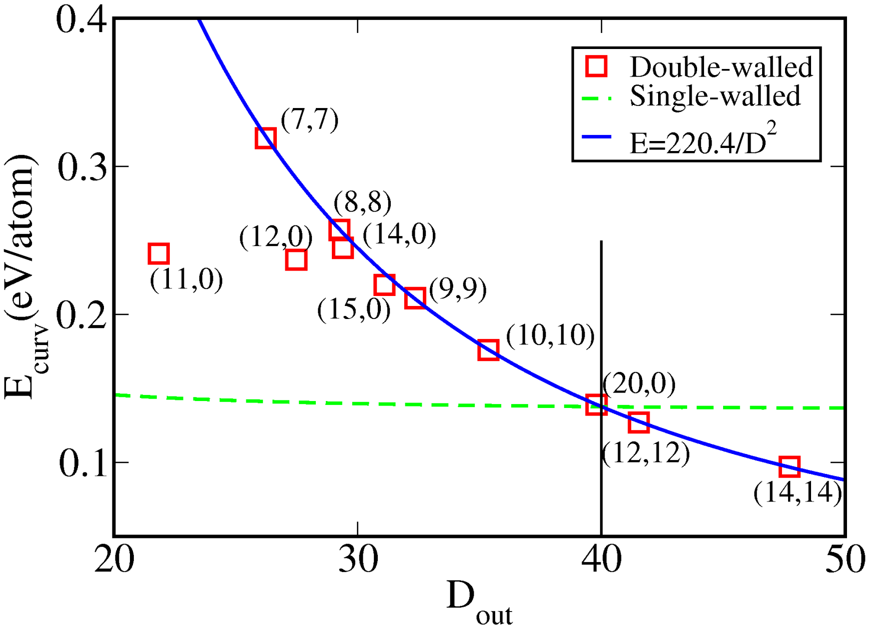

Figure 3.25: Red squares are the curvature energies E_{curv} (in eV/atom) versus outer wall diameter D_{out} (in Å) for double-walled nanotubes made from rolling the double-Z(1/12) sheet. The blue solid line is the result of a $1/D_{out}^2$ fit to all the data excluding the anomalous (11,0) and (12,0) cases (those two show structural collapse due to high curvature as per Figure 3.24). The green dashed line shows the curvature energies for single-walled A(1/9)-derived nanotubes with an added constant energy of 0.135 eV/atom to account for the energy difference between the A(1/9) and double-Z(1/12) sheets. The two curves cross at $D_{out} \approx 40$ Å. All data are calculated with SIESTA with the LDA approximations.

are about an order of magnitude larger than those of carbon nanotubes and single-walled boron nanotubes of the same diameter. It turns out that due to the very high curvatures, some of the bonds on the outer surfaces of the smallest-diameter double-walled nanotubes of this class break to release tension. As shown in Figure 3.24, many boron-boron bonds in the outer surface of the (12,0) nanotube are broken, forming "holes" on that surface, while for the (20,0) nanotube, the outer surface has the same geometry as the Z(1/12) sheet with no broken bonds. For the smallest diameter nanotubes we have considered of this class, namely (11,0) and (12,0), this strain release mechanism tends to reduce the curvature energies below the expected elastic trend of a $1/D_{out}^2$ behavior (see Figure 3.25). Electronically, all the double-walled nanotubes without broken bonds on the outer walls are semiconducting, as expected from the semiconducting nature of the parent double-Z(1/12) sheet.

After excluding the anomalous (11,0) and (12,0) cases, we can fit the remaining data in Figure 3.25 corresponding to $D_{out} > 25$ Å very well with the standard elastic formula of Eq. (3.17). We obtain C=220 eVÅ^2/atom. This is about 50 times larger than the corresponding value for single-walled A(1/9)-derived nanotubes. By accounting for the 0.135 eV/atom difference in energy between the A(1/9) sheet and the double-Z(1/12) sheet, we find a crossover in stability from single-walled to double-walled at a diameter of $D_{out} \approx 40$ Å. Hence, if we only compare these two classes of nanotubes, we would have the following progression: the ground-state is double-walled and semiconducting for $D > 40$ Å and single-walled for $D < 40$ Å; as per the previous section, for $20 < D < 40$ Å, the single-walled tubes are metallic and for $D < 20$ Å they are semiconducting.

3.4.2 Double-walled nanotubes from two A(1/9) sheets

As we saw above, although double-Z(1/12) is the most stable sheet, its large curvature energy makes it unfavorable for small diameter nanotubes. The large curvature cost is due to the fact that we are constructing double-walled nanotubes by using two identical sheet segments to construct the inner and outer walls. This in turn causes a great deal of strain as neither surface can be optimized.

Obviously, one can reduce the strain greatly by constructing double-walled nanotubes with inner and outer surfaces of differing diameters. Although one can attempt to choose inner and outer surfaces (i.e. single-walled nanotubes) that are each optimal separately, when putting them together to make a double-walled structure, one will sacrifice the optimal bonding between the two that was guaranteed in the sheet structure when both were the same sheet. Therefore, *a priori* it is not obvious in which diameter regimes such a program will be successful, and we must rely on first principles results to provide guidance. This situation is directly analogous to multi-walled carbon nanotubes [94] but with the added complication that for boron strong inter-wall chemical bonds can form. This section and the next investigate the properties of double-walled nanotubes constructed from different-sized inner and outer single-walled nanotubes.

To begin, we will focus on double-walled nanotubes made from two single-walled A(1/9)-derived nanotubes. The rationale is that the A(1/9) sheets normally don't form strong interlayer bonds, so that we may avoid or at least minimize the complication due to inter-layer bonding. Our approach to finding optimal double-walled structures is the following: for a fixed chosen outer single-walled nanotube, we choose a number of inner nanotubes, perform full relaxations of the resulting double-walled structures, and locate the lowest-energy resulting combination. We then tabulate our results as a function of the outer tube. Although other schemes are imaginable, we choose the outer diameter as the independent variable primarily because current methods for fabrication of boron nanotubes [35] (as well as some non-boron nanotube growth methods) use a hollow cylindrical physical template inside of which the nanotube is constrained to grow. Thus the exterior diameter is the variable most obviously constrained by the experimental setup.

We label these double-walled nanotubes in the following manner: we provide the name of the sheet used to create the nanotubes followed by a pair of (n, m) labels specifying the outer and then inner nanotube. Therefore, A(1/9)-(8,0)-(4,0) refers to a double-walled nanotube constructed from the (8,0) and (4,0) single-walled A(1/9)-derived nanotubes. For computational convenience, we only consider double-walled tubes where inner and outer nanotubes are both $(n, 0)$ or both (n, n): this means both single-walled nanotubes are commensurate and thus we can model the double-walled tubes using periodic boundary conditions with relatively small periodic unit cells along the nanotube axis.

Table 3.9 presents the binding energy as a function of various inner-outer pairings for A(1/9)-$(n, 0)$-$(m, 0)$ and A(1/9)-(n, n)-(m, m) double-walled nanotubes. For both groups, the tabulated data show that the optimal combinations are A(1/9)-(n,0)-(n-3,0) and A(1/9)-(n, n)-(n-2,n-2). Geometrically, we find that bonds form between the inner and outer walls in all the cases studied here. Figure 3.26 shows two such examples. The inter-wall bond lengths are in the range of 1.7 to 1.9 Å. The distances between the walls of inner and outer nanotubes are 2.8∼3.2 Å for A(1/9)-$(n, 0)$-$(m, 0)$ type and 3.2∼3.6 Å for A(1/9)-(n, n)-(m, m) type double-walled nanotubes, which are close to the interlayer distance of 3.49 Å in the double-A(1/19) sheet (see Table 3.4). Electronically, the formation of the inter-wall bonds changes the buckling pattern on both inner and outer surfaces and renders all the double-walled nanotubes investigated here metallic. For example, Figure 3.26 shows the relevant band structures in the case of A(1/9)-(6,0)-(3,0): the double-walled nanotube has multiple bands crossing the Fermi energy even though the individual constituent (3,0) and

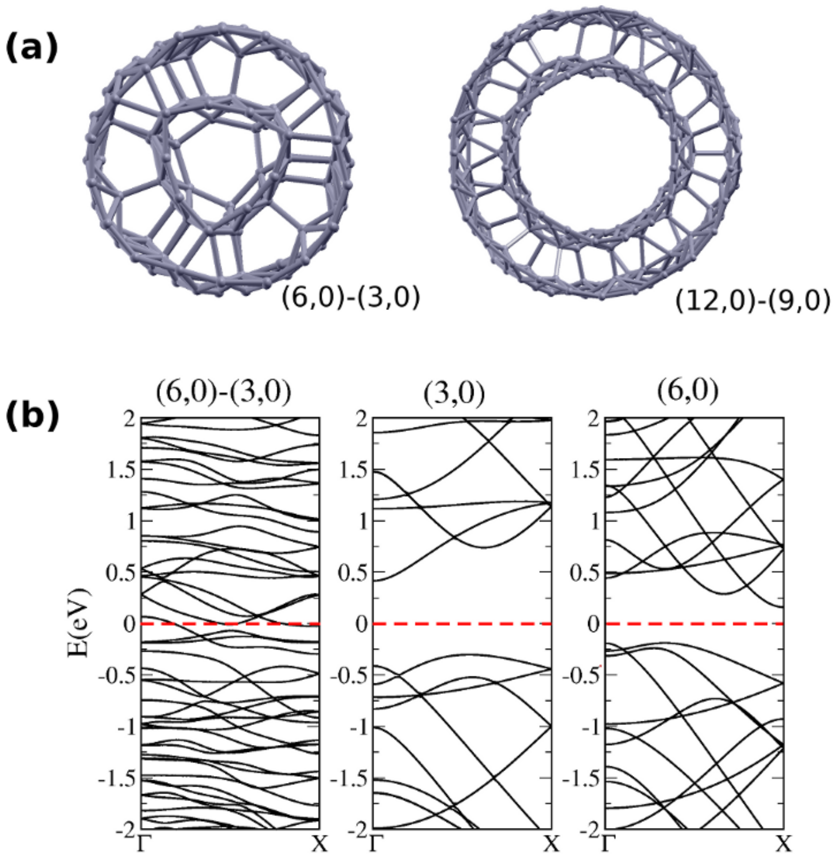

Figure 3.26: (a) Atomic geometries of the double-walled boron nanotubes A(1/9)-(6,0)-(3,0) and A(1/9)-(12,0)-(9,0) viewed down the nanotube (z) axis. See text for nomenclature. (b) LDA bandstructure of the double-walled A(1/9)-(6,0)-(3,0) nanotube compared to the constituent single-walled (3,0) and (6,0) cases. In all cases, the energies are shifted so that the Fermi energies are at zero.

(6,0) nanotubes are semiconducting.

We note that our results are restricted to relatively small diameter double-walled nanotubes which have relatively large curvatures: the largest nanotube in our library is A(1/9)-(18,0)-(15,0), which has an outer diameter of 28.9 Å and still has inter-walled bonds formed between inner and outer nanotubes. Although we are presently unable to directly verify the properties of larger diameter double-walled nanotubes through explicit calculations, we can make some general arguments. For very large diameters, we expect weak curvature effects, which means each nanotube is quite close to being a flat A(1/9) sheet. As described in Sec. 3.2, two A(1/9) sheets stay flat and apart at a distance of 3.49 Å and do

Table 3.9: Binding energy in eV/atom of double-walled boron nanotubes made from two distinct coaxial single-walled A(1/9) nanotubes (calculated by SIESTA with the LDA approximation). We only consider cases where both inner and outer tubes are both of $(n,0)$ (up panel) or (n,n) (bottom panel) variety. Larger binding energies correspond to more stable structures.

		Outer $(n,0)$						
		12	11	10	9	8	7	6
	10	7.37	-	-	-	-	-	-
	9	7.42	7.36	-	-	-	-	-
	8	7.40	7.42	7.33	-	-	-	-
Inner	7	7.39	7.40	7.42	7.32	-	-	-
$(m,0)$	6	7.37	7.39	7.39	7.42	7.37	-	-
	5	7.36	7.36	7.38	7.40	7.41	7.37	-
	4	7.35	7.35	7.35	7.37	7.40	7.40	7.33
	3	7.34	7.33	7.33	7.33	7.35	7.35	7.38

		Outer (n,n)				
		8	7	6	5	4
	7	7.41	-	-	-	-
	6	7.43	7.40	-	-	-
Inner	5	7.40	7.43	7.39	-	-
(m,m)	4	7.37	7.39	7.45	7.39	-
	3	-	7.36	7.38	7.43	7.39
	2	-	-	7.35	7.36	7.43

not form chemical bonds. Therefore, such large diameter double-walled boron nanotubes will be similar to double-walled carbon nanotubes in that there will be weak van der Waals interactions between the walls. We would expect the inter-wall distance to be quite close to 3.49 Å. This fixed distance (i.e. fixed diameter difference) allows us to estimate that the optimal combinations for large diameters will be A(1/9)-$(n,0)$-(n-4,0) and A(1/9)-(n,n)-(n-2,n-2) for (n,n). Notice that the optimal combination for large-diameter $(n,0)$ type nanotubes is different from small-diameter ones. Electronically, we expect such double-walled nanotubes to be metallic since each individual constituent single-walled nanotube is metallic by itself.

We now compare the stability of these double-walled boron nanotubes to the A(1/9)-derived single-walled ones. Figure 3.27 shows the total energy per atom versus outer diameter for these two classes of nanotubes. In all cases studied here, the double-walled are more stable than the single-walled variety, typically by 0.05 eV/atom. As the Figure shows,

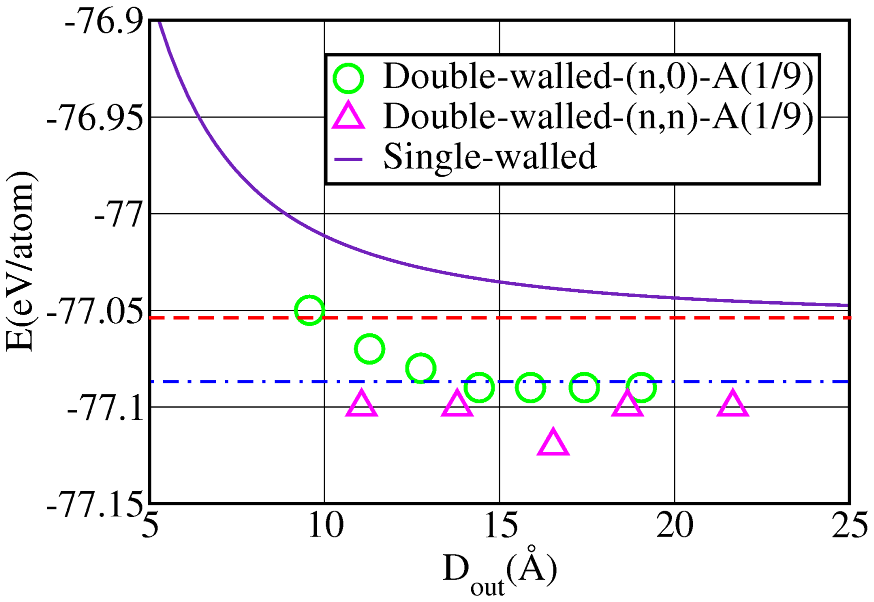

Figure 3.27: Total energies (from LDA) per atom versus outer diameter D_{out} for single-walled A(1/9)-derived nanotubes (solid indigo curve), double-walled A(1/9)-(n,0)-(n-3,0) for n=6–12 (green circles), and double-walled A(1/9)-(n,n)-(n-2,n-2) for n=4–8 (magenta triangles). The red dashed line is the energy of a single flat A(1/9) sheet. The blue dot-dash straight line shows the energy of the double-A(1/9) sheet.

the energies in both cases have essentially asymptoted to the respective sheet energies, so we expect this relative stability to also hold for larger diameters. We note that the energy of large diameter double-walled nanotubes asymptotes to the energy of the double-A(1/9) sheet, which is some 0.03 eV/atom more stable than the single-walled A(1/9) sheet due to weak inter-sheet interactions. There appears to be some chirality dependence to the data as the A(1/9)-(n,n)-(n-2,n-2) are lower in energy than the A(1/9)-(n,0)-(n-3,0), but at present we do not have a detailed understanding of this difference. In brief, this section shows that for all diameters envisioned, double-walled A(1/9)-derived nanotubes will be more stable than their single-walled varieties. Furthermore, we expect all the A(1/9)-derived double-walled nanotubes to be metallic.

3.4.3 Double-walled nanotubes from two Z(1/12) sheets

We just have shown that double-walled nanotubes constructed from the A(1/9) sheet are always more stable than single-walled ones for all diameters. Since the double-Z(1/12)

Table 3.10: Binding energy in eV/atom of double-walled boron nanotubes made from two coaxial single-walled Z(1/12) nanotubes (calculated by SIESTA with the LDA approximation). We only consider cases where both inner and outer tubes are (*n*,0) (left) or (*n*,*n*) (right) type. Larger binding energies correspond to more stable structures.

		Outer (*n*,0)				
		10	9	8	7	6
Inner (*m*,0)	8	7.44	-	-	-	-
	7	7.49	7.45	-	-	-
	6	7.43	7.47	7.43	7.27	-
	5	-	7.41	7.47	7.42	7.28
	4	-	-	7.40	7.49	7.43
	3	-	-	7.32	7.41	7.47

		Outer (*n*,*n*)			
		8	7	6	5
Inner (*m*,*m*)	7	7.41	-	-	-
	6	7.51	7.40	-	-
	5	7.35	7.49	7.40	-
	4	7.33	7.34	7.48	7.43
	3	-	7.33	7.33	7.47
	2	-	-	7.31	7.32

sheet is more stable than the double-A(1/9) sheet (see Table 3.4), we might further stabilize double-walled nanotubes by pairing two coaxial single-walled Z(1/12) nanotubes of different diameters.

We follow the same program as in the previous section for the A(1/9)-derived double-walled nanotubes when constructing double-walled structures. Again, for simplicity, we consider only the cases where both inner and outer nanotubes are both $(n, 0)$ or both (n, n). We employ the same nomenclature as the previous section, so that Z(1/12)-(n, m)-(p, q) is a double-walled nanotube with outer single-walled tube (n, m) and inner single-walled tube (p, q) and where both single-walled nanotubes are made from curving a Z(1/12) sheet.

Table 3.10 presents the binding energy for different combinations of inner and outer nanotubes. The optimal combinations are (*n*,0)-(*n*-3,0) and (*n*,*n*)-(*n*-2,*n*-2). Figure 3.28 shows the structures of Z(1/12)-(9,0)-(6,0) and Z(1/12)-(8,8)-(6,6). In all cases we have studied in this work, as exemplified by Figure 3.28, we find that interlayer bonds form between the inner and outer surfaces with a bond length close to 1.7 Å. The fact that such bonds form is no surprise since the double-Z(1/12) sheet has interlayer bonds of the same length. However, the number of bonds formed is harder to predict: since the inner and outer tubes have different number of atoms, not all the bonds that form in the sheet geometry are possible in the tube geometry. More careful examination shows that the two classes of double-walled nanotubes solve this frustration in opposite manners: more inter-tube bonds than expected form for the Z(1/12)-(*n*,0)-(*n*-3,0) cases, while too few bonds

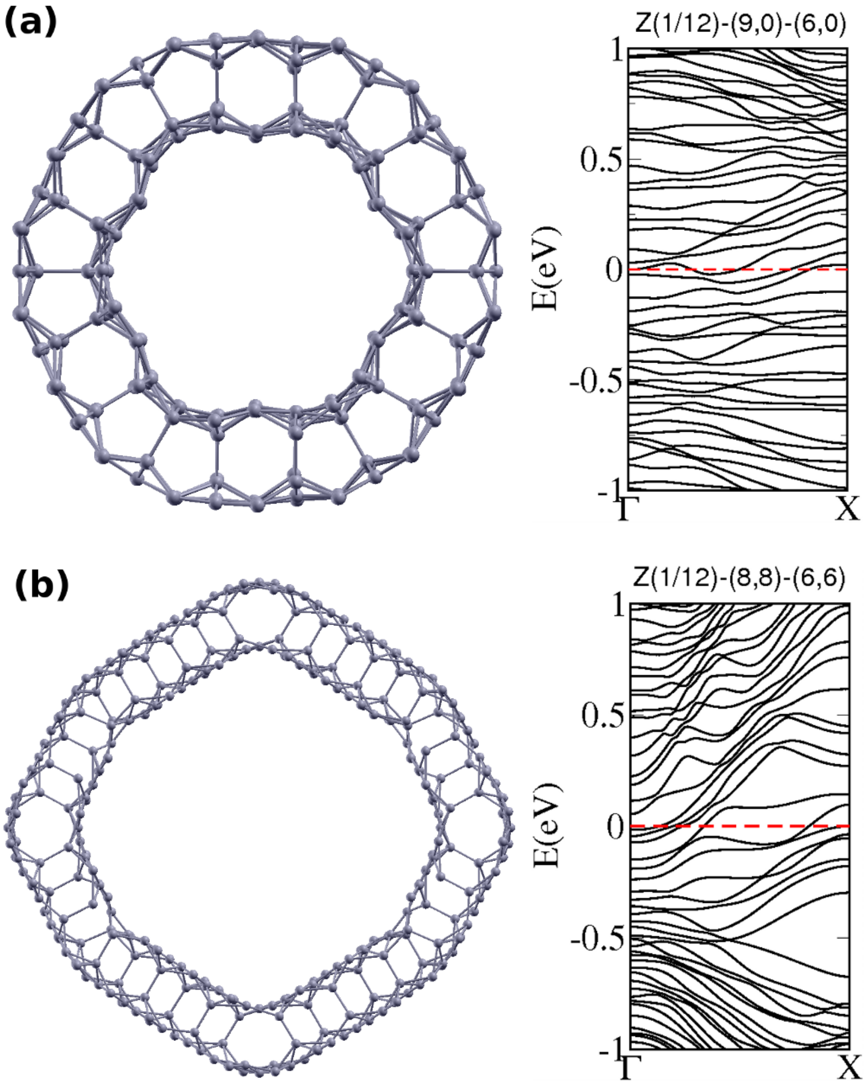

Figure 3.28: Atomic geometries viewed down the nanotube axis and LDA bandstructures for the (a) Z(1/12)-(9,0)-(6,0) and (b) Z(1/12)-(8,8)-(6,6) double-walled nanotubes. Fermi levels are at zero (energies are shifted accordingly) and denoted by the red horizontal dashed lines.

are formed in the Z(1/12)-(n,n)-(n-2,n-2) cases. Put another way, the Z(1/12)-(n,0)-(n-3,0) structures have the right number of bonds for the outer tube but too many for the inner tube, and the Z(1/12)-(n,n)-(n-2,n-2) have the opposite behavior. This is visible in Figure 3.28: for Z(1/12)-(9,0)-(6,0) we see a regular alternating buckling pattern on the outer wall whereas for Z(1/12)-(8,8)-(6,6) the inner wall features the alternative regular buckling.

The consequence of this "defective" interlayer bonding pattern on the electronic structure is that all such double-walled nanotubes we have studied are metallic. Figure 3.28 shows two examples of the band structures. This is different from the semiconducting nature of the double-Z(1/12) sheet or the double-walled nanotubes made directly from the double-Z(1/12) sheet of Sec. 3.4.1. An analysis of the local densities-of-states of these small-diameter double-walled nanotubes shows that the states at the Fermi level are extended to the whole structure rather then being localized around the structural defects.

Due to computational limitations, the sample of double-walled nanotubes we present here from first principles is limited to small diameters. Although we are not yet able to directly simulate larger diameter nanotubes, we can present general arguments to deduce their likely properties. Clearly, for very large diameters, in order to minimize the total energy, the local structure of such double-walled nanotubes will converge to the structure of the double-Z(1/12) sheet and the distance between the inner and outer walls will be close to 3.23 Å as appropriate to the double-layered sheet. This means that the optimal combinations will be (n,0)-(n-3,0) and (n,n)-(n-2,n-2), which are the same as found for the small diameter cases. Furthermore, since the inner walls have fewer atoms than the outer walls, the structural defects related to frustrated interlayer bonding persist for all large diameter double-walled nanotubes, and we thus expect them to be metallic as well. Quantitatively, the number of structural defects per unit nanotube length is constant for either (n,0)-(n-3,0) or (n,n)-(n-2,n-2) classes because the number of the defects is proportional to the constant difference in the number of atoms between inner and outer walls: the linear density of defects per unit length will not depend on diameter but only possibly on chirality.

We now turn to the comparative energetics for this class of double-walled nanotubes. Figure 3.29 shows the total energy per atom versus outer wall diameter for this class in comparison to those of the single-walled A(1/9)-derived nanotubes and the double-walled A(1/9)-derived nanotubes. For the range of diameters examined, double-walled nanotubes made from two coaxial Z(1/12) single-walled nanotubes are always the most stable. As discussed in Sec. 3.4.1, single-walled A(1/9)-derived nanotubes are more stable than double-walled nanotubes rolled up directly from the double-Z(1/12) sheet for $D_{out} <$

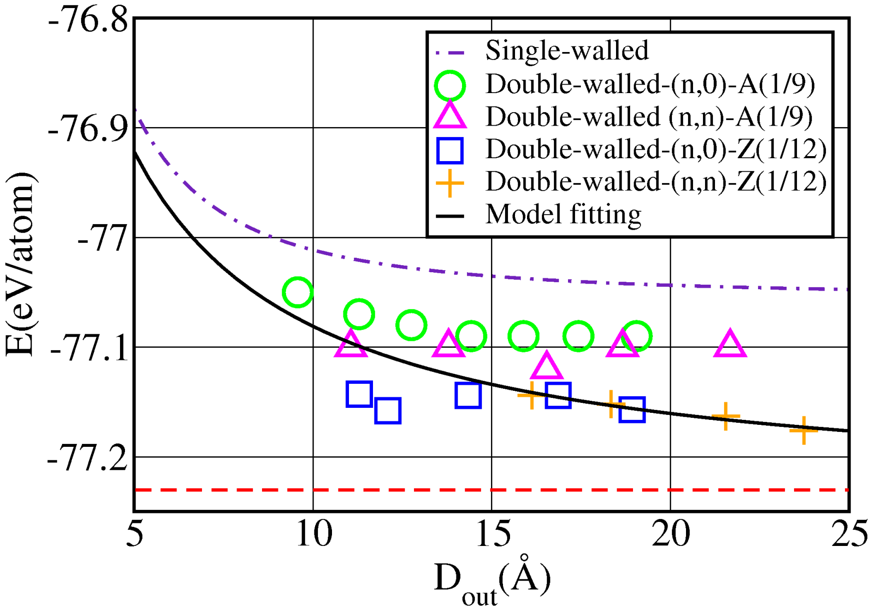

Figure 3.29: Total energies (from LDA) per atom versus outer diameter D_{out} for single-walled boron nanotubes (indigo dot-dash line), double-walled boron nanotubes made of A(1/9) single-walled nanotubes (green circles and magenta triangles), and double-walled boron nanotubes from two Z(1/12) single-walled nanotubes (blue squares and yellow plus). The red dashed line shows the energy of the double-Z(1/12) sheet. The black solid curve is a fitting to squares and plus in the range of 15 Å $< D_{out} <$ 25 Å.

40 Å. Therefore, at least for $D_{out} < 40$ Å, metallic double-walled nanotubes constructed from two different concentric Z(1/12) single-walled nanotubes are our best candidate for the ground state structure.

To predict the ground state for $D_{out} > 40$ Å, we compare the metallic double-walled nanotubes made from two different concentric Z(1/12) single-walled nanotubes with the semiconducting ones based on the double-Z(1/12) sheet. From Sec. 3.4.1, the latter group has an energy per atom given by

$$E = E[\text{double-Z}(1/12)] + (220.4\ \text{eVÅ}^2)/D_{out}^2\,, \tag{3.19}$$

where E[double-Z(1/12)] is the energy per atom for the double-Z(1/12) sheet. For the former group, when tube diameter becomes very large, they are essentially gently curved double-Z(1/12) sheets with a fixed number of structural defects per unit length. So the total energy has two important contributions: the total energy per atom of the double-Z(1/12) sheet and the energy increase due to the structural defects — the curvature energy is minimized by choosing optimal choice of inner and outer walls and we assume it can be neglected (if it were to be included it would be a small sub-leading term of order $1/D_{out}^2$). Since the number of defects per unit length is constant regardless of tube diameter, we assume that each defect increases the total energy by a constant amount, which when divided by the number of atoms gives a contribution proportional to $1/D_{out}$. So we expect the total energy for large diameters to be given approximately by

$$E = E[\text{double-Z}(1/12)] + S/D_{out}\,, \tag{3.20}$$

for some constant S. We fit the available data in Figure 3.29 for 15 Å $< D_{out} <$ 25 Å and find $S = 1.59$ eVÅ. Comparing the above two formulae gives a crossing at $D_{out} = 139$ Å. Therefore, we can safely state that, for the experimentally fabricated range of nanotubes with $D_{out} < 100$ Å [35], our best candidates for the ground-state are double-walled boron nanotubes constructed from two different concentric Z(1/12) single-walled nanotubes. All such nanotubes are computed to be or are expected to be metallic.

3.5 Summary

We have presented structures and electronic properties of single-layered and double-layered boron sheets, single-walled and double-walled boron nanotubes. Although boron is the neighbor of carbon in periodic table, boron nanostructures have distinct properties to carbon, which is mainly due to the electron deficiency of boron. Boron has three valence electrons but four atomic orbitals ($2s$, $2p_x$, $2p_y$, $2p_z$) which makes it impossible for boron to form regular electron bonding. Instead three-center or even multi-center bonds are necessary for the stability of boron structures. This electron deficiency has resulted in unique 2D boron sheet structures which are made of mixtures of hexagons and triangles, with atoms in the triangular regions acting as electron donors. Because all other boron nanostructures we have investigated are based on boron sheets, the peculiar structures of boron sheets have consequently determined various properties of other boron nanostructures.

We have explained the stability of boron sheets by the balance of two-center bonding in the hexagonal regions and three-center bonding in the triangular regions. Particularly, we discovered a self-doping phenomenon in boron sheets that adding or removing atoms to hexagon centers does not change the number of bonding states but merely increases or decreases the number of electrons. With self-doping, a close connection between boron and carbon nanostructures can be drawn – starting from a carbon nanostructure, a corresponding boron nanostructure can be built by adding extra atoms to hexagon centers. Self-doping can be further employed to help search for stable Mg boride sheet structures. In addition, these atomically thin boron sheets are not always flat, and some sheets prefer buckled groundstate geometries. This buckling phenomenon is in contradiction to the σ-π mixing picture and can be well explained through a nonconventional electron gas description. With two single-layered boron sheets stacking together, double-layered boron sheets can have interlayer bonds formed if the constituent single-layered boron sheet has a buckled groundstate. The most stable double-layered boron sheet is metallic with a band gap of 0.8 eV. For single-walled boron nanotubes based on the α sheet, their curvature energies are smaller than single-walled carbon nanotubes. Under large curvature, single-walled boron nanotubes become semiconducting with buckled surfaces. Although the energy gains from opening gaps around Fermi levels are very small, the semiconducting behavior of small boron nanotubes is quite robust under soliton perturbation. For double-walled boron nanotubes, the optimal structures have smaller inner nanotubes than outer nanotubes, releasing large strain which will otherwise exist. The most stable double-walled boron nanotubes are always more stable than single-walled ones and are metallic.

Chapter 4

Mg boride nanostructures

Mg boride nanostructures can be constructed by doping pure boron nanostructures with Mg. The added Mg atoms act as another source of electrons in addition to the boron atoms in triangular regions and tend to change the boron substructures as well as many other properties. In this chapter, we discuss novel properties caused by Mg doping and explore the phase diagrams of Mg boride nanostructures in order to find the most stable phases.

4.1 Negative curvature energy

We start with presenting negative curvature energies in Mg boride nanotubes. In most nanotubular systems, e.g., carbon and boron nitride nanotubes, it always costs energy to bend the covalent bonds when rolling up the precursor sheet into nanotubes. In other words, these nanotubes all have positive curvature energies which increase quadratically with curvature. On the other hand, Mg boride nanostructures are rather peculiar. We have discovered that the curvature energy is negative for many Mg doped boron sheets. Equivalently, certain Mg doped boron sheets prefer to curve themselves automatically into nanotubes, which is a unique phenomenon and has not been seen in other nano-systems. As examples, we show nanotubes built from two precursor sheets – the Mg doped α sheet and the Mg doped hexagonal sheet.

We first discuss the Mg doped α sheet with Mg:B = 1:8 where all Mg atoms stay on the same side of the boron sheet. The structure is shown in Fig. 4.1. When constructing

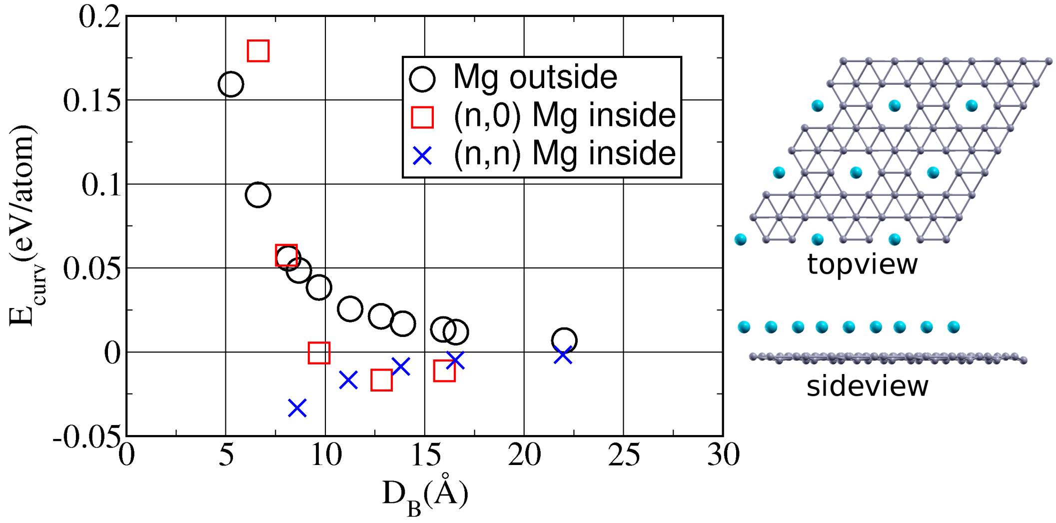

Figure 4.1: (Left) Curvature energy per atom versus diameter of the constituent boron nanotube for nanotubes made of Mg doped α sheet with Mg:B=1:8. (Right) Structure of Mg doped α sheet with Mg:B=1:8. Large blue balls are Mg, small gray balls are B.

a nanotube from this sheet, it is possible to place Mg atoms either inside or outside the nanotube. These two kinds of geometries result in different curvature energies. Figure 4.1 shows the curvature energy versus diameter for nanotubes made of this Mg doped α sheet with Mg inside or outside. We see that nanotubes with Mg inside generally have smaller curvature energy than those with Mg outside. More importantly, for nanotubes with Mg inside, their curvature energies are negative for a wide range of diameters for both (n,0)- and (n,n)-type. In addition to the Mg doped α sheet, negative curvature energy is also observed in nanotubes made of the hexagonal MgB_2 sheet (see Fig. 4.2). Similarly, Mg can be put inside or outside when constructing these nanotubes, which leads to different curvature energies as shown in Fig. 4.2. For nanotubes derived from the hexagonal MgB_2 sheet, the ones with Mg outside are always energetically favored and have negative curvature energies independent of nanotube diameter or chirality.

As illustrated by the above two systems, negative curvature energy is a common phenomenon in Mg boride nano-materials. We have studied a series of Mg doped boron sheets with hexagonal hole density η ranging from 0 to 1/3 and varied Mg doping concentration. We found that negative curvature energy occurs for Mg doped boron sheets with both small and large η. In addition, we discovered a general trend – negative curvature energy

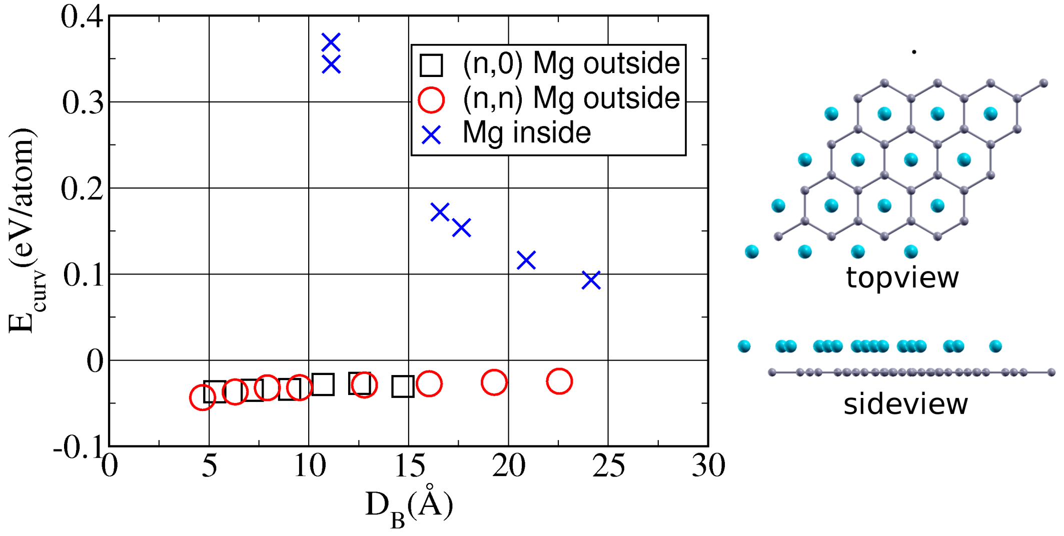

Figure 4.2: (Left) Total energy per atom versus diameter of the constituent boron nanotube for nanotubes made of hexagonal MgB_2 sheet. (Right) Structure of the hexagonal MgB_2 sheet. Large blue balls are Mg, small gray balls are B.

occurs for small-η sheets with Mg atoms inside and for large-η sheets with Mg outside.

Mg on boron sheets

To understand the negative curvature energy in Mg boride nanotubes, we first study their precursors, Mg doped boron sheets. We define the absorption energy per Mg as

$$E_{ab} = (E_B - E_{doped})/N_{Mg} + E_{Mg},$$

where E_{doped} is the energy of Mg doped boron sheet, E_B is the energy of the same boron sheet with Mg removed, N_{Mg} is the number of Mg, and E_{Mg} is the energy of an isolated Mg atom. E_{ab} is positive, and larger E_{ab} means stronger binding of Mg to the boron sheet.

We start with the Mg doped α sheet. First, we checked the convergence of E_{ab} versus the size of the supercell. We calculated E_{ab} for one Mg on an α sheet with different-sized unit cells and found that a 2×2 unit cell converges E_{ab} to 5 meV/Mg. So a 2×2 unit cell is sufficient to isolate a Mg from its periodic copies. Second, we investigated the preferred absorption site for Mg. By computing E_{ab} with Mg placed on high-symmetry points in a 2×2 unit cell, we found that the center of a hexagon is the most stable absorption site with E_{ab}=1.07 eV/Mg and is at least 0.4 eV/Mg more stable than any other sites. In addition,

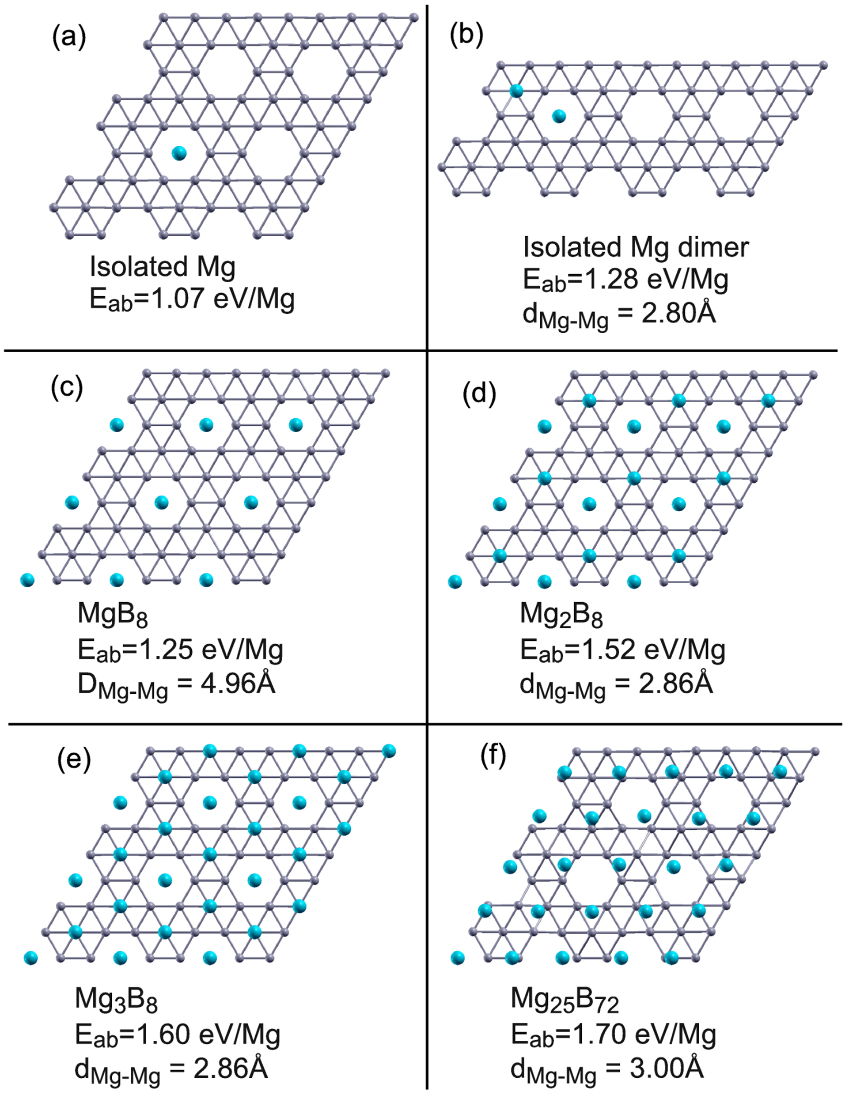

Figure 4.3: Structures, absorption energies, and Mg-Mg bond length for six exemplary configurations of Mg doped α sheet: (a) isolated Mg, (b) Mg dimer, (c) MgB_8, (d) Mg_2B_8, (e) Mg_3B_8, and (f) $Mg_{25}B_{72}$. Large blue balls are Mg, small gray balls are B.

we studied two Mg atoms on an α sheet with a 4×2 unit cell. We searched for the most stable structure over many configurations where the two Mg are placed on various high-symmetry points and on either side of the sheet. We found that two Mg prefer to stay on the same side of the sheet and close to each other, showing that the interaction between two Mg is attractive on the α sheet. The optimal configuration, shown in Fig. 4.3(b), is 0.21 eV/Mg more stable than an isolated Mg on a hexagon center. The distance between two Mg in the optimal configuration is 2.80 Å, which is smaller than the LDA bond length, 3.40 Å, in a Mg dimer [95].

Finally, we investigated 2D meshes of Mg on top of an α sheet. Figure 4.3(c)-(f) show structures of four exemplary systems we studied. The simplest 2D Mg structure on the α sheet (MgB_8) is to put one Mg on every hexagon center, which has E_{ab}=1.25 eV/Mg. When increasing Mg concentration and putting additional Mg on triangular regions, we obtained hexagonal (Mg_2B_8) and triangular (Mg_3B_8) lattices on top of the α sheet. These two configurations have E_{ab} of 1.52 eV/Mg and 1.60 eV/Mg, which are about 0.5 eV/atom larger than isolated Mg. Hence, Mg prefer to attract each other and form 2D lattices on top of an α sheet instead of staying isolated. To find the optimal 2D Mg structure on α sheet with the largest E_{ab}, we have constructed many configurations and searched for the best one. We found that the optimal structure is $Mg_{25}B_{72}$ shown in Fig. 4.3(f). This configuration has the largest E_{ab} we have seen in an Mg-α sheet system, which is 1.70 eV/Mg. Furthermore, the Mg-Mg bond length in $Mg_{25}B_{72}$ is about 3.00 Å, very close to the LDA Mg-Mg bond length of 2.99 Å calculated for a 2D triangular lattice of pure Mg.

On the other hand, Mg on the hexagonal sheet shows very different behavior. Since the hexagonal sheet is unstable by itself, we have kept the boron sublattice fixed and relaxed only the Mg coordinates. We performed similar calculations to those for Mg on the α sheet. We found that the most favored absorption site is still the hexagon center, with a large E_{ab}=3.56 eV/Mg for isolated Mg. In addition, we found that the interaction between Mg is always repulsive and isolated Mg gives the largest E_{ab}.

We have also investigated many other Mg doped boron sheets and have discovered two opposite behaviors for Mg on boron sheets as exemplified by the α and hexagonal sheets, respectively. On boron sheets with $\eta \leq 1/7$, Mg attract each other and form covalent bonds with bond length close to pure Mg structures. On the other hand, on sheets with $\eta \geq 1/6$, the interaction between Mg is always repulsive and isolated Mg is preferred. We explain the underlying mechanism below.

Charge transfer

We have discovered that a simple charge transfer picture can be used to explain the disparate Mg-Mg interactions on the different boron sheets. In Mg-B systems, Mg is expected

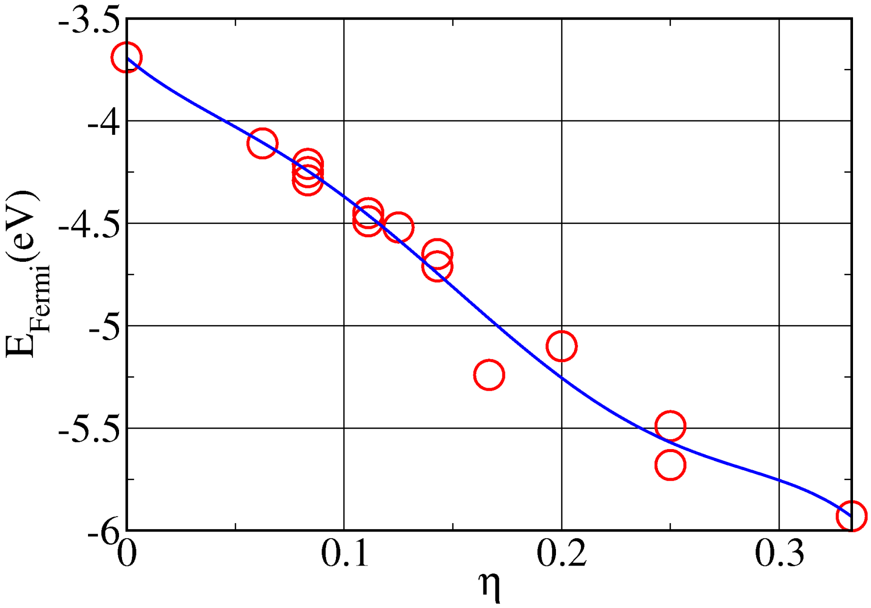

Figure 4.4: Fermi level of boron sheets versus η. Red circles are the DFT calculated data and the blue solid line is a fit.

to donate electrons to the boron sub-system and become positively charged. The amount of charge transfer from Mg to B is driven by the Fermi level difference between Mg and boron sheets. Since the Fermi level of Mg is approximately its $2s$ atomic energy level, the Fermi level difference is determined mainly by the Fermi level of boron sheets. Figure 4.4 shows the Fermi level versus η for boron sheets. We can see that the Fermi level of boron sheets changes more than 2 eV when η goes from 0 to 1/3. Small-η boron sheets have higher Fermi levels than large-η ones. We then expect that Mg will donate fewer electrons to small-η boron sheets and more to large-η ones, which is exactly what we see in our *ab initio* calculations. Figure 4.5 shows the calculated charge transfer from Mg to different boron sheets using two approaches – Löwdin charges [71] and a Wannier function based method [7]. Although different in absolute numbers, both approaches show the same trend that Mg on boron sheets with larger η donates more electrons and is more positively charged.

Hence, the interactions between Mg atoms can be understood in the following way. When doped on boron sheets with small η, Mg atoms donate few electrons to the boron sheets and are close to being neutral, and thus prefer to make covalent bonds with each

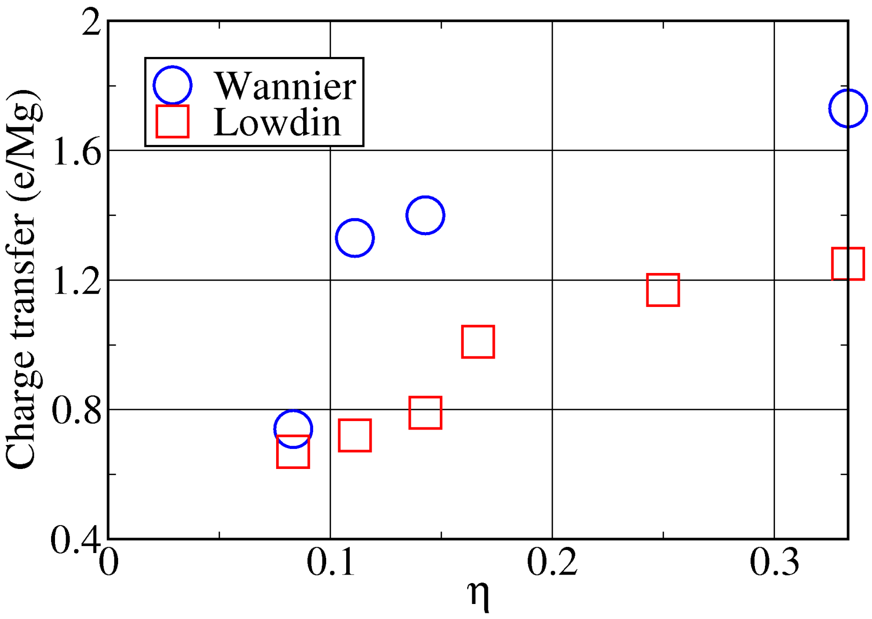

Figure 4.5: Charge transfer from Mg to boron sheets (in e/Mg) calculated using Wannier functions (blue circles) and Löwdin method (red squares)

other much like Mg atoms. On the other hand, on large-η boron sheets, Mg atoms are well ionized with charge states close to Mg^{2+}, and repulsive Coulomb interactions become dominant and make the Mg atoms stay as far away from each other as possible.

Explanation of negative curvature energy

Once we know that the different charge states on Mg atoms determine the Mg-Mg interactions, we can apply this knowledge to explain our discovery of negative curvature energy. When constructing a nanotube from a Mg boride sheet, we change the distance between Mg atoms in addition to curving boron-boron bonds. If the Mg stay outside the nanotube, the distance between Mg and Mg becomes larger with increased curvature, while the Mg-Mg distance decreases if Mg are inside. For nanotubes based on small-η boron sheets, Mg-Mg interactions are attractive and Mg atoms prefer to aggregate and thus prefer to stay inside the nanotube to make covalent bonds. The energy lowering from forming Mg-Mg bonds can overcome the energy cost of bending the boron-boron bonds and can result in negative curvature energy. However, with extreme curvature, Mg-Mg bonds can become shorter than the optimal length, introducing large curvature energy which is what we see in Fig. 4.1. For nanotubes based on large-η boron sheets, Mg-Mg interactions are

Table 4.1: Decomposed energy changes for nanotubes made of Mg doped α sheet, MgB_8. E_{Mg} (in eV/Mg) is the energy changes for Mg nanotubes compared to Mg sheet. E_B (in eV/B_8) is the energy changes for B nanotubes compared to B sheet. E_{sum} is the sum of E_{Mg} and E_B. E_{curv} (in eV/MgB_8) is the overall curvature energy for Mg boride nanotubes.

	E_{Mg}	E_B	E_{sum}	E_{curv}
(6,0)	-0.38	0.37	-0.01	0.00
(8,0)	-0.35	0.22	-0.13	-0.15
(10,0)	-0.25	0.15	-0.10	-0.10
(3,3)	-0.76	0.45	-0.31	-0.30
(4,4)	-0.48	0.26	-0.22	-0.15
(5,5)	-0.30	0.17	-0.13	-0.08
(6,6)	-0.22	0.12	-0.10	-0.04
(8,8)	-0.14	0.07	-0.07	-0.02

repulsive, so Mg atoms prefer to stay away from each other and on the outside. When the energy gain from Coulomb repulsion overcomes the energy to bend boron-boron bonds, we observe negative curvature energy.

To support our explanation, we turn to nanotubes made from the Mg doped α sheet – MgB_8. We focus on nanotubes with Mg inside which have negative curvature energies. According to our theory, negative curvature energy originates from the attractive interaction between Mg. Hence, the curvature energy of a Mg boride nanotube is approximately the sum of the energy gained from Mg interaction and the energy lost to bend boron-boron bonds, assuming that the bonding between Mg and the α sheet does not change much with curvature. To test this, we decompose MgB_8 nanotubes into separate Mg and B nanotubes and the MgB_8 sheet into Mg and B sheets, with their atomic coordinates being the same as the original relaxed configuration. We then calculate energy changes for Mg and B nanotubes relative to their sheet structures and compare the sum of these two energy changes to the curvature energy of the corresponding MgB_8 nanotube. Table 4.1 shows our calculated results. As we can see, the interaction between Mg is indeed the driving force for negative curvature energy, and the sum of energy changes from Mg and B separately explains the total curvature energy quite well.

4.2 Two-dimensional Mg boride sheets

After presenting the peculiar negative curvature energy in Mg boride nanotubes, we now discuss 2D Mg boride sheet structures and their phase diagram which determines the most stable phases. In a 2D Mg boride sheet, Mg atoms donate electrons to boron sheets. With donated electrons from Mg, boron sheets tend to reduce their triangular regions and increase η to keep the optimal filling of bonding states. Larger Mg concentration then results in large η for the constituent boron sheets. For a given ratio of Mg to boron (*i.e.* stoichiometry), the optimal groundstate structure should be searched with respect to boron sheet structures and Mg positions. Given the optimal structures at each stoichiometry, we are able to build the phase diagram and determine the most stable phases and phase coexistence.

We have used a genetic algorithm to search for optimal structures at fixed stoichiometries. To map out the phase diagrams for Mg boride sheets, we choose 17 reasonable stoichiometries and search for the most stable structure at every stoichiometry. By writing the formula of a Mg boride compound as $\mathrm{Mg}_m\mathrm{B}_n$, where m, n are integers, the 17 stoichiometries we investigated are m:n = (1:8, 1:6, 1:5, 1:4, 1:3, 2:5, 1:2, 2:3, 3:4, 1:1, 4:3, 3:2, 2:1, 5:2, 3:1, 4:1, 6:1). In our simulations, we have considered two different constraints on the structures of 2D $\mathrm{Mg}_m\mathrm{B}_n$ sheets: restricting the constituent boron subsystem to be at most a single-layered sheets, or allowing the existence of double-layered boron sheet structures. In this section, we first discuss the 2D $\mathrm{Mg}_m\mathrm{B}_n$ structures with single-layered boron sheets, and then present double-layered boron sheets based Mg boride structures.

4.2.1 Mg borides based on single-layered B sheets

Structures

Using the genetic algorithm, we have determined the most stable sheet structures at each stoichiometry $\mathrm{Mg}_m\mathrm{B}_n$ under the structural constraint that boron sheets are at most single-layered. Here, we discuss the structures of these 2D sheets. Figure 4.6 shows exemplary structures of the most stable Mg boride sheets for eight different stoichiometries. As we can see from the Figure, the MgB_8 structure is based on the most stable single-layered boron sheet - α sheet. When the concentration of Mg increases from MgB_8 to MgB_5

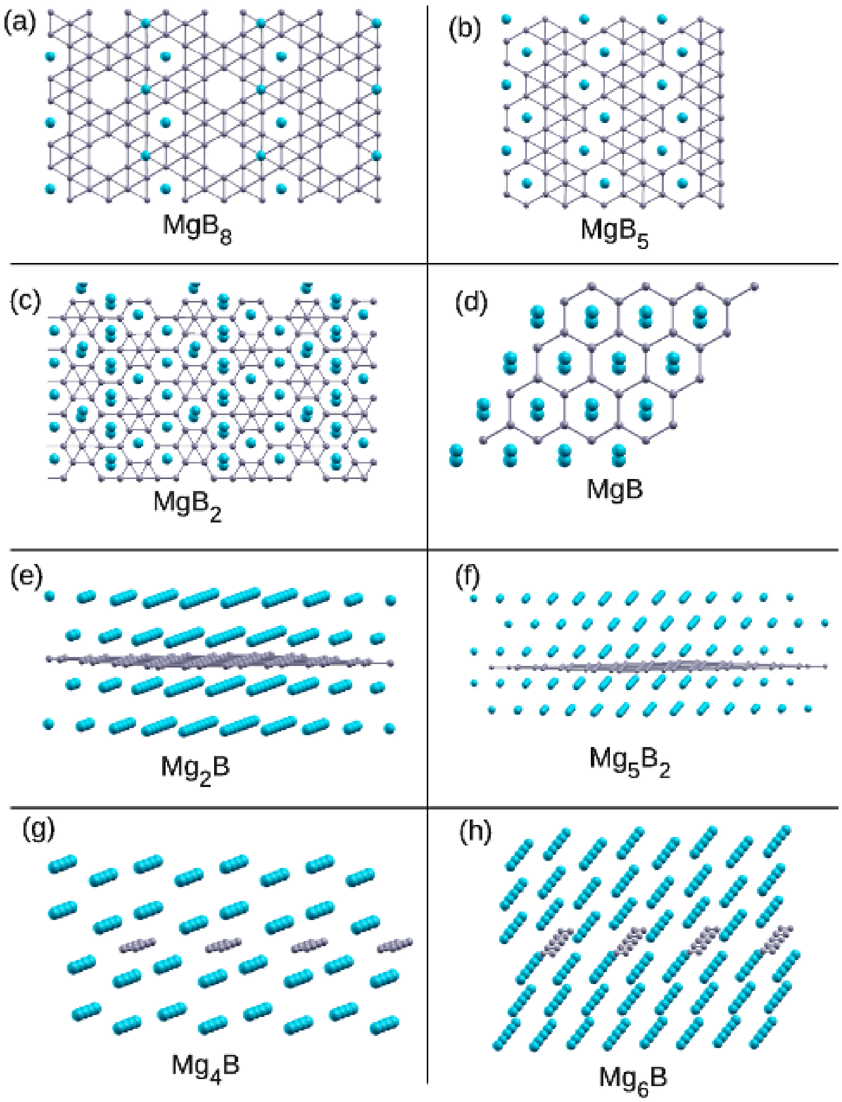

Figure 4.6: Illustration of the most stable Mg boride sheet structures for eight different stoichiometries: (a) MgB_8, (b) MgB_5, (c) MgB_2, (d) MgB, (e) Mg_2B, (f) Mg_5B_2, (g) Mg_4B and (h) Mg_6B. Small gray balls are B and large blue balls are Mg.

and MgB_2, the constituent boron sheets have increased hexagonal regions, or equivalently larger hexagonal hole density η. As soon as the stoichiometry hits m:n=1:1, or MgB, the constituent boron sheet becomes hexagonal, which is the same as the structure of bulk MgB_2. With even larger Mg ratios – Mg_2B and Mg_5B_2, the boron sheet remains hexagonal and additional Mg atoms keep stacking on both sides of the MgB layer in an *hcp*-like manner similar to Mg bulk. When the concentration of Mg gets extremely high,

Mg_4B in our case, the boron subsystem breaks into 1D zigzag lines instead of forming 2D sheets (similar structures of boron have been seen in Li boride bulk [96]) and this trend persists for higher Mg concentration (Mg_6B) with Mg forming bulk-like slabs.

The above observation can be explained through a charge transfer picture, in which Mg atoms donate electrons to the boron subsystems and consequently change the bonding patterns of the boron. As shown in previous sections, pure boron sheets are made of mixtures of triangles and hexagons. The graphitic hexagonal boron sheet is not stable because boron only has three valence electrons instead of four so that large parts of the bonding states are not filled. Adding boron atoms to the hexagonal sheet forms mixtures of hexagonal and triangular motifs and thus improves stability by balancing two-center and three-center bonding. According to the self-doping rule in pure boron sheets, adding a boron atom to the center of a hexagon does not change the number of bonding states but only adds three valence electrons to the system. In other words, we can consider every atom added to a hexagonal center as a perfect electron donor. With a fixed number of bonding states, the most stable α sheet is the structure with the right number of atoms in hexagon centers, which makes all atoms in the hexagonal lattice have 4 electrons each and the α sheet become iso-electronic to graphene.

With the existence of Mg, each Mg atom donates a certain number of electrons to the boron sub-system. In other words, every boron atom now has more than 3 valence electrons. Hence, fewer boron atoms are needed at the hexagon centers to keep the boron subsystem iso-electronic to graphene. As a consequence, the most stable structures with Mg should contain a boron structure that has fewer triangular regions than the α sheet. Furthermore, more hexagonal regions appear as more Mg atoms are added to the system, and this is exactly what we see in Fig. 4.6 from MgB_8 to MgB. When the m:n ratio reaches 1:1, the constituent boron sheet starts to become exactly graphitic, suggesting that this is the point where each B atom now has approximately 4 electrons . After the m:n ratio exceeds 1:1 and Mg becomes more numerous than B, each B atom would have more than 4 electrons, which would fill anti-bonding states which challenges the stability of the graphitic boron structure. But only after the m:n reaches 4:1 does the graphitic boron structure break and the zigzag lines of boron are formed with quite similar boron structures to Li

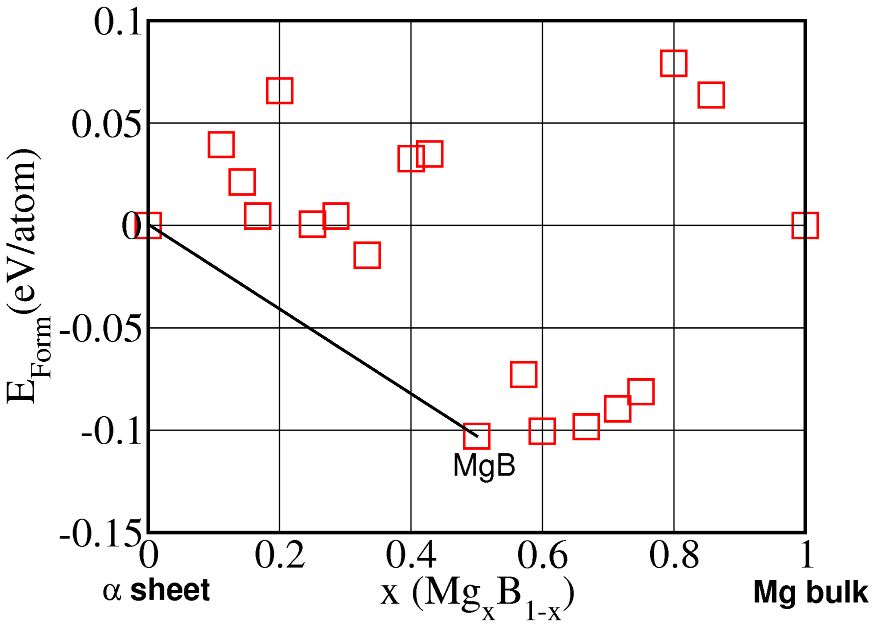

Figure 4.7: Phase diagram of 2D Mg boride structures based on single-layered boron sheets: formation energies versus Mg concentration x. Red squares are DFT calculated data with LDA. The black solid coexistence line connects the α sheet and the most stable phase MgB for boron rich environments ($x \leq 1$).

boride bulk [96]. Lines of boron form because each boron has more than 4 electrons and thus prefers to lower its coordination. One can imagine the extreme scenario where each boron atom has 8 electrons and the boron atoms would not bind to each other at all.

Phase diagram

After calculating the total energies of the most stable structures for all the 17 stoichiometries we have considered, we are now ready to construct the phase diagram for 2D Mg boride sheets and determine the most stable phase. Using the pure boron α sheet and Mg bulk as the two reference systems, we define the formation energy of a $\mathrm{Mg}_m\mathrm{B}_n$ or $\mathrm{Mg}_x\mathrm{B}_{1-x}$ $[x = m/(m+n)]$ structure as

$$E_{Form} = E_{Mg_xB_{1-x}} - (1-x)E_\alpha - xE_{Mg}, \tag{4.1}$$

where $E_{Mg_xB_{1-x}}$ is the energy per atom of the structure $\mathrm{Mg}_x\mathrm{B}_{1-x}$, E_α is the energy per atom of the α sheet, and E_{Mg} is the energy per atom of bulk Mg.

Figure 4.7 shows our calculated phase diagram, which is formation energy E_{Form} versus

Mg concentration x for Mg boride sheets based on single-layered boron structures. For small x with $x < 1/2$, most structures are above the $E_{Form} = 0$ line connecting the α sheet to Mg bulk, except for MgB_2 with x=1/3 which is slightly below this line. This means that, for small Mg concentrations, Mg boride sheets are not very stable with respect to the two references. At x=1/2 the MgB sheet (see Fig. 4.6), which is based on a graphitic boron sheet, is 0.11 eV below the $E_{Form} = 0$ line, showing that MgB is a stable phase. For x larger than 1/2 and smaller than 0.8, all stable structures are constructed from the MgB sheet by stacking Mg on both sides of the MgB sheet in an *hcp* manner. These structures are about 0.07-0.1 eV below the $E_{Form} = 0$ line and are also stable. When x gets close to 1, the Mg boride structures are based on zigzag boron lines which are above the $E_{Form} = 0$ line and unstable. Hence, we can see that, compared to the α sheet and bulk Mg, stable Mg boride sheets occur around x=1/2.

Given the experimental situation where Mg boride nanostructures are fabricated by doping pure boron nanotubes with a small amount of Mg [14], we are interested in the most stable phases under boron rich environments, and we focus on the phase diagram for $x \leq 1/2$. As shown in Fig. 4.7, for $x \leq 1/2$ a straight line connecting α sheet and MgB at x=1/2 has all other structures lying above it. Hence, MgB is the most stable structure indicated by our phase diagram. In other words, if we only consider 2D flat sheet structures based on at most single-layered boron sheets and neglect any possible curvature effects, doping single-walled boron nanotubes with Mg will result in coexistence of the α sheet and the MgB structure once the whole system reaches equilibrium; no other structures would occur.

4.2.2 Mg borides based on double-layered B sheets

Structures

In the previous section, we have discussed the structures and phase diagram for 2D Mg boride structures based on single-layered boron sheets. Because the most stable double-layered boron sheet, double-Z(1/12), is more stable than the optimal single-layered α sheet, in principle 2D Mg boride structures based on double-layered boron sheets should be more stable than those with single-layered boron sheets. In this section, we relax our constraints on the configurations of the boron sub-system and allow the occurrence of 2D Mg boride

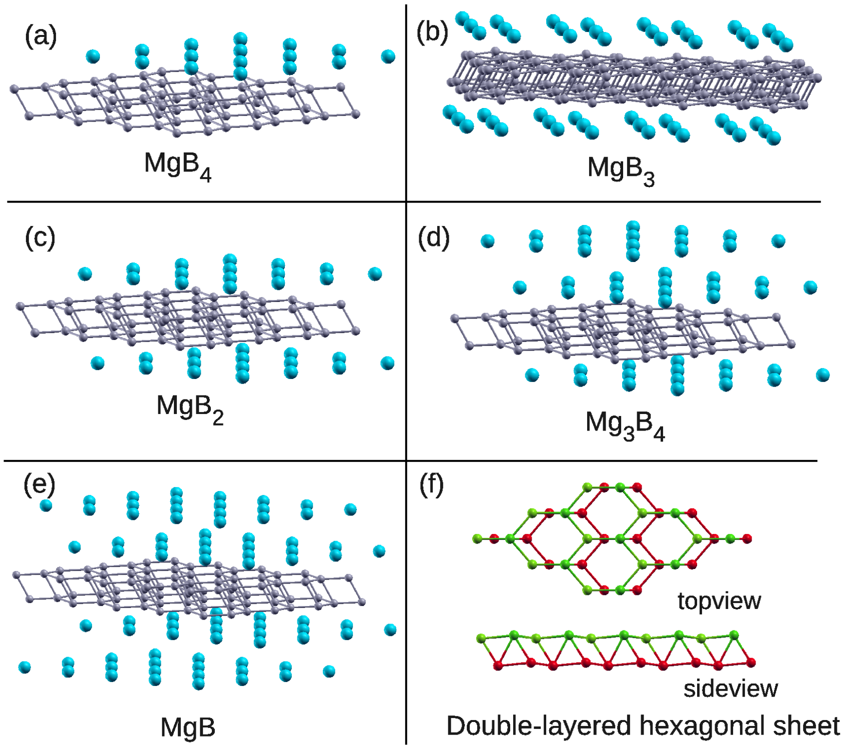

Figure 4.8: (a)-(e) Illustrations of the most stable Mg boride structures based on double-layered hexagonal boron sheets for five stoichiometries. Small gray balls are B and large blue balls are Mg. (f) Structure of double-layered hexagonal boron sheet. The upper layer of the boron sheet is shown as green balls and the lower layer is in red.

structures with double-layered boron sheets.

With the new structural constraint, we have re-run the genetic algorithm calculations and searched for more stable structures. As a result, we discovered more stable structures at five stoichiometries, which are MgB_4, MgB_3, MgB_2, Mg_3B_4 and MgB. Figure 4.8(a)-(e) show their structures. As we can see, all five structures are based on the same double-layered hexagonal boron sheet [shown in Figure 4.8(f)] with different Mg coverages. The double-layered hexagonal boron sheet is constructed by stacking two single-layered hexagonal sheets on top of each other with one sliding slightly along the in-plane B-B bond. As a result, all the hexagons are slightly distorted.

Other than the five double-layered structures shown in Fig. 4.8, we have not observed any double-layered structures at other stoichiometries. For structures with large Mg concentrations ($x > 1/2$), this is probably because double-layered structures are not as stable as the single-layered structures we discussed in Sec. 4.2.1 for these stoichiometries: each boron has more than 4 electrons such that boron prefers to form low-coordinated structures. On the other hand, for $x < 1/2$, it might be possible to find more stable structures based on the double-layered hexagonal boron sheet, but this would require us to do much larger searches and use significantly more computational time and resources.

Phase diagram

We construct a new phase diagram that includes the more stable double-layered structures found at MgB_4, MgB_3, MgB_2, Mg_3B_4 and MgB. For other stoichiometries, we use the same single-layered structures as in Fig. 4.7. To be compatible with the double-layered boron sheets based Mg boride structures, we now use the optimal double-layered boron sheet, double-Z(1/12), as the reference system for pure boron instead of the α sheet; we still use Mg bulk as the other reference system. The formation energies of all structures are recalculated with respect to the new references.

Figure 4.9 shows the formation energies E_{Form} versus x. We connect MgB_4, MgB_3, MgB_2, Mg_3B_4 and MgB with linear lines to get the linear interpolated formation energies for those structures based on the double-layered hexagonal boron sheet with Mg concentrations between these five stoichiometries. We can see that structures with small x and large x are unstable with respect to the two references and all stable structures occur around x=1/2. Similar to what we have done in Sec. 4.2.1, for the $x \leq 1/2$ region lines connecting structures at x=0, 1/3, 3/7 and 1/2 have all other structures lying above the lines as shown in Fig. 4.9. Hence, the double-layered boron sheet, MgB_2, Mg_3B_4 and MgB are stable structures under boron-rich environments and can coexist with the double-Z(1/12) sheet. In addition, all structures based on the double-layered hexagonal boron sheet with x between 1/3 and 1/2 should also be stable.

4.2.3 Discussion

We have described the structures of 2D Mg boride sheets and their phase diagram under two different structural constraints which allows at most single-layered or double-layered boron sheets. One can image that, if we relax the constraint even more, more stable "2D" structures will show up, and if we do not impose any restriction on the structures, the

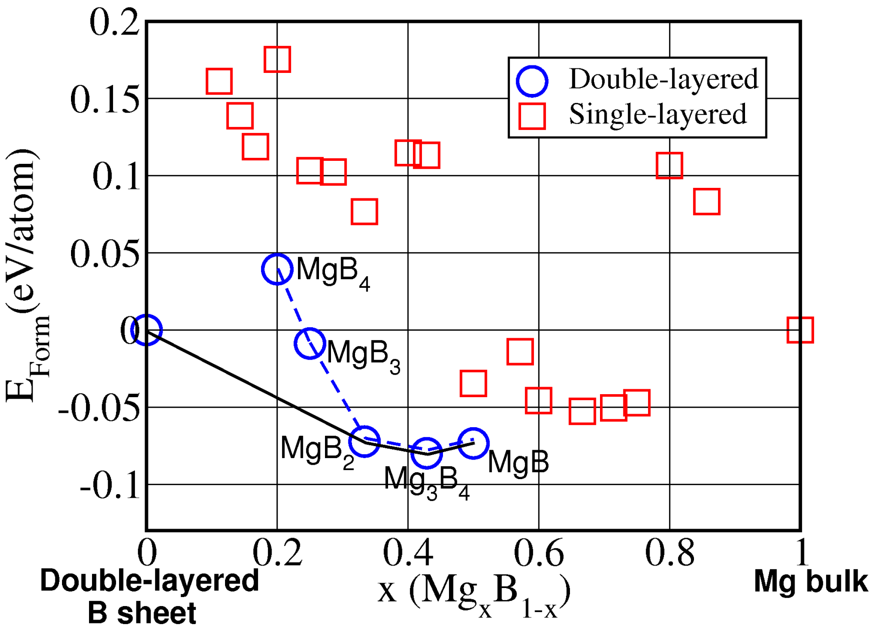

Figure 4.9: Phase diagram of 2D Mg boride sheets including double-layered boron sheet based structures: formation energies versus Mg concentration x. Blue circles are DFT calculated data for double-layered boron sheet based structures and red squares show calculated formation energies for single-layered boron sheet based structures. The blue dashed lines connecting MgB_4, MgB_3, MgB_2, Mg_3B_4 and MgB account for structures based on the double-layered hexagonal boron sheet with x between 1/5 and 1/2. The black solid lines connecting structures at $x = 0$, 1/3, 3/7 and 1/2 denote stable phases at equilibrium.

most stable phase should be the bulk MgB_2 structure. So we must carefully define the very question we are trying to answer. Here, we are trying to address the problem of what are the likely geometries of the Mg boride nanostructures (presumably nanotubes) fabricated in experiments. Thus we should first investigate the 2D flat sheets which are the precursors of Mg boride nanotubes. For 2D flat Mg boride sheets, we should focus on those stable 2D structures that are relatively easy to curve into nanotubes. Therefore, structures based on single-layered boron sheets should have small curvature energies and are the first objects to study. Structures based on double-layered boron sheets are more stable but also are more difficult to curve, but the curvature energies might not be too large. On the other hand, structures based on three or more layers of boron will be formidable to curve and are out of the scope of this preliminary investigation.

4.3 Mg boride nanotubes

In the previous section, we have discussed the phase diagrams of 2D flat Mg boride sheets under structural constraints. For Mg boride nanotubes with very large diameters, their stable structures and phase diagrams should be similar to those of 2D structures since curvature effects will be small. However, the story can be different for small-diameter Mg boride nanotubes. In this section, we show how the phase diagram changes with curvature when 2D Mg boride sheets are curved into 1D nanotubes.

From the previous section, we know that sheet structures based on double-layered boron can be more stable than those based on single-layered boron. However, when considering nanotubes, curvature could play an important role in determine the energetic order, especially for small diameters and large curvature. Since the ionic bonds between Mg and B should not be very angle-dependent and should not change much when going from sheets to nanotubes, the curvature energy comes mostly from the bond bending in the boron sub-system and changes in Mg-Mg interactions. As we have shown in Section 4.1, changes in Mg-Mg interactions can results in negative curvature energy in Mg boride nanotubes. In addition, similar to single-walled and double-walled carbon nanotubes, Mg boride sheets with double-layered boron sheets are much more difficult to curve. Due to the above two factors, we expect that curvature plays an important role in determining the phase diagrams of Mg boride nanostructures, especially when nanotube diameters reach small values.

4.3.1 Curvature energy of stable two-dimensional phases

Before discussing the effect of curvature on the phase diagram of Mg boride nanostructures, we first investigate the curvature energies of two stable phases under two different structural constraints: the single-layered MgB sheet (shown in Fig. 4.6) and the double-layered MgB_2 sheet (shown in Fig. 4.8).

Figure 4.10 shows the curvature energies versus diameter of the constituent boron nanotubes for the single-layered MgB sheet. The curvature energies turn out to be dependent on both nanotube diameter and chirality. The (n,n)-type nanotubes have smaller curvature energies than the $(n,0)$-type for given nanotube diameters. By fitting the curvature

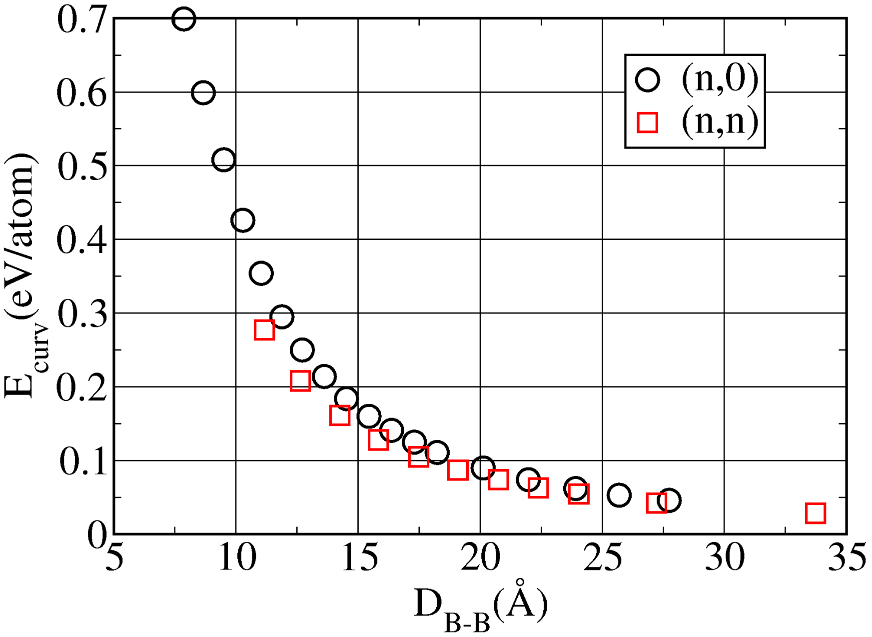

Figure 4.10: Curvature energies versus nanotube diameters for both (n,0) and (n, n) type nanotubes made from the hexagonal MgB sheet.

energy versus diameter with $1/D^2$, we obtain

$$E_{curv} = C_1/D^2, C_1 = 34.54 \text{ eV}\text{Å}^2 \tag{4.2}$$

for (n,n)-type and

$$E_{curv} = C_2/D^2, C_2 = 45.18 \text{ eV}\text{Å}^2 \tag{4.3}$$

for (n,0) type. Comparing these to the corresponding values for single-walled boron nanotubes made of α sheet, we can see that the curvature energies for this MgB sheet is about one order of magnitude larger. We believe that the large energy cost to curve the sheet comes from the fact that Mg atoms are extremely ionized and it costs large energies to place Mg atoms inside nanotubes.

For the double-layered MgB_2 sheet, we had expected that its curvature energy would be larger than the single-layered MgB sheet because the covalently bonded double-layered hexagonal boron sheet is harder to curve (in addition to the fact that Mg atoms do not prefer to stay inside nanotubes). We show the curvature energy versus average diameter of

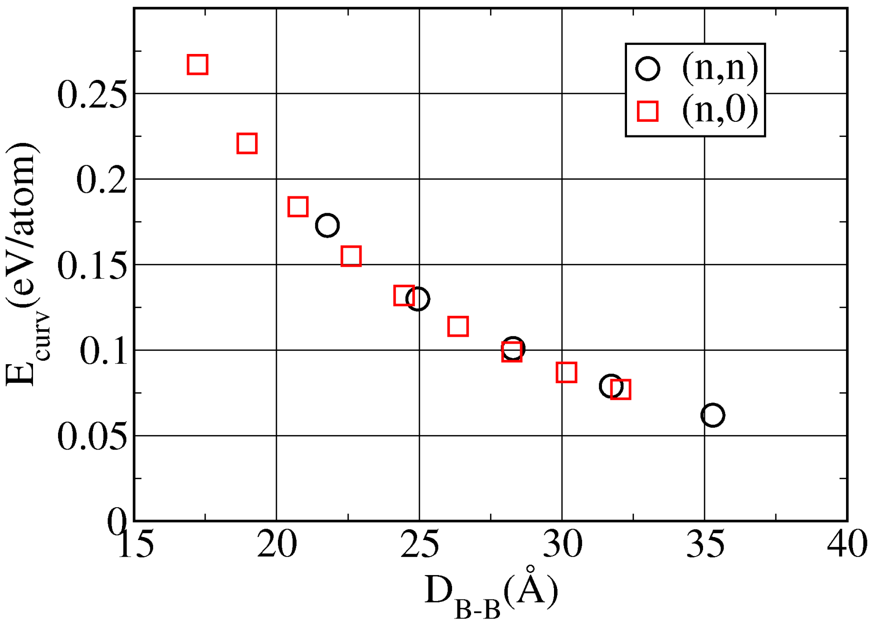

Figure 4.11: Curvature energies versus average nanotube diameters for both (n,0) and (n, n) type nanotubes made from the MgB_2 sheet based on double-layered hexagonal structures.

constituent boron nanotubes for the MgB_2 sheet in Fig. 4.11. The curvature energy is also slightly chiral dependent with the (n,0)-type nanotubes having slightly smaller curvature energies. Fitting E_{curv} versus D with $1/D^2$ results in

$$E_{curv} = C_3/D^2, C_3 = 81.04 \text{ eVÅ}^2 \tag{4.4}$$

for (n,n)-type and

$$E_{curv} = C_4/D^2, C_4 = 79.44 \text{ eVÅ}^2 \tag{4.5}$$

for (n,0)-type. These values are about twice what we have for the MgB sheet.

These large curvature energies for the two stable phases of 2D Mg boride sheets suggest that curvature is important for the phase diagrams of Mg boride nanotubes with small diameters. When diameters are small, the original stable phases for 2D structures could become unstable due to large curvature energies, and some other structures with small or even negative curvature energies may become more favorable. Consequently, it is necessary to take into account curvature effects when building phase diagrams for Mg boride nanostructures.

4.3.2 Curvature effects on phase diagrams

In the previous section, we have discovered that large curvature energies exist for the two stable phases of 2D Mg boride sheets. In addition, many Mg boride nanotubes have negative curvature energies. Due to these findings, investigation of curvature effects on phase diagrams of Mg boride nanotubes becomes indispensable.

Single-layered structures

First, we consider Mg boride nanotubes based on single-layered boron structures. We have constructed nanotubes from the 10 representative 2D Mg boride sheets in Fig. 4.7 which are the most stable structures at 10 corresponding stoichiometries. We studied the dependence of their total energies on the (average) diameters of the constituent boron nanotubes. Here we set up the phase diagrams for Mg boride nanotubes with various fixed nanotube diameters. For a given nanotube diameter, we use the single-walled boron nanotube made of α sheet with the same diameter as the reference for pure boron and Mg bulk as the other reference for pure Mg, and calculate the formation energies of Mg boride nanotubes with respect to these two references.

Figure 4.12 shows the phase diagrams for three different diameters, D=10Å, 15Å and 20 Å. For D=10Å and 15Å, the only stable phase is MgB_5, whose 2D sheet structure is shown in Fig. 4.6. When the diameter exceeds 15 Å and reaches 20 Å, both phases, MgB_5 and MgB, are stable with respect to the two reference systems. MgB_5 is just above the line connecting pure boron and MgB, meaning MgB becomes slightly more stable than MgB_5 when D=20Å. Considering that MgB is the most stable phase for 2D flat sheets, D=20Å should be the transitional diameter for the most stable phase to change from MgB_5 to MgB. Therefore, if we constrain all structures to be based on single-walled boron nanotubes, MgB_5 is the most stable phase for $D < 20$ Å and MgB is the optimal phase for $D > 20$ Å.

Double-layered structures

Once we relax our constraints to include structures based on double-layered boron sheets, or equivalently double-walled boron nanotubes, we expect more drastic changes in the phase

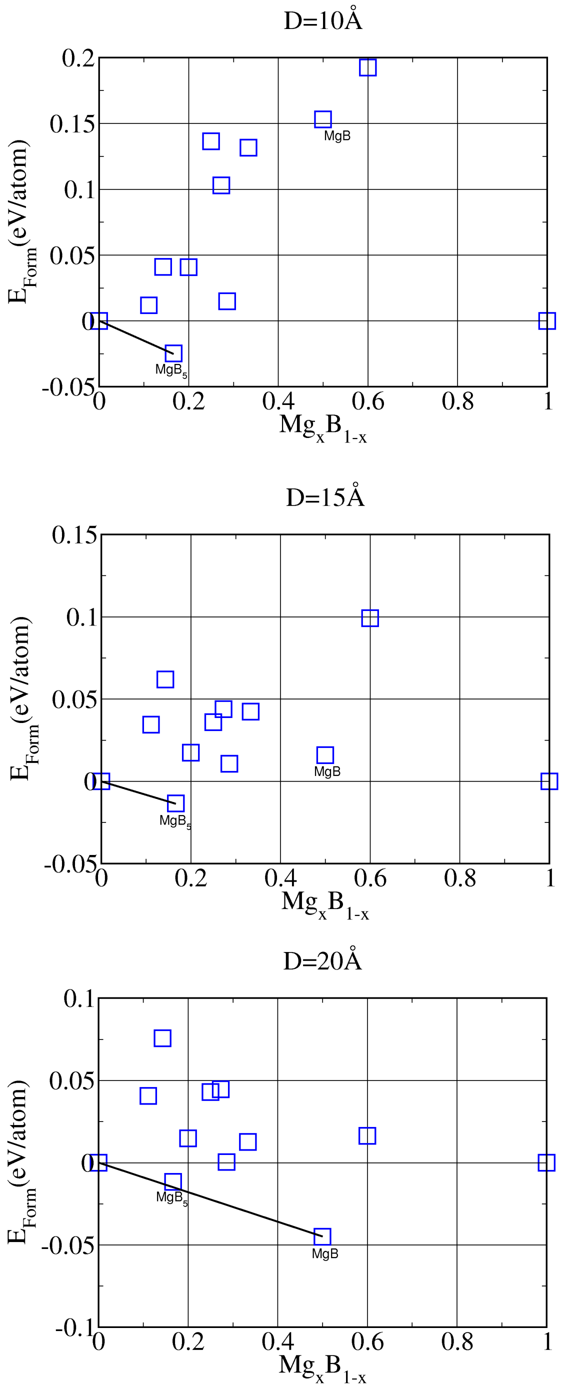

Figure 4.12: Phase diagram for Mg boride nanotubes based on Mg doped single-layered boron sheets with three different diameters: 10 Å, 15Å and 20Å. Blue squares are calculated data. The two references are single-walled boron nanotubes based on the α sheet and Mg bulk.

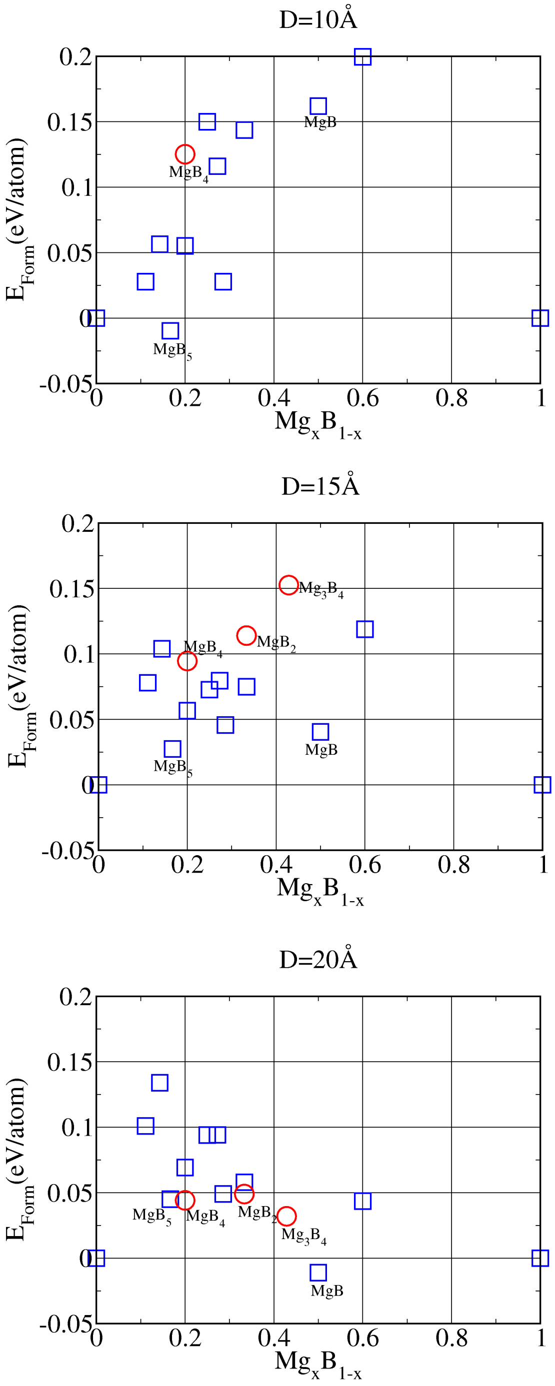

Figure 4.13: Phase diagram for Mg boride nanotubes based on single-layered and double-layered boron sheets with three different diameters: 10 Å, 15Å and 20Å. Blue squares are single-layered structures and red circles are double-layered. The two references are double-walled boron nanotubes based on α sheet and Mg bulk.

diagram due to curvature. Similar to the previous section, we have calculated the phase diagrams for three different nanotube diameters. Here we use the most stable double-walled boron nanotubes [8] as the reference for pure boron and Mg bulk as the other reference. We have included nanotubes made of three Mg boride sheets based on the double-layered hexagonal sheet including MgB_4, MgB_2, and Mg_3B_4 (structures shown in Fig. 4.8). We do not include the double-layered MgB structure because it has extremely large curvature energies due to layers of Mg atoms on both sides of the double-layered hexagonal boron sheet such that it is always less stable than the MgB structure based on single-layered hexagonal sheet for $D < 40$ Å.

Figure 4.13 shows phase diagrams for three nanotube diameters including all structures discussed in Sec. 4.3.2 and nanotubes made of the three double-layered sheet structures. For D=10Å, nanotubes made of double-layered MgB_2 and Mg_3B_4 sheets are unstable and collapse, and nanotubes made of double-layered MgB_4 are less stable than the single-layered counterpart. The most stable phase is MgB_5 based on single-layered boron sheets whose precursor sheet is shown in Fig. 4.6. When D=15Å, no structures are stable with respect to the two reference systems. No Mg boride nanostructures will exist in principle. As D goes to 20 Å, MgB becomes the only stable structure whose formation energy is only slight below zero. Therefore, at very small diameters with $D < 20$ Å, The only two stable phases are MgB_5 and MgB, both of which are based on single-layered boron sheets.

Discussion

In this section, we have studied how curvature changes the phase diagrams of Mg boride nanostructures. Our starting points are the most stable stable 2D sheet structures found using genetic algorithm. All nanotube structures we considered are based on these sheet structures. Apparently such analysis may overlook some important structures which are not very stable as sheets but have small or even negative curvature energies. To deal with this problem in the right way, we should follow a similar procedure to what we have done for 2D sheet structures – to search for the best nanotube structures at given stoichiometry and diameter using a genetic algorithm and to build the phase diagrams based on these best nanotube structures. We have proposed a method to adapt genetic algorithms to studying nanotubes which is described in Appendix A. We have done tests on this method and some promising results have been obtained. We expect further investigation on this topic in the future.

4.4 Summary

We have presented structures and phase diagrams for Mg boride nanostructures including 2D sheets and nanotubes. First, we show that negative curvature energy exists for certain Mg boride nanotubes which is caused by the interactions between Mg atoms. Depending on the structure of the boron sheets, Mg can have different charge states, resulting in distinct interactions between Mg atoms. When curving Mg doped boron sheets into nanotubes, curvature changes the distance between Mg and hence the interaction strength. Once energy gain from Mg-Mg interactions overcomes energy loss from bending covalent boron bonds, we can observe negative curvature energy. This phenomenon has not been seen in other nanotube systems and might be important for the growth of Mg boride nanotubes. Second, we present the most stable Mg boride sheet structures for various stoichiometries with two different structural constraints. Based on these structures, we construct the phase diagram and predict the stable phases under boron-rich environment. When considering only structures based on single-layered boron sheets, the stable phase is a MgB sheet which is composed of a hexagonal boron lattice. Once we including Mg boride structures with double-layered boron sheets, several phases based on a double-layered hexagonal sheet can coexist. These results on 2D sheet structures should also hold for Mg boride nanotubes with large enough diameters and small curvature effects. Finally, we consider curvature effects on the stability of Mg boride nanotubes and how their phase diagrams change with curvature. When nanotube diameters are smaller than 20 Å, Mg boride nanotubes based on single-walled boron nanotubes are generally preferable due to smaller or even negative curvature energies. Our present research on Mg boride nanotubes is not complete enough to definitively predict stable phases with large curvature, and a genetic algorithm based investigation is in progress.

Chapter 5

Boron crystals with layered structures

All boron crystals that exist at ambient conditions have complex structures based on B_{12} icosahedra. The simplest boron crystal, α rhombohedral boron, is made of equivalent interconnected B_{12} icosahedra [2, 3, 4, 97]. Another stable phase of boron, β rhombohedral boron, which is close in energy to α rhombohedral boron, is based on a B_{105} lattice with additional sites partially filled with boron atoms, averaging 106.67 atoms in a rhombohedral unit cell [4, 5, 97]. With the discovery of superconductivity in compressed boron crystals at pressures about 160 GPa [98], much work has been dedicated to exploring novel boron phases under high pressure. Recently a new high-pressure boron phase, γ boron, was fabricated experimentally and verified by first principles calculations [99, 100]. This new boron crystal consists of B_{12} icosahedra and B_2 dimers which act as electron acceptors and donors, respectively, thus showing some ionic behavior. However, this new phase is semiconducting and cannot become superconducting. To search for possible superconducting phases, researchers have focused on metallic boron structures including α-Ga, fcc and bcc. α-Ga boron is stable when pressure is larger than 100 GPa but has small density-of-states around the Fermi level [101]. Fcc and bcc phases have large DOS around the Fermi levels but are only stable under pressures larger than 200 GPa [102]. Obviously, further study is needed to clarify the phase diagram of boron under high pressure. We note that graphite, a layered carbon crystal, can be built directly from stacking graphene sheets. With the

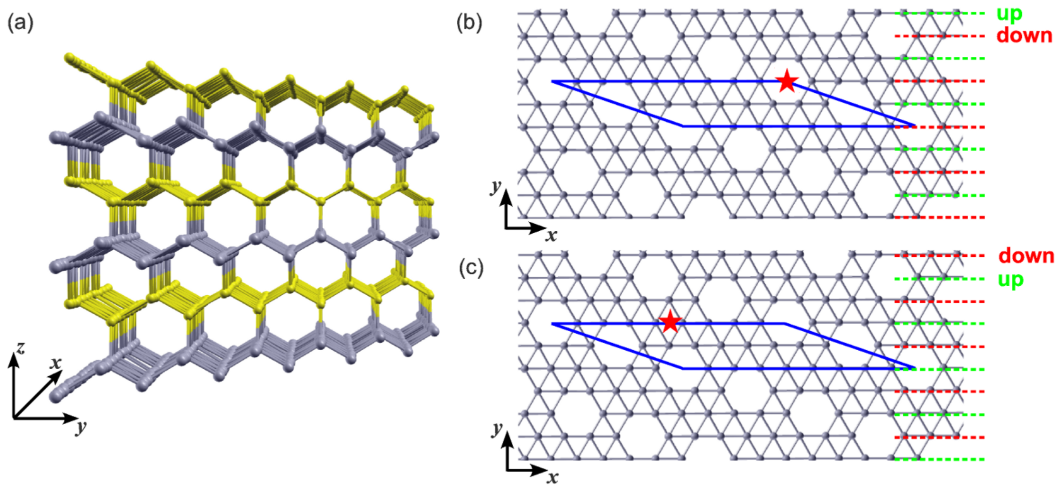

Figure 5.1: (a) Structure of the most stable layered boron crystal in our library. Two inequivalent layers in a unit cell are shown in different colors to guide the eyes. (b) and (c) Structures of constituent boron sheets in two inequivalent layers. Blue solid lines show the unit cell of the sheet. Green (light) dashed lines mark the line of atoms moving up and red (dark) dashed lines mark the line of atoms moving down. When packed to form a crystal, one layer is shifted along the x direction to make the two stars match in the x-y plane.

discovery of stable 2D boron sheets [6], an interesting question can be raised for boron crystals – are there any stable boron crystal structures which are based on sheet structures? In this chapter, I present boron crystals with layered structures and compare their stability with other boron crystalline phases under pressure. All calculations are performed using the PWSCF code [103, 104] and the LDA [58] for exchange and correlation.

5.1 Structure and energy

Unlike graphene and graphite for carbon, boron sheets are significantly (~ 0.5 eV/atom) less stable than α rhombohedral boron. To construct stable boron crystals from boron sheets, it is essential to choose the optimal alignment between different layers of boron sheets such that stabilizing interlayer bonds can form. We have discovered that, in layered boron crystal structures, interlayer bonds are multi-center-like, which are different from the two-center-like interlayer bonds in double-layered boron sheets.

We build layered boron crystals by stacking copies of a boron sheet along the z direction (perpendicular to the sheet plane). We optimize structures by varying the boron sheets and

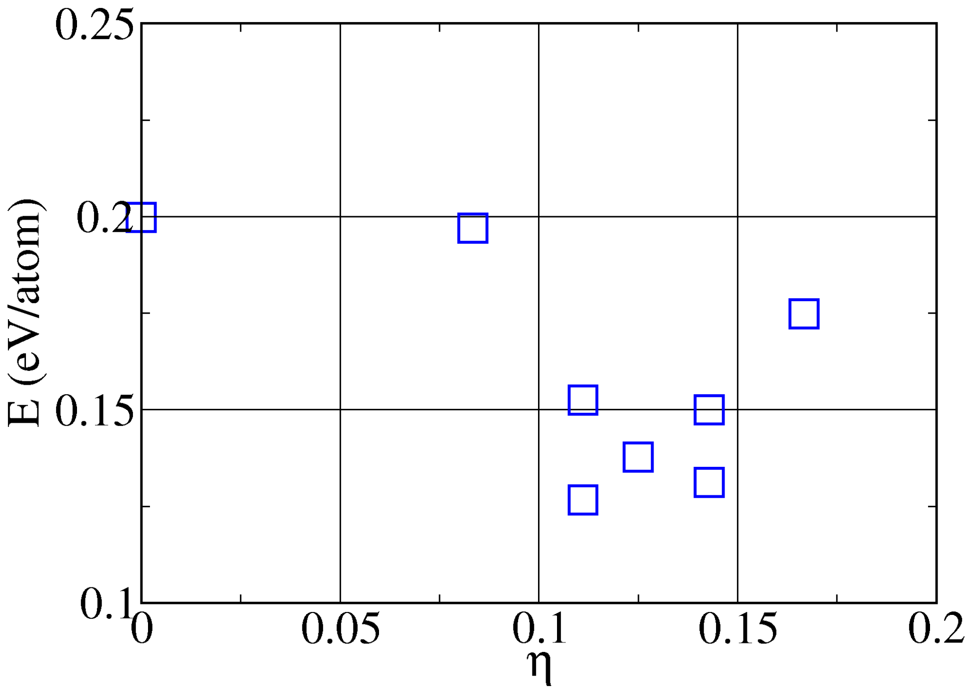

Figure 5.2: Total energy in eV/atom relative to α rhombohedral boron versus η for layered boron crystals built on two-dimensional boron sheets.

their relative alignment. Figure 5.1 shows the most stable layered boron crystal structure in our library, built from a boron sheet with η=1/9 which has a slightly different hexagon arrangement from the α sheet. For this layered structure, a primitive unit cell consists of two inequivalent layers which are buckled with lines of boron atoms moving alternatively up and down along the z direction (similar to the buckling in the buckled triangular sheet [36, 38, 39]). The buckling configurations of two layers are exactly out-of-phase such that atoms moving down in the upper layer can meet atoms moving up in the lower layer forming bonds and *vice versa*. In addition, to make efficient bonding between layers, the two layers of boron sheets are not exactly matched in the x-y plane, but the upper layer is shifted along the x direction by half a lattice vector. Compared to the case that two layers are exactly matched in the x-y plane, the total energy is lowered by about 0.1 eV/atom.

Using the same procedure, we have constructed other layered boron crystal structures based on boron sheets with different η values. Similar to boron sheets, the stability changes with η. Figure 5.2 shows calculated total energy versus η for layered boron crystals. These layered structures are about 0.1-0.2 eV/atom less stable than the α rhombohedral boron.

The optimal structure in our library occurs at η=1/9 which is shown in Figure 5.1 and a structure with η=1/7 is only 0.01 eV/atom less stable. The energy variance versus η for these layered crystals is ~0.07 eV/atom for $0 < \eta < 0.2$, which is smaller than the corresponding value for boron sheets.

5.2 Stability under high pressure

From the previous section, we have learned that boron crystals built based on sheet structures are not as stable as α rhombohedral boron under ambient conditions. However, these layered boron crystals have smaller average volume per atom than α rhombohedral boron, which suggests that layered boron structures may become more favorable under high pressure. In this section, we study the relative stability of our most stable layered boron structure with respect to α rhombohedral boron under high pressure. In addition, we compare our layered structures with two stable high-pressure boron phase, γ boron and α-Ga boron, which are preferred phases under the experimentally reasonable pressure range ($P \leq$ 200GPa) as shown in previous work [99, 100, 101].

Figure 5.3 shows the calculated enthalpy for layered boron, γ boron and α-Ga boron relative to α rhombohedral boron under different external pressures ranging from 0 to 150 GPa. As we can see, the α rhombohedral boron is the most stable phase at zero pressure. γ boron is only 0.03 eV/atom less stable, while layered boron and α-Ga boron are less stable by 0.13 and 0.26 eV/atom, respectively. As pressure increases, all three phase become more stable with respect to α rhombohedral boron. When pressure reaches 20 GPa, γ boron becomes optimal and it remains as the most stable phase for pressure less than 80 GPa. Around 80 GPa, three phases become very close in enthalpy and are approximately degenerate showing possible coexistence of these three. This approximate degeneracy in enthalpy remains for pressures between 80 and 110 GPa. Eventually, α-Ga boron is the most stable structure for pressures larger than 110 GPa.

When comparing the stability of these four boron phases, we have neglected temperature effects by assuming that vibrational entropy and configurational entropy are approximately the same for different boron phases. However, boron crystals are usually fabricated at very high temperature around 2000-3000K and hence the entropy effect can play an

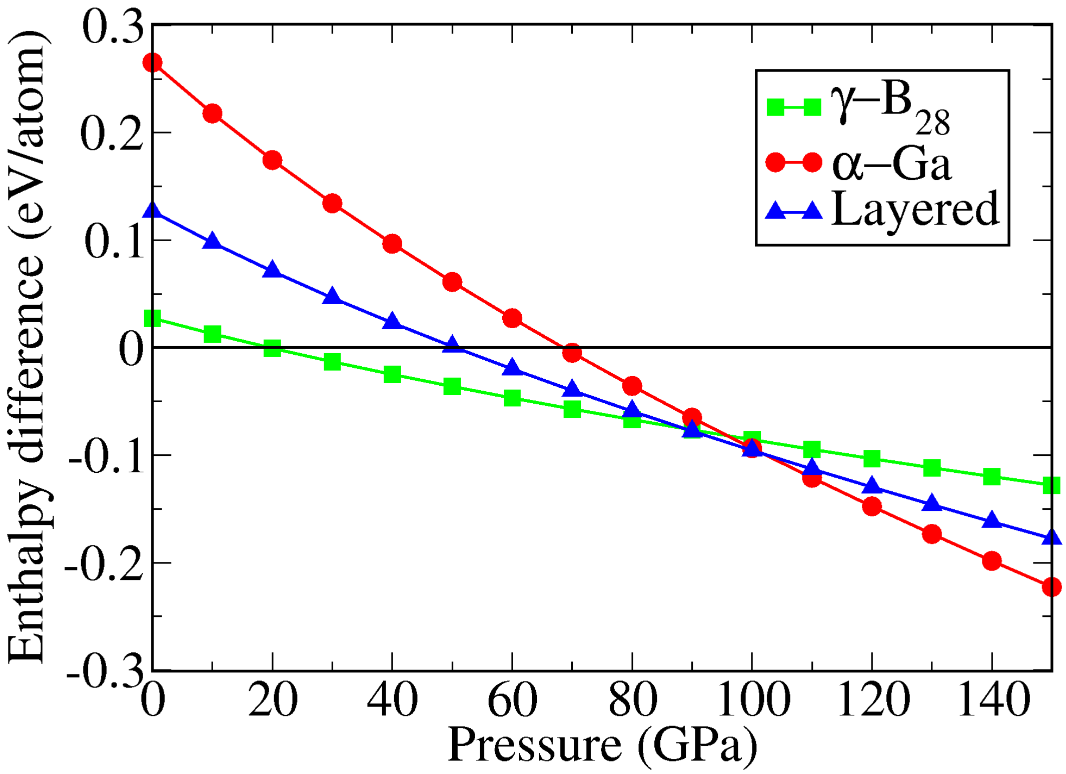

Figure 5.3: Enthalpy of three boron crystals relative to α rhombohedral boron for pressure ranging from 0 to 150 GPa: γ boron (green squares), α-Ga boron (red circles) and layered boron (blue triangles).

important role. For instance, β rhombohedral boron is less stable than α rhombohedral boron based only on total energy, but it becomes more stable than α rhombohedral boron when one accounts for vibrational entropy effects, in agreement with experiments [4, 97]. In our case, three boron phases become almost degenerate for pressures between 80 and 110 GPa, and entropy could be an important factor determining their relative stability and should be further investigated. In particular, because layered boron structures have much freedom in their construction (varying sheet structures and alignment between different layers) which generate structures with very close energies, configurational entropy along with high temperature could contribute to their stability.

Finally, I compare the DOS of the four boron crystals. Figure 5.4 shows the density of states for the most stable layered boron structure along with the three other boron phases. This layered boron crystal is metallic and its DOS around the Fermi level is ~0.1

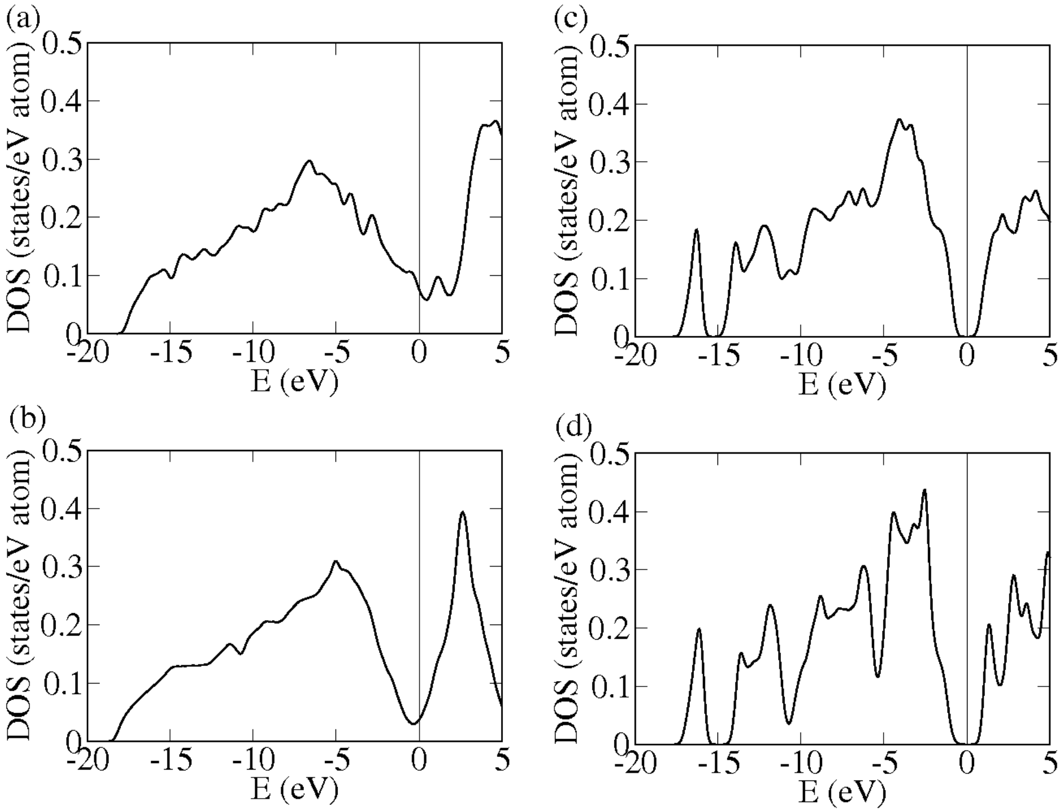

Figure 5.4: Densities-of-states for four boron crystals: (a) most stable layered boron, (b) α-Ga boron, (c) γ boron and (d) α rhombohedral boron. Densities-of-states are in states/(eV atom). Fermi levels are at zero for all plots.

states/(eV atom). γ boron and α rhombohedral boron are semiconducting. In addition, α-Ga boron is metallic but with a small DOS around the Fermi level of ~0.04 states/(eV atom). Considering that a large DOS around the Fermi level may lead to a higher chance of superconductivity, this layered boron crystal structure is worth further investigation.

5.3 Summary

Using first-principle calculations, a new class of layered boron crystals is proposed which is built from two-dimensional boron sheets. Although not as stable as α rhombohedral boron at ambient conditions, layered boron crystals become competitive with α boron, γ boron and α-Ga boron under high pressure. In addition, layered boron crystals have a larger DOS around their Fermi level when compared to other boron phases.

Chapter 6

Hydrogen storage with boron nano-materials

Hydrogen is a promising source for clean and renewable energy and may replace fossil fuels in the future [105, 106]. Developing novel materials to efficiently store hydrogen with high gravimetric and volumetric densities is a very challenging topic since the hydrogen storage and release should be performed close to room temperature and under ambient conditions [106]. Carbon based nano-materials are good candidates for hydrogen storage because of their light weight and easy fabrication in experiments [107, 108, 109, 110, 111]. For convenience of operation, physisorption of hydrogen on the surface of carbon nano-structures is preferred [112]. In addition, to operate around room temperature, the binding energy of hydrogen should be in the range of a few tenths of an eV/H_2 [111, 113]. However, the interaction between H_2 and pure carbon surfaces is weak and the binding energy is usually $\sim$0.05 eV/H_2 [112]. Researchers have proposed various methods to increase the binding energy by decorating carbon nano-structures with metal dopants [109, 110, 111, 114]. Ca doped carbon fullerenes and nanotubes turn out to be the optimal one with hydrogen storage weight percentage up to 9% as shown by first-principles calculations [114].

As the neighbor of carbon, metal doped boron fullerenes and nanotubes were also investigated as possible candidates for hydrogen storage materials. Various model systems have been studied including transition metal doped boron fullerenes, Li and Ca doped boron fullerenes and nanotubes, all of which show encouraging results [115, 116, 117, 118, 119]. In this chapter, I discuss physisorption and chemisorption of hydrogen on pristine and various metal doped boron nano-structures. The dynamics of hydrogen absorption is explored by calculating energy barriers between physisorption and chemisorption. Finally pros and cons of boron based hydrogen storage materials are discussed and possible future questions are raised. In the calculations, we use the PWSCF code [103, 104] and the LDA for exchange and correlation [58]. Results are checked with GGA-PBE [60]. K-point sampling of the Brillouin zone uses a Gaussian smearing width of 0.05 eV. The nudged elastic band method [81, 82, 83, 84] is employed to compute the energy barriers for hydrogen from physisorption to chemisorption. We have focused on the most stable α sheet and nanotubes based on the α sheet, although there are many other stable boron sheets [6].

6.1 Hydrogen on boron sheets and nanotubes

We would like to first clarify the differences between physisorption and chemisorption of hydrogen. In physisorption, the bonding of the hydrogen molecule stays approximately intact and the interaction between hydrogen and substrate is mainly of weak van der Waals type. Since physisorption does not break any covalent bonds, there are no (or very small) energy barriers for physisorption which is good for fast storage and release of hydrogen. On the other hand, in chemisorption H-H bonds are broken (or damaged) and H atoms make strong chemical bonds with the substrate. In this case, the absorption energies can be much larger. Chemisorption usually needs to overcome large energy barriers when breaking H-H bonds and the process is usually slow.

We define the absorption energy per H_2 as

$$E_{ab} = E_{H_2} + (E_B - E_{B+H_2})/N_{H_2}, \tag{6.1}$$

where E_{H_2} is the energy of a free-standing H_2 molecule, E_B is the energy of the boron substrate, E_{B+H_2} is the energy of the whole system (boron substrate + hydrogen) and N_{H_2} is the number of adsorbed hydrogen molecules. A system is stable compared to separated boron substrate and isolated hydrogen molecules when E_{ab} is larger than zero. Lager E_{ab}

Table 6.1: Absorption energy E_{ab} (in meV/H_2) for hydrogen physisorption on a pristine α sheet and the (3,0) α-sheet-derived boron nanotube. Four different configurations are considered in each case: hydrogen on top of a hexagon parallel (hex $\|$) or perpendicular (hex $\perp$) to the surface, and hydrogen on top of a triangular atom parallel (tri $\|$) or perpendicular (tri $\perp$) to the surface.

	hex $\|$	hex $\perp$	tri $\|$	tri $\perp$
α sheet	70	86	81	78
(3,0) BNT	94	93	97	87

means more stable binding of hydrogen to the substrate.

6.1.1 Physisorption

We start with discussing hydrogen physisorption on pristine boron sheets and nanotubes. Table 6.1 shows the calculated E_{ab} for hydrogen physisorption on pristine α sheets and the (3,0) α-sheet-derived boron nanotube for different absorption sites and H_2 configurations. We can see that the absorption energy for hydrogen physisorption on the α sheet is uniform for different absorption sites and is in the range of 70-90 meV/H_2, which is larger than graphene. For the (3,0) boron nanotubes, the binding between hydrogen and boron is strengthened slightly by the curvature, and the absorption energy is closer to 100 meV/H_2. Although hydrogen binds stronger on boron nanostructures than carbon [40], the absorption energy is far too small for practical applications at room temperature. Hence, physisorption of hydrogen on pristine boron nanostructures is not a plausible mechanism for hydrogen storage.

6.1.2 Chemisorption

Next, we show results of hydrogen chemisorption on the α sheet and the (3,0) nanotube. When chemisorbed on the α sheet, H_2 is decomposed into two hydrogen atoms which then bond to two boron atoms. We have studied chemisorption of one H_2 molecule on a

Table 6.2: Absorption energies (in eV/H_2) and energy barriers (in eV) from physisorption to chemisorption for different configurations of hydrogen chemisorption on α sheet. Configuration (1,7) is unstable and E_{ab} and $E_{barrier}$ are not shown.

sites	(1,2)	(1,3)	(1,4)	(1,7)	(2,8)	(7,11)	(1,8)	(1,9)	(1,10)	(1,11)
E_{ab}	0.04	-0.04	-0.12	-	0.49	0.22	-0.11	0.48	0.39	0.61
$E_{barrier}$	1.54	1.34	1.18	-	1.41	1.35	1.48	1.21	1.37	0.84

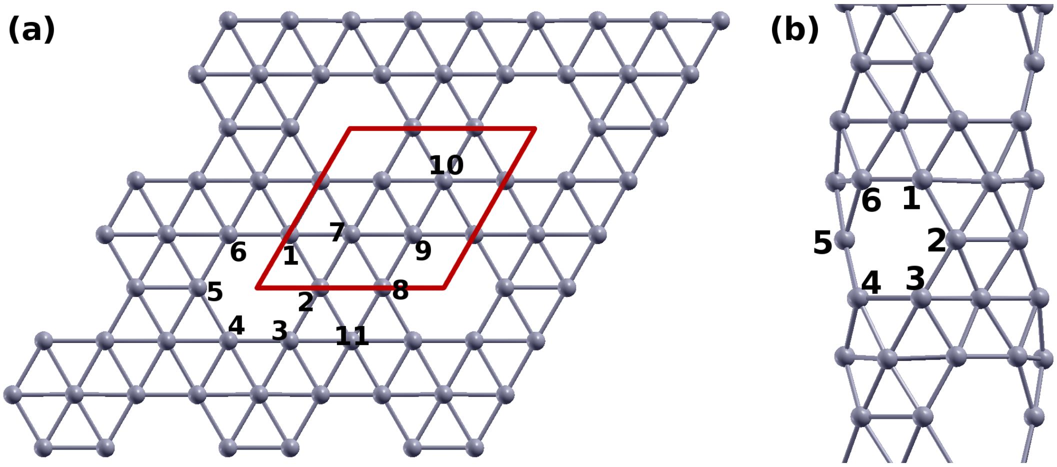

Figure 6.1: (a) Absorption sites on the α sheet for hydrogen chemisorption denoted by numbers from 1 to 11. (b) Absorption sites on the (3,0) boron nanotubes for hydrogen chemisorption denoted by numbers from 1 to 6.

2×2 unit cell of the α sheet with different absorption sites for two hydrogen atoms. We denote absorption sites using numbers from 1 to 11 as shown in Figure 6.1(a). Table 6.2 shows E_{ab} for different inequivalent configurations of two hydrogen atoms absorbed on the α sheet. For instance, (1,2) means one H atom is attached on atom 1 and the other H atom is bonded to atom 2. We can see from the Table that for some configurations E_{ab} is negative, meaning that these configurations are not as stable as separated α sheet and hydrogen molecules. In other words, the energy gain from forming B-H bonds is not always sufficient to compensate the energy cost to break H-H bonds. For those configurations with positive absorption energies, E_{ab} is in the range from 0.2-0.6 eV/H_2, which is in the optimal desired range. The most stable absorption site is (1,11) which has E_{ab}=0.61 eV/H_2.

For the nanotube (3,0) made of the α sheet, we have calculated E_{ab} for six different inequivalent configurations of hydrogen chemisorption. We use a similar denotation for absorption sites as shown in Figure 6.1(b). Table 6.3 shows the absorption energies. Compared to the flat α sheet, curvature drastically increases the absorption energies for hydrogen and E_{ab} is always positive for the configurations we have studied. Similar effects have been seen for graphene and carbon nanotubes [120, 121]. A simple rationalization would be that curvature mixes in-plane states and out-of-plane states inducing sp_3-type hybridization such that each boron atom can bind hydrogen atoms more strongly. All

Table 6.3: Absorption energy (in eV/H_2) and energy barriers (in eV) from physisorption to chemisorption for different configurations of hydrogen chemisorbed on boron nanotube (3,0). Configurations (1,2) and (1,5) are unstable and are relaxed into (1,3) and (1,4), respectively.

	(1,2)	(1,3)	(1,4)	(1,5)	(1,6)	(2,5)
E_{ab}	-	1.40	1.35	-	0.94	0.40
$E_{barrier}$	-	0.50	1.03	-	0.70	0.38

configurations have absorption energies close to or larger than 1 eV/H_2, indicating very strong binding (except for configuration (2,5)).

6.1.3 Energy barriers for chemisorption

Although physisorption of hydrogen on the α sheet and nanotube (3,0) results in too weak binding, chemisorption has led to reasonable absorption energies for α sheet, which suggests that hydrogen chemisorption on boron sheets and nanotubes might be a plausible mechanism for hydrogen storage. However, chemisorption usually needs to overcome large energy barriers, and the energy barriers for hydrogen release can be even larger. We should consider how large the energy barriers are and how efficiently H_2 can be chemisorbed and released from chemisorption configurations. To address these questions, we calculate the minimal energy reaction path from physisorption to chemisorption using nudged elastic band method and determine the energy barriers. Figure 6.2 shows a calculated reaction path from physisorption to chemisorption configuration (1,3) as an example. As we expected, the maximal energy on the path is where H-H bond is broken and this point determines the energy barrier for the reaction.

Tables 6.2 and 6.3 show the energy barriers from physisorption to chemisorption for both the α sheet and the (3,0) nanotube. For the α sheet, the energy barriers are in the range of 0.84 eV to 1.54 eV, and for the (3,0) nanotube the energy barriers are a little smaller, with the smallest energy barrier being 0.38 eV. Compared to graphene and carbon nanotubes, the energy barriers from physisorption to chemisorption are much smaller for hydrogen absorbed on boron sheets and nanotubes and hence chemisorption is more plausible. However, compared to room temperature, these energy barriers for chemisorption are too large and the efficiency of hydrogen absorption and release will be very low. In our

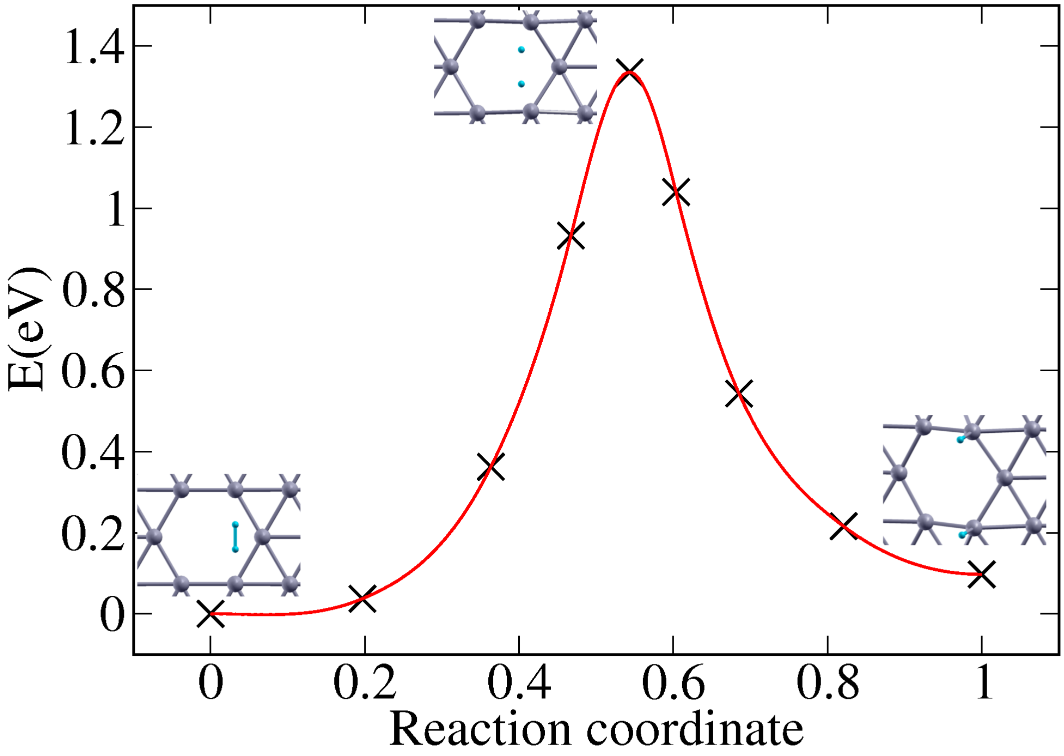

Figure 6.2: Minimal energy reaction path for hydrogen absorbed on the α sheet from physisorption (at reaction coordinate 0) to chemisorption configuration (1,3) (at reaction coordinate 1).

opinion, pristine boron sheets and nanotubes cannot be used as hydrogen storage materials at room temperature.

6.2 Hydrogen on metal doped boron nanostructures

6.2.1 Physisorption

Since pristine boron sheets and nanotubes are not suitable for hydrogen storage, we have considered decorating boron nanostructures with light metal atoms, including alkali and alkaline earth metals. These metal atoms are attached to the surfaces of boron nanostructures and serve as absorption sites for hydrogen. We have studied five different metal dopants (Li, Na, K, Mg and Ca). Because alkali and alkaline earth metal atoms do not aggregate on top of the α sheet and nanostructures based on the α sheet, adsorption of hydrogen on metal doped α sheets can be well approximately by hydrogen interacting with an isolated metal atom. In our calculations, we only examine the case of an isolated metal

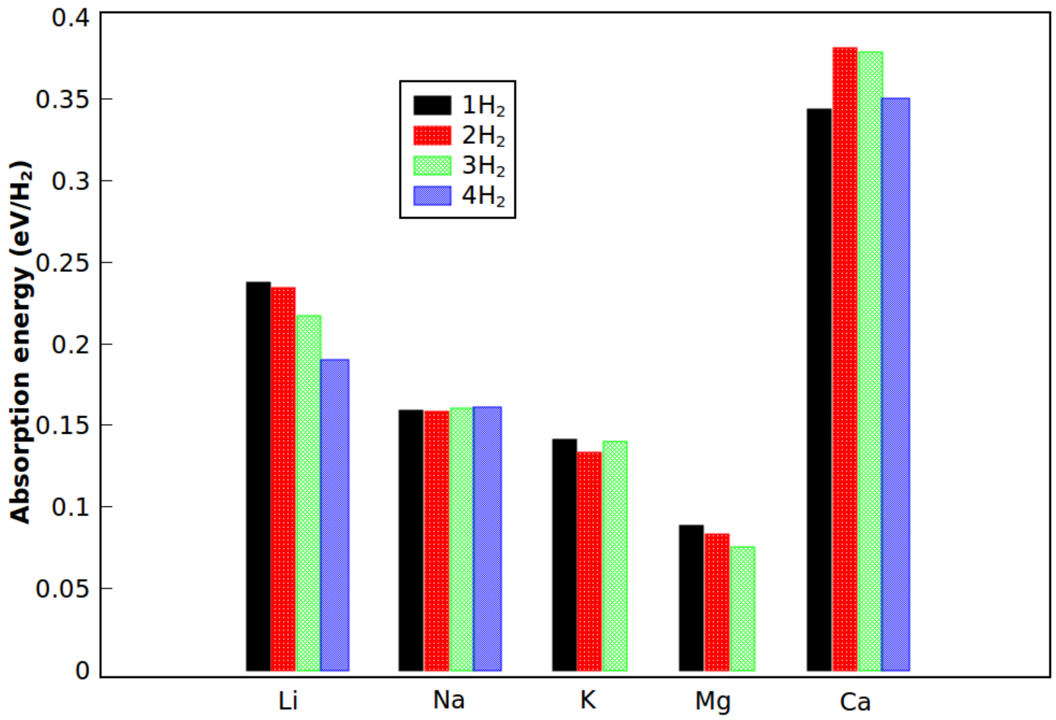

Figure 6.3: Physisorption energies (in eV/H$_2$) for hydrogen on five different kinds metal doped α sheet with different numbers of hydrogen molecules.

atom with hydrogen absorbed around it. The most stable absorption site for an isolated metal atom on a boron sheet or nanotube is on top of a hexagon.

We first consider the physisorption process of hydrogen on metal doped α sheet. Figure 6.3 shows the physisorption energies of hydrogen for different metal dopants on the α sheet and versus the number of hydrogen molecules. We can see that the absorption energies are larger than pristine boron sheets and nanotubes. However, only Li and Ca have absorption energies within the desired range of 0.2 eV-0.4 eV; the other three metal dopants do not provide strong enough binding. Ca is preferable to Li because of the larger binding energies. In order to check how curvature of the boron surface may change the binding energies, we have computed the absorption energies for hydrogen physisorption on metal-doped B_{80} fullerenes and nanotubes and found out that the absorption energies are almost the same as the Ca doped α sheet. Hence, curvature of the boron surface does not contribute to physisorption energy of hydrogen to metal dopants.

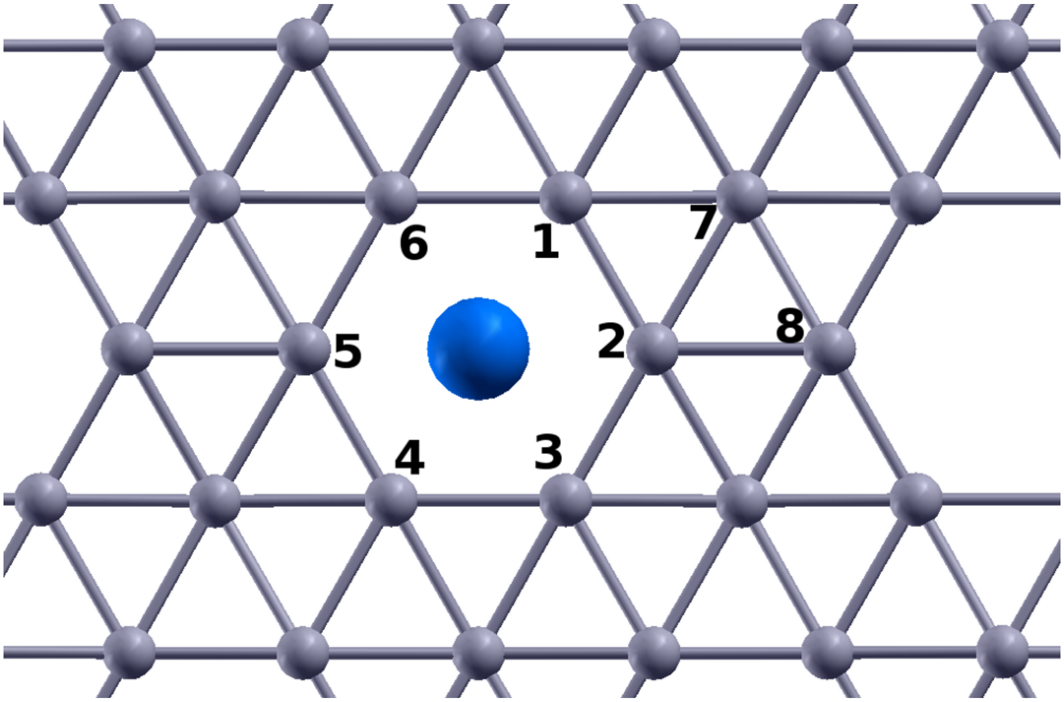

Figure 6.4: Chemisorption sites for Ca doped α sheet. Large blue ball is Ca and small gray balls are B.

6.2.2 Chemisorption and energy barriers

We now focus on Ca doped α boron sheets and study hydrogen chemisorption. We consider different absorption sites as shown in Figure 6.4. Table 6.4 shows the chemisorption energies for different configurations. Compared to the pristine α sheet, the chemisorption energies are much larger and are positive for all configurations considered. In addition, we calculate the energy barriers from physisorption to chemisorption as shown in Table 6.4. For some of the configurations, the energy barriers are surprisingly small. In particular, the energy barrier for (1,7) is only 0.10 eV. Hence, chemisorption is greatly facilitated by Ca.

Furthermore, we have discovered an extremely stable chemisorption configuration. We

Table 6.4: Chemisorption energy (in eV/H_2) and energy barriers (in eV) from physisorption to chemisorption for different configurations of hydrogen chemisorbed on Ca doped α sheet.

	(1,2)	(1,3)	(1,4)	(1,7)	(2,8)
E_{ab}	1.00	0.94	0.89	0.80	0.75
$E_{barrier}$	0.54	1.03	1.83	0.10	0.42

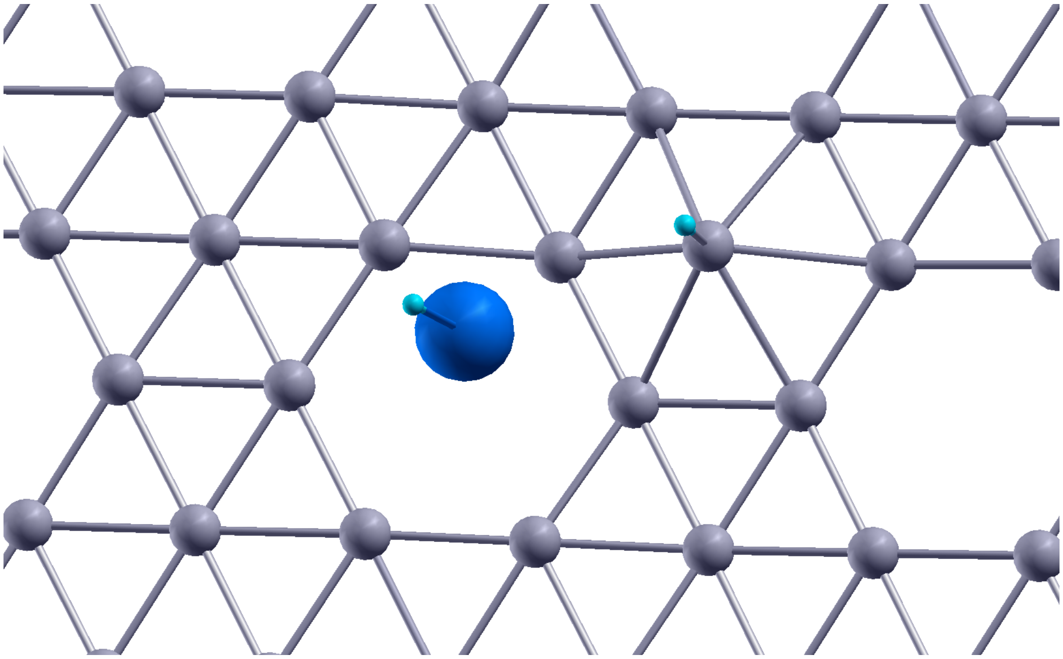

Figure 6.5: A stable configuration for hydrogen chemisorption which has almost zero energy barrier from physisorption to chemisorption. Large blue ball is Ca, small green blue balls are H and medium gray balls are B.

show this configuration in Figure 6.5. Instead of having both hydrogen atoms bonded to boron atoms, only one H atom is bonded to a boron atom and the other one sits on top of the Ca atom. The absorption energy for this configuration is 1.20 eV/H_2. Furthermore, we have found out that this configuration of chemisorption has almost zero energy barrier (less than 50 meV) to physisorption.

Since chemisorption of hydrogen on the Ca doped α sheet has a tiny energy barrier, we consider the extreme case where there is one H atom bonded to each of the six boron atoms close to Ca atom. We calculate the absorption energy for additional hydrogen molecules physisorbed on this hydrated system. The calculated absorption energies for first three hydrogen molecules are about 0.24 eV/H_2, which are 50% less than the case where no hydrogen molecules are chemisorbed. Hence, chemisorption of hydrogen can lower the performance of Ca doped α sheets as hydrogen storage materials.

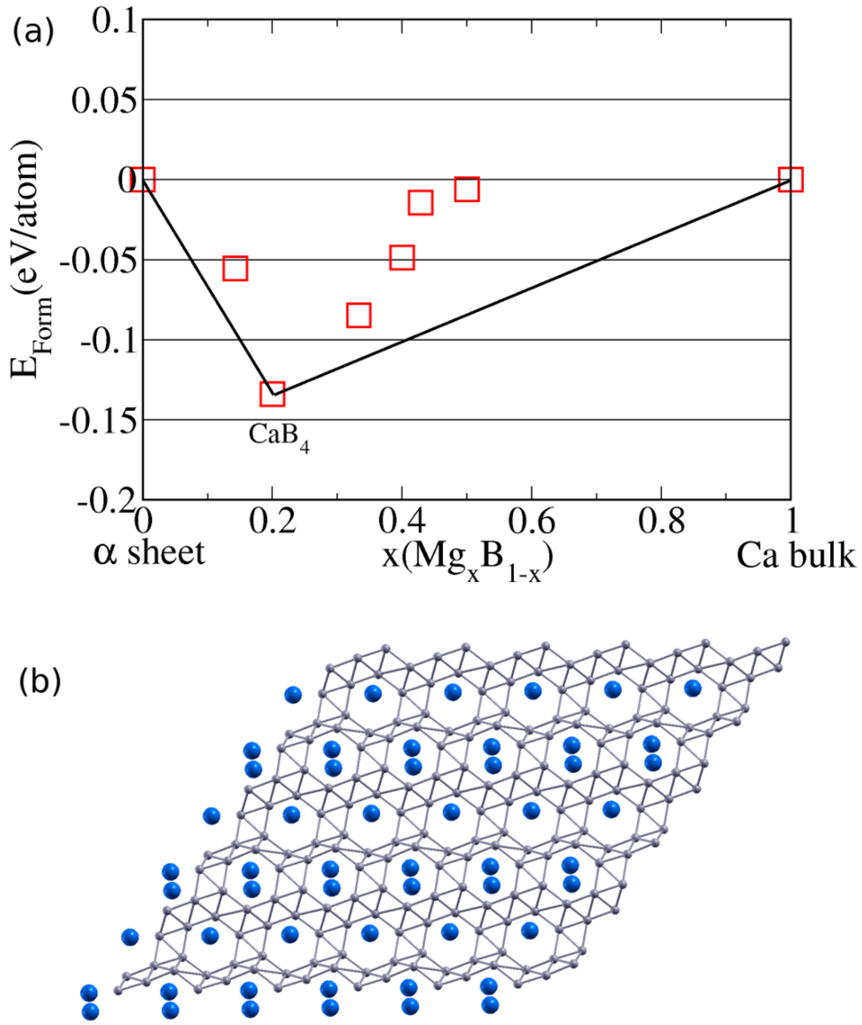

Figure 6.6: (a) A preliminary phase diagram for two-dimensional Ca borides based on single-layered boron sheets. (b) Structure of the CaB_4 sheet.

6.2.3 Stability of Ca doped boron sheets

In the previous sections, we have learned that Ca doped α sheets might be good hydrogen storge materials if we consider only physisorption of hydrogen. In this section, we discuss the stability of Ca doped boron sheets and suggest that researchers may have been working on the wrong material stoichiometry: *i.e.* Ca doped α sheets may not be the relevant material.

To achieve high density of hydrogen storage, boron sheets (or fullerenes, nanotubes) need to be highly doped by Ca to provide sufficient absorption sites. Since Ca is expected to donate electrons to α sheet, similar to our argument for Mg borides [7], a large concentration of Ca on boron sheets will change the boron sheet structures, and α sheet based structures will not be the most stable ones. The optimal stoichiometry and structure can be found by using a similar method to Mg borides (*i.e.* genetic algorithms). In Figure 6.6, we show a very preliminary phase diagram for two-dimensional Ca borides based on single-layered boron sheets. According to this phase diagram, a CaB_4 sheet structure is the most stable stoichiometry for two-dimensional Ca boride sheets. Because the phase diagram is based on limited data, further study is needed to explore detailed information of the phase diagram. Furthermore, all work on hydrogen storage of Ca doped boron nanostructures should be reinvestigated using the most stable Ca boride structure.

6.3 Summary

We have studied physisorption and chemisorption of hydrogen on pristine and metal doped boron nanostructures. For pristine boron sheets and nanotubes, we found that physisorption of hydrogen does not provide enough binding for room-temperature operation. In addition, chemisorption of hydrogen can have absorption energies in the right range but can be difficult to achieve due to large energy barriers from physisorption to chemisorption. For metal doped boron sheets, Li and Ca are the right metal elements to decorate boron nanostructures and provide absorption sites for physisorption of hydrogen. Ca is better than Li because of larger absorption energies. Furthermore, we have shown that energy barriers are very small and even close to zero for hydrogen to be chemisorbed on Ca doped boron sheets, which can reduce the absorption energy for additional physisorbed hydrogen molecules. Hence, in our opinion, Ca doped boron nanostructures might not be the ideal materials for hydrogen storage. In the end, we show very preliminary results on the phase diagram of two-dimensional Ca borides and suggest that researchers might have been working on the wrong material composition and structures. Further research is needed to evaluate boron nanostructure-based hydrogen storage.

Chapter 7

Conclusions

The goal of this thesis is to understand boron and Mg boride nanostructures using first-principles calculations based on density functional theory, focusing on their structures, bonding, electronic properties and possible applications on hydrogen storage. Our systematic research contributes valuable information to the knowledge of boron nanomaterials.

In the first part of this thesis, boron sheets and nanotubes are investigated. As the starting point for nanotubes, two-dimensional sheet structures need be studied first. For boron the sheet structures are not as trivial as graphene is to carbon because no such boron structures exist in nature. Luckily we can borrow ideas from graphene and small clusters of boron. The direct analogy to graphene, the hexagonal boron sheet, is unstable with respect to shearing perturbation. On the other hand, small boron clusters are quasi-planar and made of triangular motifs. The triangular boron sheet derived from boron clusters is much more stable than the hexagonal sheet but not optimal. Instead, a class of stable boron sheets can be constructed via mixing the hexagonal and triangular phases and benefit from the balance of two-center bonding in hexagonal regions and three-center bonding in triangular regions. Equivalently these boron sheets can be considered to be constructed by removing atoms from a triangular template sheet. The stability of these boron sheets is dependent on the hexagon hole density η, which is the ratio of removed atoms to the triangular template. The most stable boron sheet, α sheet, occurs at η=1/9.

As further shown with maximally localized Wannier functions, boron atoms in the triangular regions of boron sheets act like "perfect electron donors". When a boron atom is added to the center of a hexagon, the number of bonding states does not change such that the only effect of the added boron atom in the triangular region is to increase the number of electrons by three. Equivalently the added atom donates all its three valence electrons to the hexagon lattice via multi-center bonding and we name this phenomenon “self-doping”. Self-doping naturally explains the stability of α sheet – atoms in the triangular regions donate all their electrons, giving the hexagonal lattice the same number of electrons as graphene. In addition, self-doping links boron nanostructures with carbon nanostructures. Similar to α sheet and graphene, starting from a stable carbon nanostructure, a corresponding stable boron nanostructure can be constructed by replacing carbon with boron and adding the right number of electrons to hexagon centers. Finally, self-doping provides a scheme to efficiently search for the optimal Mg boride sheet structure with given stoichiometry.

Composed of mixtures of hexagons and triangles, boron sheets are not always flat. Boron sheets with small η prefer buckled groundstate geometries, while the others always stay flat with the separational point at η=1/9. This asymmetric buckling behavior cannot be explained by mixing of in-plane σ and out-of-plane π states, which in fact generates contradictory results. Instead an unconventional electron gas picture can lead to a reasonable explanation to the buckling of boron sheets which links buckling to increasing of η such that only buckling in small-η sheets is preferred. This asymmetric buckling has important consequences on double-layered boron sheets. When constructed from two identical atomically thin boron sheets, double-layered boron sheets can have interlayer bonds formed if only the constituent boron sheets prefer to buckle. These interlayer bonds in double-layered boron sheets are strong and two-center-like due to which the most stable double-layered boron sheet occur at η=1/12 and is semiconducting with a band gap of 0.8 eV.

With single-layered boron sheets as precursors, single-walled boron nanotubes can be constructed. While electronic properties of large single-walled boron nanotubes can be predicted from their precursors via a zone-folding technique, small boron nanotubes possess rather peculiar geometries and electronic properties. Although α sheet is metallic and flat such that large-diameter boron nanotubes are metallic, small-diameter boron nanotubes based on α sheet prefer buckled surfaces with atoms in the triangular regions going inward and outward alternatively, due to which small-diameter boron nanotubes are semiconducting. This metal-to-semiconductor transition occurs for boron nanotubes when their diameter is smaller than 20 Å. Interestingly, for small boron nanotubes energy gain from surface buckling is at most a few tens of meV/atom which is small even compared to room temperature. However, the semiconducting behavior is expected to be quite stable under thermal and soliton perturbations.

Similar to single-walled boron nanotubes, double-walled boron nanotubes can be built with the most stable double-layered boron sheet as precursor. Double-walled boron nanotubes built in this way tend to have huge curvature energies because inner and outer nanotubes are identical such that the inner one is compressed and the outer one is stretched around the circumference. To release the strain, a small inner nanotube and a large outer nanotube should be used to construct a double-walled boron nanotube whose energy is optimized with respect to the diameter of the inner nanotube. The resulting double-walled boron nanotubes benefit from a good balance between strain release and inter-walled bond formation. Compared to single-walled boron nanotubes, double-walled boron nanotubes are always more stable and are metallic for the interesting range of diameters. Following this trend, boron nanotubes are expected to be more stable with increasing number of walls. Given the hollow structures fabricated in experiments, certain kinetic limitation mechanism should play a crucial role in the growth of boron nanotubes. However, this kinetic process can be very difficult to simulate.

The second part of this thesis discusses the structures and phase diagrams of Mg boride nanostructures. Again, Mg boride sheet structures are the starting point. If focusing on structures based on single-layered boron sheets, one can consider Mg boride sheets as the product of doping boron sheets with Mg atoms. When doped on different single-layered boron sheets, Mg atoms tend to have different charge states, resulting distinct interactions between Mg atoms. Mg atoms are attractive on small-η boron sheets but repel each other on large-η boron sheets. Due to interactions between Mg atoms, Mg doped small-η boron sheets prefer to have Mg stay inside when curved to form nanotubes; it is the opposite for large-η boron sheets. When energy gains from Mg-Mg interaction overcome energy losses on bending covalent boron bonds, Mg boride nanotubes can be more stable than the precursor sheets, indicating negative curvature energies. The negative curvature energy is a unique phenomenon for Mg boride nanotubes and may be important for the growth of Mg boride nanotubes.

To further understand the overall phase diagrams for two-dimensional Mg boride sheet structures, the most stable sheet structures at various stoichiometries are searched globally using a genetic algorithm. Two different structural constraints are considered – the constituent boron sheets are limited to be atomically thin or are allowed to be double-layered. In the first case, the optimal structures at all stoichiometries can be understood with the self-doping picture where larger Mg concentration results in large η for the constituent boron sheets. The stable phase under boron-rich environments is a MgB sheet based on a hexagonal boron lattice which coexists with α sheet. Once allowing for structures based on double-layered boron sheets, more stable structures are found to be based on the double-layered hexagonal boron sheet. Under boron-rich environments, several double-layered hexagonal boron sheet based Mg boride sheets can coexist with the most stable double-layered boron sheet.

When considering nanotubes built from Mg boride sheets, curvature effects can be important for the phase diagrams, especially for small-diameter nanotubes. On one hand, stable phases from sheet phase diagrams all have large curvature energies and are thus difficult to curve into nanotubes. Furthermore, structures based on double-layered boron sheets are much harder to curve than those based on single-layered sheets. On the other hand, certain Mg boride sheets even prefer curved geometries due to Mg-Mg interactions. From our rather preliminary results, we observe two trends for the stable phases. First, structures with small or even negative curvature energies are more preferred for small diameters. Second, structures based on single-layered boron sheets tend to win over those double-layered structures for small diameter.

In the third part of the thesis, layered boron crystals based on boron sheet structures are proposed based on first-principle calculations. These layered boron crystals are constructed by stacking boron sheets perpendicular to their surfaces with multi-center-like bonds forming between layers. Compared to α rhombohedral boron, layered boron crystals are less stable by 0.15 eV/atom under ambient conditions but can become more stable under high pressure. When pressure is about 100 GPa, layered boron crystals are comparable in stability with two other stable high-pressure phase – γ boron and α-Ga boron. Given the fairly large DOS around Fermi level for layered boron crystals, they might be more likely to be superconducting.

The last part of the thesis is dedicated to the possible application of boron nanomaterials for hydrogen storage. For pristine boron sheets and nanotubes, the absorption energy of hydrogen is too small if hydrogen is physisorbed. On the other hand, the energy barriers for hydrogen to be chemisorbed are too large to allow fast performance of absorption and release. In fact, to achieve fast operation physisorption of hydrogen with the right absorption energies is always preferred. Hence, pristine boron nanostructures are not suitable for hydrogen storage. Among various metal doped boron nanostructures, Ca doped ones are optimal and provide the right absorption energy for hydrogen to be physisorbed. However, the existence of Ca results in very small or even close to zero energy barriers for the chemisorption of hydrogen on boron sheets and facilitates the chemisorption process. The chemisorbed hydrogen atoms can subsequently jeopardize the performance of Ca atoms as absorption sites, raising the question whether Ca doped boron sheets or nanotubes are the right materials for hydrogen storage. Furthermore, high concentration of Ca doping can change the groundstate geometries of boron sheets by donating many electrons to boron. Hence, Ca doped α sheet or α nanotubes may not be the right system to investigate. Instead similar procedures to Mg boride sheets should be performed which first determines the stable stoichiometry and structure then investigates hydrogen storage properties based on the stable structure.

Further problems

In this thesis we have mainly concentrated in structures, bonding and electronic properties of boron and Mg boride nanostructures. We are also interested in further investigating several other problems. One of the problems involves the differences between the second row and the third row elements in periodic table, e.g., B and Al, C and Si. If viewed from pseudopotentials, C and Si are very similar – they have the same number of electrons and similar pseudopotentials converging to $-4/r$. However, C and Si have rather different properties. For instance, the groundstate structure of C is graphite while for Si it is diamond structure. From constructing pseudopotentials we know that properties of materials are determined by not wavefunctions in the core regions but wavefunctions in the interstitial regions. Hence the differences between C and Si should be determined by the shape of their atomic wavefunctions outside core regions. The shape of an atomic wavefunction is usually described via two factors – locality which measures how localized the wavefunction is around the core, and eigen-energy which shows the asymptotic decay rate of the wavefunction. We would like to know which one is the major factor determining the differences by changing one factor while fixing the other.

Another problem we are interested in is the possibility to grow two-dimensional boron sheets directly on flat substrates. Unlike graphene, boron sheets do no exist in nature and are not very stable compared to bulk boron. To grow boron sheets in a similar manner to graphene, we need a substrate which binds boron atoms strongly to avoid bulk-like phases while in the same time provides good mobility for boron atoms to move on the substrate. Possible candidates for the substrates are various close-packed transition metal surfaces. We are trying to search over various candidates to find the optimal one.

Finally, with analogy to graphene nanoribbons, boron nanoribbons are expected to have novel properties due to electron confinement and edge effects. To approach this problem, we can have many degrees of freedom to construct boron nanoribbons such as precursor sheets with different η and hexagon patterns, different cutting directions. As a starting point, we have studied nanoribbons constructed from the flat triangular sheet and discovered interesting properties. For instance, boron nanoribbons from the triangular sheet are metallic for most cases but can become semiconducting with specific cutting direction and width. In addition, boron nanoribbons prefer to be cut along B-B bonds generating smooth edges and these smooth-edged nanoribbons sometimes are more stable than the precursor triangular sheet. We expect further work to be done on nanoribbons based on more general precursor sheets.

Appendix A

Genetic algorithm

A.1 Basic procedure

The basic procedure of a genetic algorithm in predicting crystal structures is illustrated in Figure A.1. In the following context, we explain the procedure in details.

Representation of structures

For each structure, we represent its unit cell with a 3×3 matrix in which each row is a lattice vector. To remove the redundancy from rotation, we transform the lattice matrix into lower-triangular format. Equivalently we rotate the structure and make the first lattice vector align along x axis and second lattice vector lie in x-y plane. In following calculations, lattice matrices are always represented in or transformed to lower-triangular format. On the other hand, atomic positions are in fractional coordinates which facilitates crossover of two structures.

Generation of random structures

We randomly generate initial structures with constraints to avoid too unreasonable configurations. First, we randomly generate the 3×3 lattice matrix with nine random numbers and make sure that they fulfill the following requirements: a) angles between any two lattice vectors are between 50° and 130°, and b) ratio between lengths of any two lattice vectors is between 1/3 and 3. We then transform the lattice matrix into lower-triangular format which is then multiplied by a common factor to make sure that volume of the unit cell is within reasonable range. Second, all atomic coordinates are generated in fractional

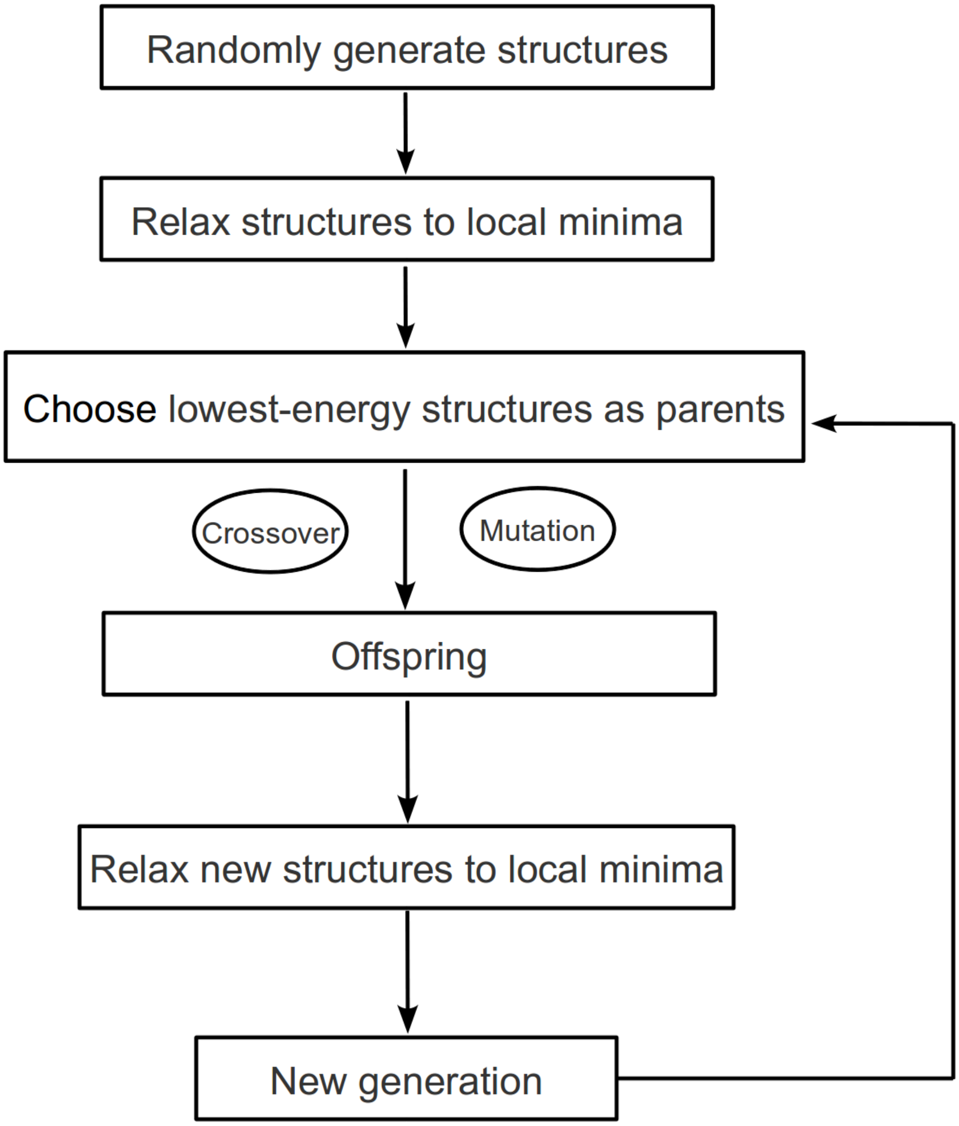

Figure A.1: Basic procedure of genetic algorithm in predicting crystal structures.

units with random numbers and distances between any two nearest neighbors are ensured to be larger than 1 Å. In principle, more constraints in the generating initial random structures will lead to faster convergence of the final structures but might increase the chances to miss optimal structures.

Local minimization

To relax each structure to the corresponding local minimum, we have used a standard DFT code SIESTA with the conjugate gradient method. SIESTA is very stable when relaxing randomly generated structures which are usually highly distorted. In contrast, we have done some testing and used PWSCF to relax random structures. We found out that the BFGS algorithm in PWSCF is unstable when relaxing structures far from local minima and shows unreasonable large stresses after a few ionic steps. On the other hand, local minimization is in principle not necessary and was not used in many versions of genetic algorithm codes. However, local minimization has been proven to be indispensable for structure prediction in practice. The reason is quite simple. Local minimization greatly simplifies the free energy surface and removes many degrees of freedom in constructing crystal structures such as small changes of bong length and bond angles. In addition, local minimization is a very mature technique in first-principles calculations and can be performed very efficiently. Overall, local minimization is able to speed up genetic algorithm calculations very much and should be included in all calculations.

Crossover and Mutation

Crossover means the process that two parent structures combine together to generate new structures. The generated new structure should keep some characteristics from each parent structure. In a genetic system, crossover of chromosomes is rather straight forward because each chromosome can be essentially represented by an one-dimensional array of 1s and 0s and crossover can be done by cut-and-paste. However, for crystal structures crossover can be quite tricky because each structure is represented by a 3×3 lattice matrix and fractional coordinates of atoms. In practice, crossover of two crystal structures involves two parts.

First, the new lattice matrix is generated by mixing the lattice matrices of two parents randomly. A random number r_L is generated and the lattice matrix of the offspring structure is obtained by

$$L_{os} = r_L \times L_{p1} + (1 - r_L) \times L_{p2}, \tag{A.1}$$

where L_{p1} and L_{p2} are the lattice matrices of two parents.

Second, atomic coordinates of the new structure are obtained in the following way. Essentially we would like to cut the two parent structures along a certain direction, pick one part from the first parent and another part from the second parent, stick the two parts together and form a new structure to be used in the next generation. In practice, we first randomly choose a lattice vector and let us assume we have picked the first lattice vector. Then we generate a random number r_A in [0,1) and choose atoms from the first parent with the first coordinate smaller than r_A and additional atoms from the second parent with the first coordinate lager than r_A to form the offspring structure. We check the number of atoms for each species – we remove atoms randomly if there are too many and add atoms randomly if there are too few.

On the other hand, mutation changes crystal structures randomly and abruptly with certain probabilities. Mutation provides the mechanism to bring novel properties into the system and is especially important when trying to jump out from a local minimum. Three operations can be done for mutation – changing lattice matrix, perturbing atomic positions, and switching positions of atoms from different species. Among three operations, perturbing atomic positions is least important because local minimization cancels most of the effects from small perturbation of atomic positions. In practice, the operation to perturb atomic position can be safely neglected.

Parameters and convergence

For a typical genetic algorithm calculation to deal with problems with 20 to 30 atoms, we use 20 structures in each generation and choose 12 most stable ones as parents to generate new structures for next generations. We generate one new structure by changing the lattice matrix, one new structure by switching atoms from different species and the remaining structures from the crossover of two parents. In addition, the most stable structure in each generation is kept to compete in the next generation. We assume one genetic algorithm calculation converges when at least 5 structures in one generation are the same as the most stable one. Most of our calculations converge in less than 15 iterations. We have set our maximal number of iterations to be 20.

A.2 Adaptation to two-dimensional sheets and Nanotubes

Genetic algorithm can be easily adapted to studying two-dimensional sheet structures and nanotubes. For two-dimensional sheet structures, we set up structures in the x-y plane and vacuum along z. We fix the z lattice constant to be 30 Å for all structures. When generating initial random structures, only the first two lattice vectors are randomly generated and are fixed in the x-y plane. In addition, z coordinates of atoms are randomly generated in the range of [0, 0.3) to ensure a two-dimensional configuration. In the process of local minimization, only the first two lattice vectors are relaxed and are always kept in the x-y plane. In crossover, only the first two lattice vectors can be chosen to perform cut-and-paste. In addition, to avoid the occurrence of bulk-like phases for our Mg boride sheet structures, we have applied penalty functions to constrain the constituent boron structures to be sheet-like. We add the following function to the total energy of each Mg boride structure during the competition process

$$E_{penalty} = K \times \sum_{i}^{\text{B atoms}} [(|z_i - \bar{z}| - L) \times H(|z_i - \bar{z}| - L)]^2, \qquad \text{(A.2)}$$

where z_i is the z coordinate of boron atom i, $\bar{z}$ is the average z coordinate of all boron atoms, K and L are two parameters, the sum is over all boron atoms, and $H(x)$ is the Heaviside step function (equal to 0 if $x < 0$, 1 if $x \geq 0$). Basically, we apply a quadratic penalty to the total energy once the distance between a boron atom and the xy plane defined by $\bar{z}$ is larger than L. By varying the values of K and L, we are able to confine the constituent boron sub-systems of all Mg boride structures to be single-layered or double-layered, which are the two types of scenarios we have investigated.

For nanotubes, we perform all genetic algorithm procedure on their precursor sheets and make structures compete with each other based on total energies calculated from nanotubes. First, we randomly generate sheet structures and roll them into nanotubes. After relaxing these nanotubes into their local minima, we choose a certain number of most stable ones from the relaxed nanotubes and obtain their precursor sheets. We perform crossover and mutation on these sheets to generate new sheet structures which are then rolled up

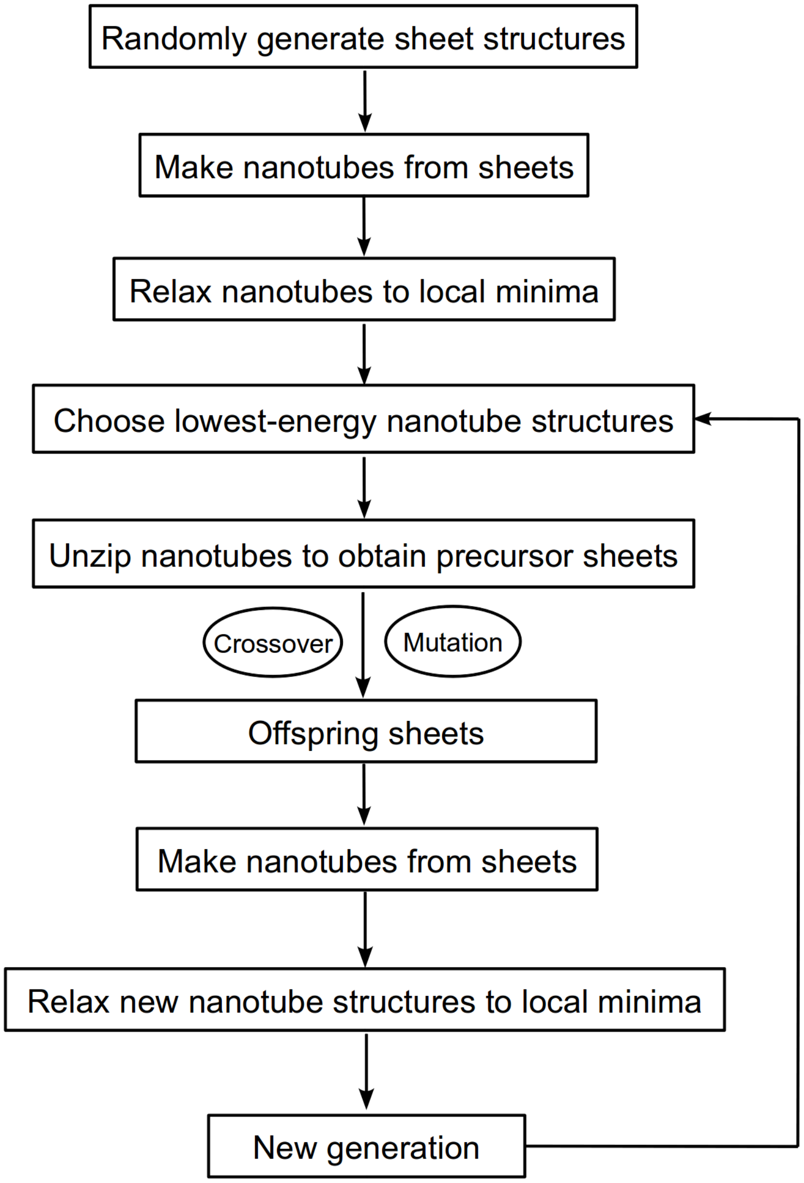

Figure A.2: Basic procedure of genetic algorithm for nanotubes.

into nanotubes to be used in the next generations. The whole process iterates until convergence. With curvature effects included, the energy surface becomes even more complicated and hence the convergence in nanotube calculations is slower than two-dimensional sheets, especially for small-diameter nanotubes.

Appendix B

Notes on pseudopotentials

We have managed to change the locality of pseudo atomic wavefunctions while fixing the atomic eigenenergies. Suppose we have generated a norm-conserving pseudopotential for carbon with a reference electronic configuration $2s^2 2p^2$ and cutoff radii r_s and r_p. Then pseudo atomic wavefunction φ_l is described by

$$\left[-\frac{\hbar^2}{2m}\nabla^2 + V_l^{ps}(r) + V_{xc}(r) + V_h(r)\right]\varphi_l(\mathbf{r}) = \epsilon_l \varphi_l(\mathbf{r}), \tag{B.1}$$

where V_l^{ps} is the pseudopotential for the angular momentum component l, V_{xc} is the exchange-correlation potential and V_h is the Hartree potential. We further separate the radial part of the wavefunction from φ_l by introducing

$$\varphi_l(\mathbf{r}) = \frac{U_l}{r} Y_{lm}, \tag{B.2}$$

where Y_{lm} is the spherical harmonic function. Then the radial equation is

$$\left[-\frac{\hbar^2}{2m}\frac{d^2}{dr^2} + V_l^{ps}(r) + V_{xc}(r) + V_h(r) + \frac{l(l+1)\hbar^2}{2mr^2}\right] U_l(r) = \epsilon_l U_l(r). \tag{B.3}$$

To change the locality of $U_l(r)$ while fixing ϵ_l, we alter $V_l^{ps}(r)$ inside the core region and keep the asymptotic behavior of $V_l^{ps}(r)$ ($\approx -4/r$ when $r \to \infty$). We have developed two methods to accomplish the task.

The first method is rather straightforward. We discretize the core region into N_s and

N_p points for s and p channels, respectively. Usually the same grids from pseudopotential generation are used. We denote the s and p pseudopotentials on these grids by two vectors ξ_s (with length N_s) and ξ_p (with length N_p). Then $U_s(r)$, $U_p(r)$ and ϵ_s, ϵ_p are functions of ξ_s and ξ_p, or ξ=(ξ_s, ξ_p), which is a vector with length N_s+N_p. The original question is then transformed into how to change ξ such that ϵ_s and ϵ_p are fixed, or how to move along the contour lines of ϵ_s and ϵ_p. The solution is simple. First, we compute the gradients of ϵ_s and ϵ_p with respect to ξ

$$\nabla_s = \frac{d\epsilon_s}{d\xi} = \left(\frac{\partial\epsilon_s}{\partial\xi_1}, \frac{\partial\epsilon_s}{\partial\xi_2}, \ldots\right), \tag{B.4}$$

and

$$\nabla_p = \frac{d\epsilon_p}{d\xi} = \left(\frac{\partial\epsilon_p}{\partial\xi_1}, \frac{\partial\epsilon_p}{\partial\xi_2}, \ldots\right). \tag{B.5}$$

∇_s and ∇_p are vectors with length N_s+N_p. Then we orthonormalize ∇_s and ∇_p via the Gram-Schmidt scheme

$$n_s = \frac{\nabla_s}{|\nabla_s|} \tag{B.6}$$

$$n_p' = \nabla_p - (\nabla_p \cdot n_s)n_s, \qquad n_p = \frac{n_p'}{|n_p'|}. \tag{B.7}$$

If we induce a small change in ξ that is perpendicular to both n_s and n_p, ϵ_s and ϵ_p will remain unchanged. For any arbitrary change to ξ, we simply perform the following transformation

$$\delta \to \delta' = \delta - (\delta \cdot n_s)n_s - (\delta \cdot n_p)n_p, \tag{B.8}$$

then δ' is perpendicular to n_s and n_p.

In practice, pseudopotentials are generated using the fhi98PP code [122]. We then employ the same discrete grids inside the core region as those used in pseudopotential generation, and calculate ∇_s and ∇_p with small changes of ξ at each grid point, which requires solving the radial equation (Equation B.3) N_s+N_p times. With ∇_s and ∇_p, we can obtain n_s and n_p via the Gram-Schmidt orthonormalization. Then we propose a small change to ξ, and make it perpendicular to n_s and n_p via the transformation in Equation (B.8). The resulting change is then applied to ξ, and new radial wavefunctions and eigenenergies are recalculated using fhi98PP. n_s and n_p are also recalculated. We repeat the process until we obtain desired changes in the pseudopotentials.

The above method is time-consuming because there are hundreds of discrete points inside the core region, and thus calculating n_s and n_p at each iteration requires hundreds of runs of fhi98PP to solve the radial equation. To improve the efficiency, instead of modifying ξ point by point, we can change the pseudopotential with continuous functions. we have considered changes in the form of sine and cosine functions. To confine the changes within the core region, we multiply each function by a cutoff function, which results in the following functions

$$e^{-(r/r_c)^8}, \quad \cos\left(\frac{k\pi}{r_c}r\right) e^{-(r/r_c)^8}, \quad \sin\left(\frac{k\pi}{r_c}r\right) e^{-(r/r_c)^8}, \tag{B.9}$$

where k is a positive integer and r_c is the cutoff radius.

We have used functions with k up to 2, resulting in 5 basis functions for each channel (s and p) and 10 basis functions in total. We denote these functions by f_i, i=1,2,. . .,10, and expand changes in the pseudopotentials with respect to them

$$\Delta = \sum_{i=1}^{10} c_i f_i \tag{B.10}$$

Following a similar procedure to that in the previous method, we calculate the gradients

$$\nabla_s = \left(\frac{\partial \epsilon_s}{\partial c_1}, \frac{\partial \epsilon_s}{\partial c_2}, \dots\right), \tag{B.11}$$

$$\nabla_p = \left(\frac{\partial \epsilon_p}{\partial c_1}, \frac{\partial \epsilon_p}{\partial c_2}, \dots\right), \tag{B.12}$$

and obtain the orthonormalized n_s and n_p

$$n_s = \frac{\nabla_s}{|\nabla_s|} \tag{B.13}$$

$$n'_p = \nabla_p - (\nabla_p \cdot n_s) n_s, \qquad n_p = \frac{n'_p}{|n'_p|}. \tag{B.14}$$

With a small arbitrary change to the pseudopotentials, δ, we expand it in terms of the

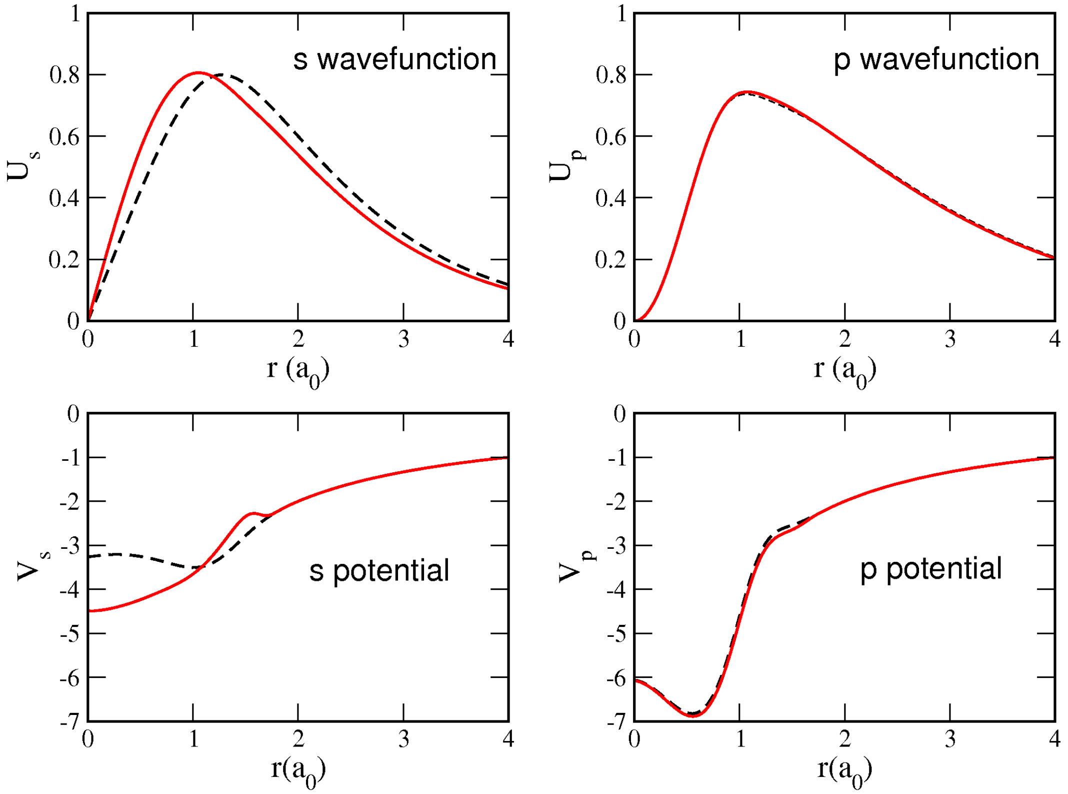

Figure B.1: Radial wavefunctions and pseudopotentials for s and p channels of a carbon atom. Black dashed lines show the wavefunctions and pseudopotentials from the original pseudopotential generation with the cutoff radii r_s=r_p=1.8a_0. Red solid lines show the wavefunctions and pseudopotentials for the case of a more localized s wavefunction, in which the eigen-energies ϵ_s and ϵ_p remain the same.

basis functions

$$\delta = \sum_{i=1}^{10} d_i f_i, \tag{B.15}$$

or simply δ=(d_1,...,d_{10}). Then we make the following transformation

$$\delta \to \delta' = \delta - (\delta \cdot n_s)n_s - (\delta \cdot n_p)n_p, \tag{B.16}$$

and modify the pseudopotentials according to δ'. This new method is much faster than the previous one, because evaluating n_s and n_p only needs to run fhi98PP 10 times at each iteration instead of hundreds.

By choosing different proposed changes in the pseudopotentials, we are able to generate new pseudopotentials with the atomic radial wavefunction of one channel (s or p) more localized or delocalized, while fixing approximately the other channel. For instance, if we propose changes only to the s pseudopotential, and make it more negative inside the core region, the s radial wavefunction will become more localized, while the p wavefunction stays approximately unchanged. As an example, Figure B.1 shows the radial wavefunctions and pseudopotentials of a carbon atom, for which the s wavefunction has been modified to be more localized compared to the original one. We can see that the wavefunction and pseudopotential of the p channel barely change.

Bibliography

[1] Richard M. Martin. *Electronic Structure: Basic Theory and Practical Methods.* Cambridge University Press (London), 2005.

[2] M. Fujimori, T. Nakata, T. Nakayama, E. Nishibori, K. Kimura, M. Takata, and M. Sakata. Peculiar covalent bonds in α-rhombohedral boron. *Phys. Rev. Lett.*, 82(22):4452–4455, 1999.

[3] N. Vast, S. Baroni, G. Zerah, J. M. Besson, A. Polian, M. Grimsditch, and J. C. Chervin. Lattice dynamics of icosahedral α-boron under pressure. *Phys. Rev. Lett.*, 78(4):693–696, 1997.

[4] Shunli Shang, Yi Wang, Raymundo Arroyave, and Zi-Kui Liu. Phase stability in α- and β-rhombohedral boron. *Phys. Rev. B*, 75(9):092101, 2007.

[5] Tadashi Ogitsu, Francois Gygi, John Reed, Yukitoshi Motome, Eric Schwegler, and Giulia Galli. Imperfect crystal and unusual semiconductor: Boron, a frustrated element. *J. Am. Chem. Soc.*, 131:1903, 2009.

[6] Hui Tang and Sohrab Ismail-Beigi. Novel precursors for boron nanotubes: The competition of two-center and three-center bonding in boron sheets. *Phys. Rev. Lett.*, 99(11):115501, 2007.

[7] Hui Tang and Sohrab Ismail-Beigi. Self-doping in boron sheets from first principles: A route to structural design of metal boride nanostructures. *Phys. Rev. B*, 80(13):134113, 2009.

[8] Hui Tang and Sohrab Ismail-Beigi. First-principles study of boron sheets and nanotubes. *Phys. Rev. B*, 82(11):115412, 2010.

[9] Ihsan Boustani. Systematic *ab initio* investigation of bare boron clusters: Determination of the geometry and electronic structures of B_n (n=2–14). *Phys. Rev. B*, 55(24):16426–16438, 1997.

[10] Alexander Quandt and Ihsan Boustani. Boron nanotubes. *ChemPhysChem.*, 6:2001, 2005.

[11] Russell N. Grimes. Boron clusters come of age. *J. Chem. Edu.*, 81:657, 2004.

[12] Xiaobao Yang, Yi Ding, and Jun Ni. *Ab initio* prediction of stable boron sheets and boron nanotubes: Structure, stability, and electronic properties. *Phys. Rev. B*, 77(4):041402, 2008.

[13] Abhishek K. Singh, Arta Sadrzadeh, and Boris I. Yakobson. Probing properties of boron α-tubes by *ab initio* calculations. *Nano Lett.*, 8:1314, 2008.

[14] Eswaramoorthi Iyyamperumal, Fang Fang, Agham-Bayan Posadas, Charles Ahn, Robert F. Klie, Yuan Zhao, Gary L. Haller, and Lisa D. Pfefferle. Synthesis of uniform diameter boron-based nanostructures using a mesoporous Mg-Al_2O_3 template and tests for superconductivity. *J. Phys. Chem. C*, 113:17661, 2009.

[15] M. S. Dresselhaus, G. Dresselhaus, and P. C. Eklund. *Science of fullerenes and carbon nanotubes.* Academic Press (San Diego), 1996.

[16] Ihsan Boustani. A comparative study of *ab initio* SCF-CI and DFT. Example of small boron clusters. *Chem. Phys. Lett.*, 233:273, 1995.

[17] Ihsan Boustani. Structure and stability of small boron clusters. A density functional theoretical study. *Chem. Phys. Lett.*, 240:135, 1995.

[18] Alessandra Ricca and Charles W. Bauschlicher. The structure and stability of B_n^+ clusters. *Chem. Phys.*, 208:233, 1996.

[19] Ihsan Boustani. New quasi-planar surfaces of bare boron. *Surf. Sci.*, 370:355, 1997.

[20] H. J. Zhai, L. S. Wang, A. N. Alexandrova, and A. I. Boldyrev. Electronic structure and chemical bonding of B_5^- and B_5 by photoelectron spectroscopy and *ab initio* calculations. *J. Chem. Phys.*, 117:7917, 2002.

[21] H. J. Zhai, B. Kiran, J. L. Li, and L. S. Wang. Hydrocarbon analogues of boron clusters – planarity, aromaticity and antiaromaticity. *Nat. Mater.*, 2:827, 2003.

[22] Hua-Jin Zhai, Anastassia N. Alexandrova, K. Alexander Birch, Alexander I. Boldyrev, and Lai-Sheng Wang. Hepta- and octacoordinate boron in molecular wheels of eight- and nine-atom boron clusters: Observation and confirmation. *Angew. Chem. Int. Ed.*, 42:6004, 2003.

[23] A. N. Alexandrova, A. I. Boldyrev, H. J. Zhai, and L. S. Wang. Electronic structure, isomerism, and chemical bonding in B_7^- and B_7. *J. Phys. Chem. A*, 108:3509, 2004.

[24] B. Kiran, S. Bulusu, H. J. Zhai, S. Yoo, X. C. Zeng, and L. S. Wang. Planar-to-tubular structural transition in boron clusters: B_{20} as the embryo of single-walled boron nanotubes. *Proc. Natl. Acad. Sci. U.S.A.*, 102:961, 2005.

[25] Jun-Ichi Aihara, Hideaki Kanno, and Toshimasa Ishida. Aromaticity of planar boron clusters confirmed. *J. Am. Chem. Soc.*, 127:13324, 2005.

[26] Ihsan Boustani, Alexander Quandt, and Angel Rubio. Boron quasicrystals and boron nanotubes: *Ab Initio* study of various B_{96} isomers. *J. Solid State Chem.*, 154:269, 2000.

[27] S. Chacko, D. G. Kanhere, and I. Boustani. *Ab initio* density functional investigation of B_{24} clusters: Rings, tubes, planes, and cages. *Phys. Rev. B*, 68(3):035414, 2003.

[28] Fu-Yang Tian and Yuan-Xu Wang. The competition of double-, four-, and three-ring tubular $B_{3n}(n{=}8\text{–}32)$ nanoclusters. *J. Chem. Phys.*, 129:024903, 2008.

[29] Ihsan Boustani, Angel Rubio, and Julio A. Alonso. *Ab initio* study of B_{32} clusters: Competition between spherical, quasiplanar and tubular isomers. *Chem. Phys. Lett.*, 311:21, 1999.

[30] Nevill Gonzalez-Szwacki, Arta Sadrzadeh, and Boris I. Yakobson. B_{80} fullerene: An *ab initio* prediction of geometry, stability, and electronic structure. *Phys. Rev. Lett.*, 98(16):166804, 2007.

[31] Ihsan Boustani and A. Quandt. Nanotubules of bare boron clusters: *Ab initio* and density functional study. *Europhys. Lett.*, 39:527, 1997.

[32] Asta Gindulyte, William N. Lipscomb, and Lou Massa. Proposed boron nanotubes. *Inorg. Chem.*, 37:6544, 1998.

[33] Ihsan Boustani, Alexander Quandt, Eduardo Hernandez, and Angel Rubio. New boron based nanostructured materials. *J. Chem. Phys.*, 110:3176, 1999.

[34] Ihsan Boustani and Alexander Quandt. Boron in *ab initio* calculations. *Comput. Mater. Sci.*, 11:132, 1998.

[35] Dragos Ciuparu, Robert F. Klie, Yimei Zhu, and Lisa Pfefferle. Systhesis of pure boron single-wall nanotubes. *J. Phys. Chem. B*, 108:3967, 2004.

[36] M. H. Evans, J. D. Joannopoulos, and S. T. Pantelides. Electronic and mechanical properties of planar and tubular boron structures. *Phys. Rev. B*, 72(4):045434, 2005.

[37] Jens Kunstmann and Alexander Quandt. Constricted boron nanotubes. *Chem. Phys. Lett.*, 402:21, 2005.

[38] Jens Kunstmann and Alexander Quandt. Broad boron sheets and boron nanotubes: An *ab initio* study of structural, electronic, and mechanical properties. *Phys. Rev. B*, 74(3):035413, 2006.

[39] K. C. Lau and R. Pandey. Stability and electronic properties of atomistically-engineered 2D boron sheets. *J. Phys. Chem. C*, 111:2906, 2007.

[40] I. Cabria, M. J. Lopez, and J. A. Alonso. Density functional calculations of hydrogen adsorption on boron nanotubes and boron sheets. *Nanotechnology*, 17:778, 2006.

[41] Ali Sebetci, Ersen Mete, and Ihsan Boustani. Free standing double walled boron nanotubes. *J. Phys. Chem. Solids*, 69:2004, 2008.

[42] Qing-Bo Yan, Xian-Lei Sheng, Qing-Rong Zheng, Li-Zhi Zhang, and Gang Su. Family of boron fullerenes: General constructing schemes, electron counting rule, and *ab initio* calculations. *Phys. Rev. B*, 78(20):201401, 2008.

[43] Rajendra R. Zope. The α-boron cages with four-member rings. *EPL*, 85:68005, 2009.

[44] Rajendra R. Zope, Tunna Baruah, K. C. Lau, Amy Y. Liu, M. R. Pederson, and B. I. Dunlap. Boron fullerenes: From B_{80} to hole doped boron sheets. *Phys. Rev. B*, 79(16):161403, 2009.

[45] L. A. Chernozatonskii. Diboride bifullerenes and binanotubes. *JETP Lett.*, 74:335, 2001.

[46] Alexander Quandt, Amy Y. Liu, and Ihsan Boustani. Density-functional calculations for prototype metal-boron nanotubes. *Phys. Rev. B*, 64:125422, 2001.

[47] Peihong Zhang and Vincent H. Crespi. Theory of B_2O and BeB_2 nanotubes: New semiconductors and metals in one dimension. *Phys. Rev. Lett.*, 89:056403, 2002.

[48] M. Kociak, A. Yu. Kasumov, S. Guéron, B. Reulet, I. I. Khodos, Yu. B. Gorbatov, V. T. Volkov, L. Vaccarini, and H. Bouchiat. Superconductivity in ropes of single-walled carbon nanotubes. *Phys. Rev. Lett.*, 86(11):2416–2419, 2001.

[49] I. Takesue, J. Haruyama, N. Kobayashi, S. Chiashi, S. Maruyama, T. Sugai, and H. Shinohara. Superconductivity in entirely end-bonded multiwalled carbon nanotubes. *Phys. Rev. Lett.*, 96(5):057001, 2006.

[50] Jun Nagamatsu, Norimasa Nakagawa, Takahiro Muranaka, Yuji Zenitani, and Jun Akimitsu. Superconductivity at 39 K in magnesium diboride. *Nature*, 410:63, 2001.

[51] S. Saito, S. G. Louie, and M. L. Cohen. Electronic structure and energetics of MgB_2 nanotube. *J. Phys. Soc. Jpn.*, 76:043707, 2007.

[52] Vladimir Pokropivny. Nanostructured superconductors: from granular through wire towards high-T_c nanotubular 2D composites. *Int. J. of Nanotechnology*, 1:170, 2004.

[53] V. V. Ivanovskaya, A. N. Enjashin, A. A. Sofronov, Yu. N. Makurin, N. I. Medvedeva, and A. L. Ivanovskii. Quantum chemical simulation of the electronic structure and chemical bonding in (6,6), (11,11) and (20,0)-like metal-boron nanotubes. *J. Mol. Struct: THEOCHEM*, 625:9, 2003.

[54] Dasari L. V. K. Prasad and Eluvathingal D. Jemmis. Boron and MgB_2 analogs of fullerenes and carbon nanotubes: A density functional theory study. *J. Mol. Struct: THEOCHEM*, 771:111, 2006.

[55] P. Hohenberg and W. Kohn. Inhomogeneous electron gas. *Phys. Rev.*, 136(3B):B864–B871, 1964.

[56] W. Kohn and L. J. Sham. Self-consistent equations including exchange and correlation effects. *Phys. Rev.*, 140(4A):A1133–A1138, 1965.

[57] M. C. Payne, M. P. Teter, D. C. Allan, T. A. Arias, and J. D. Joannopoulos. Iterative minimization techniques for ab initio total-energy calculations: molecular dynamics and conjugate gradients. *Rev. Mod. Phys.*, 64(4):1045–1097, 1992.

[58] D. M. Ceperley and B. J. Alder. Ground state of the electron gas by a stochastic method. *Phys. Rev. Lett.*, 45(7):566–569, 1980.

[59] John P. Perdew, J. A. Chevary, S. H. Vosko, Koblar A. Jackson, Mark R. Pederson, D. J. Singh, and Carlos Fiolhais. Atoms, molecules, solids, and surfaces: Applications of the generalized gradient approximation for exchange and correlation. *Phys. Rev. B*, 46(11):6671–6687, 1992.

[60] John P. Perdew, Kieron Burke, and Matthias Ernzerhof. Generalized gradient approximation made simple. *Phys. Rev. Lett.*, 77(18):3865–3868, 1996.

[61] D. R. Hamann, M. Schlüter, and C. Chiang. Norm-conserving pseudopotentials. *Phys. Rev. Lett.*, 43(20):1494–1497, 1979.

[62] D. R. Hamann. Generalized norm-conserving pseudopotentials. *Phys. Rev. B*, 40(5):2980–2987, 1989.

[63] N. Troullier and José Luriaas Martins. Efficient pseudopotentials for plane-wave calculations. *Phys. Rev. B*, 43(3):1993–2006, 1991.

[64] N. Marzari, I. Souza, and D. Vanderbilt. An introduction to maximally-localized Wannier functions. *Highlight the Month, Psi-K Newsletter*, 57:129–68, 2003.

[65] Nicola Marzari and David Vanderbilt. Maximally localized generalized Wannier functions for composite energy bands. *Phys. Rev. B*, 56(20):12847–12865, 1997.

[66] Ivo Souza, Nicola Marzari, and David Vanderbilt. Maximally localized Wannier functions for entangled energy bands. *Phys. Rev. B*, 65(3):035109, 2001.

[67] Arash A. Mostofi, Jonathan R. Yates, Young-Su Lee, Ivo Souza, David Vanderbilt, and Nicola Marzari. Wannier90: A tool for obtaining maximally-localised Wannier functions. *Comput. Phys. Commun.*, 178:685–699, 2007.

[68] C. Brouder, G. Panati, M. Calandra, C. Mourougane, and N. Marzari. Exponential localization of Wannier functions in insulators. *Phys. Rev. Lett.*, 98(4):46402, 2007.

[69] R. Resta. Macroscopic polarization in crystalline dielectrics: the geometric phase approach. *Reviews of Modern Physics*, 66(3):899–915, 1994.

[70] Jonathan R. Yates, Xinjie Wang, David Vanderbilt, and Ivo Souza. Spectral and Fermi surface properties from Wannier interpolation. *Phys. Rev. B*, 75(19):195121, 2007.

[71] Per-Olov Löwdin. On the non-orthogonality problem connected with the use of atomic wave functions in the theory of molecules and crystals. *J. Chem. Phys.*, 18(3):365–375, 1950.

[72] Daniel Sanchez-Portal, Emilio Artacho, and Jose M. Soler. Projection of plane-wave calculations into atomic orbitals. *Solid State Communications*, 95:685–690, 1995.

[73] P. J. M. Laarhoven, P. J. M. van Laarhoven, and E. H. L. Aarts. *Simulated annealing: theory and applications*. Springer, 1987.

[74] S. Goedecker. Minima hopping: An efficient search method for the global minimum of the potential energy surface of complex molecular systems. *J. Chem. Phys.*, 120:9911, 2004.

[75] S. Goedecker, W. Hellmann, and T. Lenosky. Global minimum determination of the Born-Oppenheimer surface within density functional theory. *Phys. Rev. Lett.*, 95(5):55501, 2005.

[76] C. J. Pickard and R. J. Needs. High-pressure phases of silane. *Phys. Rev. Lett.*, 97(4):45504, 2006.

[77] Artem R. Oganova and Colin W. Glass. Crystal structure prediction using *ab initio* evolutionary techniques: Principles and applications. *J. Chem. Phys.*, 124:244704, 2006.

[78] Artem R. Oganov and Colin W. Glass. Evolutionary crystal structure prediction as a tool in materials design. *J. Phys. : Condens. Matter*, 20:064210, 2008.

[79] Colin W. Glassa, Artem R. Oganova, and Nikolaus Hansenc. USPEX–Evolutionary crystal structure prediction. *Comput. Phys. Commun.*, 175:713–720, 2006.

[80] Atomistix ToolKit Manual. http://www.quantumwise.com/documents/manuals/ATK-2008.10/index.html.

[81] Graeme Henkelman, Blas P. Uberuaga, and Hannes Jónsson. A climbing image nudged elastic band method for finding saddle points and minimum energy paths. *J. Chem. Phys.*, 113:9901, 2000.

[82] G. Henkelman and H. Jónsson. Improved tangent estimate in the nudged elastic band method for finding minimum energy paths and saddle points. *J. Chem. Phys.*, 113:9978, 2000.

[83] G. Henkelman, G. Jóhannesson, and H. Jónsson. Methods for finding saddle points and minimum energy paths. *Progress in Theoretical Chemistry and Physics*, 5:269–302, 2002.

[84] H. Jónsson, G. Mills, and K.W. Jacobsen. Nudged elastic band method for finding minimum en-ergy paths of transitions. *Classical and Quantum Dynamics in Condensed Phase Simulations*, pages 385–404, 1998.

[85] P. J. Durrant and B. Durrant. *Introduction to advanced inorganic chemistry.* John Wiley & Sons, Inc. (New York), 1962.

[86] D. Porezag, Th. Frauenheim, Th. Köhler, G. Seifert, and R. Kaschner. Construction of tight-binding-like potentials on the basis of density-functional theory: Application to carbon. *Phys. Rev. B*, 51(19):12947–12957, 1995.

[87] R. Saito, G. Dresselhaus, and M. S. Dresselhaus. *Physical Properties of Carbon Nanotubes*. Imperial College Press (London), 1998.

[88] Noriaki Hamada, Shinichi I. Sawada, and Atsushi Oshiyama. New one-dimensional conductors: Graphitic microtubules. *Phys. Rev. Lett.*, 68(10):1579–1581, 1992.

[89] D. H. Robertson, D. W. Brenner, and J. W. Mintmire. Energetics of nanoscale graphitic tubules. *Phys. Rev. B*, 45(21):12592–12595, 1992.

[90] O. Gülseren, T. Yildirim, and S. Ciraci. Systematic *ab initio* study of curvature effects in carbon nanotubes. *Phys. Rev. B*, 65(15):153405, 2002.

[91] N. Gonzalez-Szwacki and C.J. Tymczak. The symmetry of the boron buckyball and a related boron nanotube. *Chem. Phys. Lett.*, 494:80–83, 2010.

[92] Chr. Møller and M. S. Plesset. Note on an approximation treatment for many-electron systems. *Phys. Rev.*, 46(7):618–622, 1934.

[93] T. Dauxois and M. Peyrard. *Physics of solitons*. Cambridge Univ Pr, 2006.

[94] Susumu Okada and Atsushi Oshiyama. Curvature-induced metallization of double-walled semiconducting zigzag carbon nanotubes. *Phys. Rev. Lett.*, 91(21):216801, 2003.

[95] Iann C. Gerber and Janos G. Angyan. Potential curves for alkaline-earth dimers by density functional theory with long-range correlation corrections. *Chem. Phys. Lett.*, 416:370–375, 2005.

[96] Aleksey N. Kolmogorov and Stefano Curtarolo. Prediction of different crystal structure phases in metal borides: A lithium monoboride analog to MgB_2. *Phys. Rev. B*, 73(18):180501, 2006.

[97] M. Widom and M. Mihalkovič. Relative stability of α and β boron. In *Journal of Physics: Conference Series*, volume 176, page 012024. IOP Publishing, 2009.

[98] M. I. Eremets, V. V. Struzhkin, H. Mao, and R. J. Hemley. Superconductivity in boron. *Science*, 293(5528):272, 2001.

[99] Artem R. Oganov, Jiuhua Chen, Carlo Gatti, Yanzhang Ma, Colin W. Glass, Zhenxian Liu, Tony Yu, Oleksandr O. Kurakevych, and Vladimir L. Solozhenko. Ionic high-pressure form of elemental boron. *Nature*, 457:863, 2009.

[100] E. Yu. Zarechnaya, L. Dubrovinsky, N. Dubrovinskaia, Y. Filinchuk, D. Chernyshov, V. Dmitriev, N. Miyajima, A. El Goresy, H. F. Braun, S. Van Smaalen, I. Kantor, A. Kantor, V. Prakapenka, M. Hanfland, A. S. Mikhaylushkin, I. A. Abrikosov, and S. I. Simak. Superhard semiconducting optically transparent high pressure phase of boron. *Phys. Rev. Lett.*, 102(18):185501, 2009.

[101] U. Häussermann, SI Simak, R. Ahuja, and B. Johansson. Metal-nonmetal transition in the boron group elements. *Phys. Rev. Lett.*, 90(6):65701, 2003.

[102] S. K. Bose, T. Kato, and O. Jepsen. Superconductivity in boron under pressure: A full-potential linear muffin-tin orbitals study. *Physical Review B*, 72(18):184509, 2005.

[103] PWSCF (plane-wave self-consistent field) is a computer code for electronic-structure calculations using pseudopotentials. http://www.pwscf.org/.

[104] Paolo Giannozzi, Stefano Baroni, Nicola Bonini, Matteo Calandra, Roberto Car, Carlo Cavazzoni, Davide Ceresoli, Guido L Chiarotti, Matteo Cococcioni, Ismaila Dabo, Andrea Dal Corso, Stefano de Gironcoli, Stefano Fabris, Guido Fratesi, Ralph Gebauer, Uwe Gerstmann, Christos Gougoussis, Anton Kokalj, Michele Lazzeri, Layla Martin-Samos, Nicola Marzari, Francesco Mauri, Riccardo Mazzarello, Stefano Paolini, Alfredo Pasquarello, Lorenzo Paulatto, Carlo Sbraccia, Sandro Scandolo, Gabriele Sclauzero, Ari P Seitsonen, Alexander Smogunov, Paolo Umari, and Renata M Wentzcovitch. QUANTUM ESPRESSO: A modular and open-source software project for quantum simulations of materials. *J. Phys.: Condens. Matter*, 21(39):395502, 2009.

[105] L. Schlapbach and A. Züttel. Hydrogen-storage materials for mobile applications. *Nature*, 414(6861):353–358, 2001.

[106] G. W. Crabtree, M. S. Dresselhaus, and M. V. Buchanan. The hydrogen economy. *Physics Today*, 57(12):39–44, 2004.

[107] A. C. Dillon, K. M. Jones, T. A. Bekkedahl, C. H. Kiang, D. S. Bethune, and M. J. Heben. Storage of hydrogen in single-walled carbon nanotubes. *Nature*, 386:377–379, 1997.

[108] Y. H. Kim, Y. Zhao, A. Williamson, M. J. Heben, and S. B. Zhang. Nondissociative Adsorption of H_2 Molecules in Light-Element-Doped Fullerenes. *Phys. Rev. Lett.*, 96(1):16102, 2006.

[109] T. Yildirim and S. Ciraci. Titanium-decorated carbon nanotubes as a potential high-capacity hydrogen storage medium. *Phys. Rev. Lett.*, 94(17):175501, 2005.

[110] Y. Zhao, Y.H. Kim, AC Dillon, MJ Heben, and SB Zhang. Hydrogen storage in novel organometallic buckyballs. *Phys. Rev. Lett.*, 94(15):155504, 2005.

[111] H. Lee, W. I. Choi, and J. Ihm. Combinatorial search for optimal hydrogen-storage nanomaterials based on polymers. *Phys. Rev. Lett.*, 97(5):056104, 2006.

[112] J. Li, T. Furuta, H. Goto, T. Ohashi, Y. Fujiwara, and S. Yip. Theoretical evaluation of hydrogen storage capacity in pure carbon nanostructures. *J. Chem. Phys.*, 119:2376, 2003.

[113] S. K. Bhatia and A. L. Myers. Optimum conditions for adsorptive storage. *Langmuir*, 22(4):1688–1700, 2006.

[114] M. Yoon, S. Yang, C. Hicke, E. Wang, D. Geohegan, and Z. Zhang. Calcium as the superior coating metal in functionalization of carbon fullerenes for high-capacity hydrogen storage. *Phys. Rev. Lett.*, 100(20):206806, 2008.

[115] Yufeng Zhao, Mark T. Lusk, Anne C. Dilon, Michael J. Heben, and Shengbai Zhang. Boron-based organometallic nanostructures: Hydrogen storage properties and structure stability. *Nano Lett.*, 8:157, 2008.

[116] Sheng Meng, Efthimios Kaxiras, and Zhenyu Zhang. Metal-diboride nanotubes as high-capacity hydrogen storage media. *Nano Lett.*, 7:663, 2007.

[117] Yuanchang Li, Gang Zhou, Jia Li, Bin-Ling Gu, and Wenhui Duan. Alkali-metal-doped B_{80} as high-capacity hydrogen storage media. *J. Phys. Chem. C*, 112:19268, 2008.

[118] Ming Li, Yafei Li, Zhen Zhou, Panwen Shen, and Zhongfang Chen. Ca-coated boron fullerenes and nanotubes as superior hydrogen storage materials. *Nano. Lett.*, 9(5):1944, 2009.

[119] S. Er, G. A. de Wijs, and G. Brocks. DFT Study of Planar Boron Sheets: A New Template for Hydrogen Storage. *J. Phys. Chem. C*, 113(43):18962–18967, 2009.

[120] D. W. Boukhvalov, M. I. Katsnelson, and A. I. Lichtenstein. Hydrogen on graphene: Electronic structure, total energy, structural distortions and magnetism from first-principles calculations. *Phys. Rev. B*, 77(3):35427, 2008.

[121] G. Chen, X. G. Gong, and C. T. Chan. Theoretical study of the adsorption of H_2 on (3, 3) carbon nanotubes. *Phys. Rev. B*, 72(4):45444, 2005.

[122] M. Fuchs and M. Scheffler. Ab initio pseudopotentials for electronic structure calculations of poly-atomic systems using density-functional theory. *Computer Physics Communications*, 119(1):67–98, 1999.